2016

Reservoir Characterization and Flow Simulation for CO 2-EOR in the Tensleep Formation Using Discrete Fracture Networks, Teapot Dome, Wyoming

Payam Kavousi Ghahfarokhi

Reservoir Characterization and Flow Simulation for CO_2-EOR in the Tensleep Formation Using Discrete Fracture Networks, Teapot Dome, Wyoming

Payam Kavousi Ghahfarokhi

Dissertation submitted to the
Eberly College of Arts and Sciences
at West Virginia University

In partial fulfillment of the requirement
for the degree of

Doctor of Philosophy
in
Geology

Thomas Wilson, Ph.D., Chair
Timothy Carr, Ph.D.
Jaime Toro, Ph.D.
Shahab Mohaghegh, Ph.D.
Alan Brown, Ph.D.

Department of Geology and Geography

Morgantown, West Virginia
2016

Keywords: Naturally fractured reservoir, Tensleep, CO_2-EOR, Flow simulation

ABSTRACT

Reservoir Characterization and Flow Simulation for CO_2-EOR in the Tensleep Formation Using Discrete Fracture Networks, Teapot Dome, Wyoming

Payam Kavousi Ghahfarokhi

The Tensleep oil reservoir at Teapot Dome, Wyoming, USA, is a naturally fractured tight sandstone reservoir that has been considered for carbon-dioxide enhanced oil recovery (CO_2-EOR) and sequestration. CO_2-EOR analysis requires a thorough understanding of the Tensleep fracture network. Wireline image logs from the field suggest that the reservoir fracture network is dominated by early formed structural hinge oblique fractures with interconnectivity enhanced by hinge parallel and hinge perpendicular fracture sets. Available post stack 3D seismic data are used to generate a seismic fracture intensity attribute for the reservoir fracture network. The resulting seismic fracture intensity is qualitatively correlated to the field production history. Wells located on hinge-oblique discontinuities are more productive than other wells in the field. We use Oda's method to upscale the fracture permeabilities in the discrete fracture network for use in a dual porosity fluid flow simulator. We analytically show that Oda's method is sensitive to the grid orientation relative to fracture set strike. Results show that the calculated permeability tensors have maximum geometric mean for the non-zero permeability components ($k_{xx}, k_{yy}, k_{zz}, k_{xy}$) when the dominant fracture set cuts diagonally through the grid cell at 45° relative to the grid cell principal directions (i, j). The geometric mean of the permeability tensor components falls to a minimum when the dominant fracture set is parallel to either grid wall (i or j principal directions). The latter case has off-diagonal permeability terms close to zero. We oriented the Tensleep reservoir grid to N72°W to minimize the off-diagonal permeability terms. The seismic fracture intensity attribute is then used to generate a realization of the reservoir fracture network. Subsequently, fracture properties are upscaled to the reservoir grid scale for a fully compositional flow simulation. We implemented a PVT analysis using CO_2 swelling test results to build an 8 component equation of the state. A fully compositional flow simulation is conducted to acquire a history match between model production and production history. The history matching process reveals that high fracture permeabilities enhance water conning around the producers and decreases the oil production. Moreover, increasing apertures in the model DFN will result in higher oil production from the field. Thus, aperture and vertical permeabilities are adjusted for the model DFN to approximate the production history. We analyzed two CO_2-EOR cases with different injection patterns. One has the injectors parallel to the main fracture set and the second one has injectors perpendicular to the main fracture set. Results show that the former model has higher oil recovery with later CO_2 breakthrough than the second model. The dominant fracture set (N76°W) affects the CO_2-EOR sweep efficiency in the Tensleep reservoir. We show that CO_2 breakthrough is inevitable in both cases. The fault transmissibility multipliers are also assumed; they are uncertain parameters that could influence CO_2-EOR. The model with completely impermeable faults yields a lower CO_2-EOR sweep efficiency compared to the case for which all faults are fully permeable.

To my parents

Acknowledgments

I would like to gratefully thank my advisor Dr. Thomas Wilson for his knowledge, guidance, support, and his friendship during my graduate study at West Virginia University.

My thank also goes to my committee members, Dr. Timothy Carr, Dr. Jaime Toro, Dr. Shahab Mohaghegh, Dr. Allan Brown, for their constructive comments and suggestions.

I am also thankful to Dr. Ryan Shackleton for his comments and suggestions.

I am also thankful to Mr. Randy Crow, The IT manager at the geology and geography department at West Virginia University for his help with software supports.

Contents

List of Figures

Chapter 1: INTRODUCTION

Overview

The Penssilvanian Tensleep reservoir at Teapot Dome oilfield is an unconventional, naturally fractured tight sandstone reservoir (NFR). Interpretation of open fractures identified in wireline image logs from the field suggests that the reservoir fracture network is dominated by early formed structural hinge-oblique fractures (N76°W) with interconnectivity enhanced by hinge-parallel and hinge perpendicular fracture sets. The Tensleep reservoir at Teapot Dome has been considered for carbon dioxide enhanced oil recovery (CO_2-EOR). The core of this research is to use wireline image logs and post-stack 3D seismic data to generate a discrete fracture network for the Tensleep reservoir and use the model DFN in a fully compositional flow simulator for CO_2-EOR modeling. The production history data are available through Rocky Mountain Oil Testing Center (RMOTC), but no bottom hole pressure and perforation intervals are available.

Developing a model discrete fracture network (DFN) is intended to address anisotropy through stochastic modeling of the fracture distribution in the reservoir obtained from wireline image logs data and seismic fracture intensity attributes. The distribution of fracture parameters such as spacing, length, aperture, and etc., are generated from data ranging from small scale wireline image logs to large scale outcrops and 3D seismic data.

Fluid flow can be modeled through the discrete fracture network by using unstructured control volume finite difference approach with two-point flux approximation (Karimi-Fard et al. 2004; Karimi-Fard et al. 2006; Gong et al. 2008). Although this approach provides a more accurate

estimate of the permeability tensors, they are computationally expensive and unpractical for use in large fields (Li et al. 2015; Karimi-Fard et al. 2006).

The simpler and more applicable approach for large scale reservoirs is a combination of Warren and Root (dual porosity) model and the discrete fracture network (DFN) (Dershowitz, 2000). The Warren and Root approach (1963) is mathematically less complex and faster than a DFN simulation. Thus, the DFN will only be used to generate reservoir fracture network; fluid flow simulation will be handled using the Warren and Root approach. This integrated methodology is undertaken to model CO_2-EOR in the Tensleep reservoir at Teapot Dome, Wyoming.

In this research, we used the wireline image logs and post-stack 3D seismic data to generate a fracture intensity attribute to model a realization of the reservoir fracture network. We enhance the seismic resolution through seismic spectral bluing (SSB) (Lancaster and Whitcombe, 2000). The dissimilarity of the maximum negative curvature of the SSB seismic cube provides us a relative fracture intensity attribute for subsequent model DFN generation.

The properties of model DFN are upscaled into a reservoir grid. Oda's (1985) method is used to calculate permeability tensors for use in a dual porosity reservoir model. The calculated permeability tensors are used for the fracture medium along with matrix medium parameters and tensors in a fully compositional flow simulator. DFN assisted reservoir simulation has not been implemented for the Tensleep reservoir in previous works (Friedmann and Stamp, 2006; Chiaramonte, 2009; Gaviria, 2006). This research shows that integrated DFN-dual porosity approach could address the reservoir complexities for CO_2-EOR. The generated DFN is adjusted against the production history in a history matching process and then used for CO_2-EOR analysis.

CO_2-EOR analysis shows that the dominant fracture set (N76°W) exerts significant control on sweep efficiency.

Dissertation Outlines

This dissertation includes 3 main chapters. In the second chapter, we develop a model DFN. The model is based on interpreted the wireline image logs, outcrops, and seismic data. A seismic-assisted workflow is used to model the fracture intensity attribute in the Tensleep reservoir. The workflow is based on curvature dissimilarity of the signals in the post-stack 3D seismic data which can be related to fracture zones because of the associated flexure or velocity sags often associated with fracture zones. The fracture intensity attribute is then correlated qualitatively to the production history data. The analysis shows that wells on the northwest trending discontinuities have higher production. The fracture intensity attribute generated in this chapter will be used for history matching analysis (Chapter 4).

In Chapter 3, we evaluate the Oda (1985) method. The Oda approach is computer coded and is used to understand limitation along with the influence of grid orientation. We analytically show that Oda's method is highly dependent on grid orientation, especially when fracture intensities are not similar for different sets. We show that eigenvalues and eigenvectors of the permeability tensor depend on grid orientation. This dependency could considerably affect the results of flow simulation. The production profiles vary systematically with the grid orientation. The flow simulations for several grid orientations unravel the dependency of the permeability tensor on grid orientation. The results of this chapter will enhance the understandings of Oda's method and its effects on flow simulation results. One conclusion of this chapter that we used for flow simulation is that off-diagonal permeability terms are close to zero when the grid is parallel to the main fracture set. This grid orientation considerably improves simulation speed.

The final chapter focuses on history matching and CO_2-EOR analysis for the Tensleep reservoir at Teapot Dome. The perquisite for CO_2-EOR is a history matched reservoir model. The latter is necessary since the CO_2-EOR should be initialized by pressure and water saturation for each grid block at the end of field production history. We use Oda's method to upscale fracture permeabilities into a dual porosity compositional flow simulator. Then, a sensitivity analysis is conducted on fracture aperture distribution to highlight its influence on fluid flow simulation. Moreover, we present a methodology to incorporate seismic-extracted permeability barriers (interpreted deformation bands) in the flow simulation. The deformation bands will be considered as imaginary faults with no displacement or slip and with transmissibility multipliers equal to zero. The results will reveal the potential deformation bands impact on hindering fluid flow in the Tensleep reservoir in addition to reservoir partitioning. Additional sensitivity analysis is implemented for fracture vertical permeability in the Tensleep reservoir. We show that high values of K_z results in water conning around the producers. The K_z permeabilities along with fracture aperture distribution are changed to obtain a history match. The final history matched model is used for two CO_2-EOR cases. The first model has CO_2 injectors parallel to the dominant fracture set (N76°W), and the second model has injectors perpendicular to the dominant fracture set.

Chapter 2: Fracture intensity attribute for the Tensleep reservoir at Teapot Dome, Wyoming, USA[1]

Abstract

The Tensleep oil reservoir at Teapot Dome, Wyoming, USA, is a naturally fractured tight sandstone reservoir that has been considered for carbon dioxide enhanced oil recovery (CO_2-EOR) and sequestration. Interpretation of open fractures identified in wireline image logs from the field suggests that the reservoir fracture network is dominated by early formed structural hinge-oblique fractures with interconnectivity enhanced by hinge-parallel and hinge-perpendicular fracture sets. Previous studies show that 3D seismic scale discontinuity attributes are dominated by more recent hinge-parallel and strike slip trends. The most negative curvature attribute that we used highlights concave features attributed to subtle traveltime delay through fracture zones and small faults or flexures associated with the fracture swarms. The poststack discontinuity extraction workflow incorporated seismic spectral blueing (SSB) to enhance the resolution of the seismic data. The SSB process is followed by computation of the short-wavelength most negative curvature. Subsequently, the minimum similarity attribute is applied to accentuate regions with minimum similarity of curvature. An edge-illumination process is then applied to the minimum similarity of the most negative curvature output. Discontinuities extracted through edge illumination locate regions of minimal similarity in curvature along fracture zones or small fault boundaries. This workflow enhances hinge-oblique discontinuities without azimuthal filtering and provides a fracture intensity attribute, which is used as an input to distribute the fracture intensity through the

[1] *Kavousi, P., Wilson, T., 2015, Fracture intensity attribute for the Tensleep reservoir at Teapot Dome, Wyoming, USA: Interpretation, **3**(3), SZ41-SZ48.*

model discrete fracture network. Qualitative correlation of production data to extracted discontinuities suggests that wells located on hinge-oblique discontinuities are more productive than other wells in the field.

Introduction

Teapot Dome Field is part of the Naval Petroleum Reserve, known as *NPR-3*. Teapot Dome was owned and operated by the U.S. Department of Energy and Rocky Mountain Oilfield Testing Center (RMOTC) from 1977 through 2014. In 2014, the field was placed on the market and sold in early 2015 to Stranded Oil Resources Corporation. Field data including 3D seismic, geophysical logs, and production history were publicly accessible through RMOTC. A pilot carbon dioxide enhanced oil recovery (CO_2-EOR) test was planned for the Tensleep Formation that would have used existing Tensleep wells. The proposed pilot test would inject a minimum of 60 tons/day CO_2 for at least 1.5 months (Chiaramonte et al., 2011) to recover residual oil in the Tensleep reservoir by CO_2 sequestration.

The Pennsylvanian Tensleep reservoir in the Teapot Dome oilfield is an unconventional, naturally fractured tight sandstone reservoir (NFR). The Tensleep reservoir is classified as an NFR type II reservoir, for which the rock matrix provides the main hydrocarbon storage capacity and the reservoir fracture network provides the fluid flow pathways (Allan, 2003). Oil production from the Tensleep Formation is restricted to the structural culmination in the southern part of the field. The Tensleep Formation in the southern part of Teapot Dome has been estimated to contain 3.8 million bbl (0.6 million m^3) oil of 32° American Petroleum Institute (API) and 11 MMscf (0.31 million m^3) of natural gas to date. More than 1.8 million bbl (0.29 million m^3) oil and 170 million bbl. (27 million m^3) of water have already been produced (Friedman and Stamp, 2006). Chiaramonte (2008) observes residual oil saturations between 29% and 56% in Tensleep cores from Teapot

Dome. Recovery of the residual oil requires a thorough understanding of the reservoir fracture network, as well as rock physics and fluid properties. In this study, we focus on an approach for poststack extraction of seismic scale discontinuities in the Tensleep reservoir that may exert significant control on reservoir productivity. The intensity of natural fractures within the reservoir discrete fracture network (DFN) is modeled through a combination of ant tracking, coherence, and curvature into a composite fracture intensity attribute. In this study, we refer to ant tracking (Pederson et al., 2002, 2003) as an edge-illumination process. Smith (2008) uses this edge-illumination process to distribute the fracture intensity in her Tensleep fracture model. Wilson et al. (2015) distribute the fracture intensity throughout the reservoir model, using a composite attribute developed from a weighted combination of edge illumination and directional curvature. Curvature was computed normal to the dominant northwest hinge-oblique reservoir fracture set. In this study, we use seismic spectral blueing (SSB) to enhance seismic resolution (Lancaster and Whitcombe, 2000) for subsequent attribute analysis. The most negative curvature is then calculated from the SSB cube. The distribution of the minimum similarity attribute is then calculated throughout the negative curvature volume. Thereafter, the edge-illumination process is computed through the minimum similarity of the most negative curvature cube and is used as the fracture intensity attribute to distribute variations in fracture intensity through the model DFN. The basic attribute in this workflow (following SSB) is the most negative curvature, which is used to delineate subtle flexures interpreted to be associated with the fracture swarms or velocity sags associated with intensely fractured zones.

Open fractures identified in the reservoir from wireline image logs may reduce the interval velocity especially when concentrated in seismically detectable zones with widths approximately equal to the Fresnel zone diameter and larger. The workflow described in this study is designed to detect

subtle velocity sags or flexures in the 3D seismic that might be associated with intensely fractured zones. We show that edges extracted from the similarity attribute (Tingdahl and de Rooj, 2005) using the illumination process reveal the presence of velocity variation or flexures when applied to short- wavelength negative curvature calculated from the SSB seismic volume. We show that the resultant intensity attribute can be qualitatively correlated to the production history in the producing culmination. Results suggest that wells on modeled hinge-oblique discontinuities were more productive than other wells in the culmination.

Geologic setting and lithology

Teapot Dome is an elongated, doubly plunging, asymmetric basement-cored anticline with a north– northwest trending axis (Cooper, 2000; Cooper et al., 2006). It is located near the southwestern edge of the Powder River Basin (Figure 2-1).

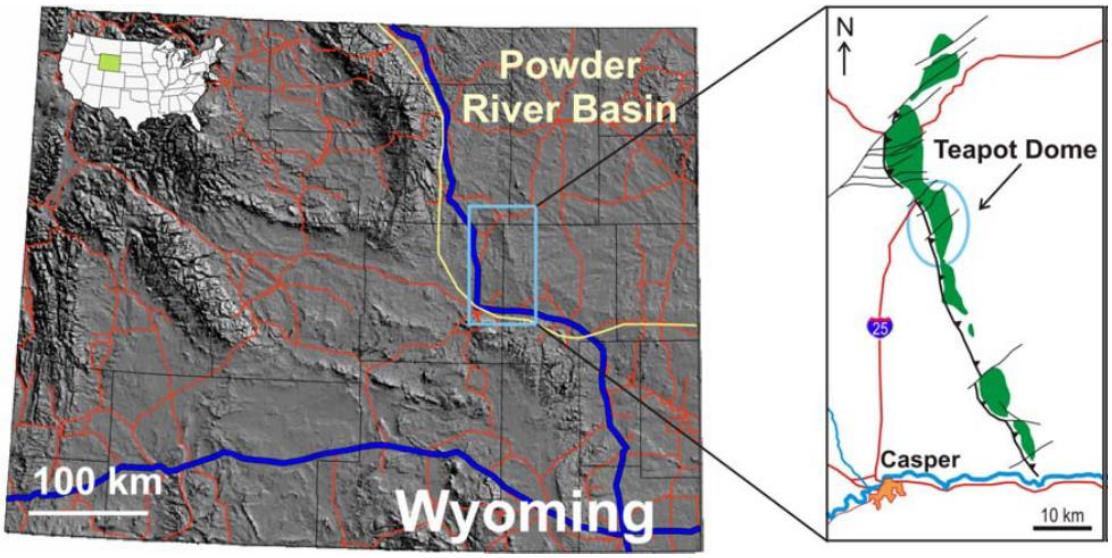

Figure 2-1: Teapot Dome is located along the southwestern edge of the Powder River Basin in northeastern part of Wyoming, USA (from Chiaramonte, 2008).

The domal structure is formed by compression from the southwest in response to the Late Cretaceous to mid-Tertiary Laramide Orogeny (Thom and Spieker, 1931). Teapot Dome is approximately 1585 m (5200 ft) above sea level and has a length of nearly 11.26 km (7 mi) and a width of approximately 4.0 km (2.5 mi). The trap consists of a three-way closure against a northeast–southwest-oriented oblique-slip fault (Cooper, 2000; Cooper et al., 2006). Teapot Dome is part of the larger Laramide structural complex that consists of three or more roughly north–south-trending anticlines (Doelger et al., 1993; Gay, 1999). The 3D seismic profiles across the area reveal that Teapot Dome formed over a northeast-dipping basement thrust with minor west–southwest reverse displacement (e.g., Smith, 2008).

The focus of this study is on the oil reservoir formed in the Tensleep Formation. The aeolian Tensleep Formation in Teapot Dome consists of shallow Aeolian sandstones, shallow marine carbonates, and extensive beds of low-permeability dolomicrites (Chiaramonte et al., 2011; Zahm and Hennings, 2009). The Tensleep Formation has an average matrix porosity of 8% (1%–19%) and permeability of 80 mD (0–110 mD) (Friedman and Stamp, 2006).

The age of the strata comprising Teapot Dome extends from the surface and near-surface Cretaceous to the Pre- Cambrian. The Pre-Cambrian basement is composed of granite (Figure 2-2b).

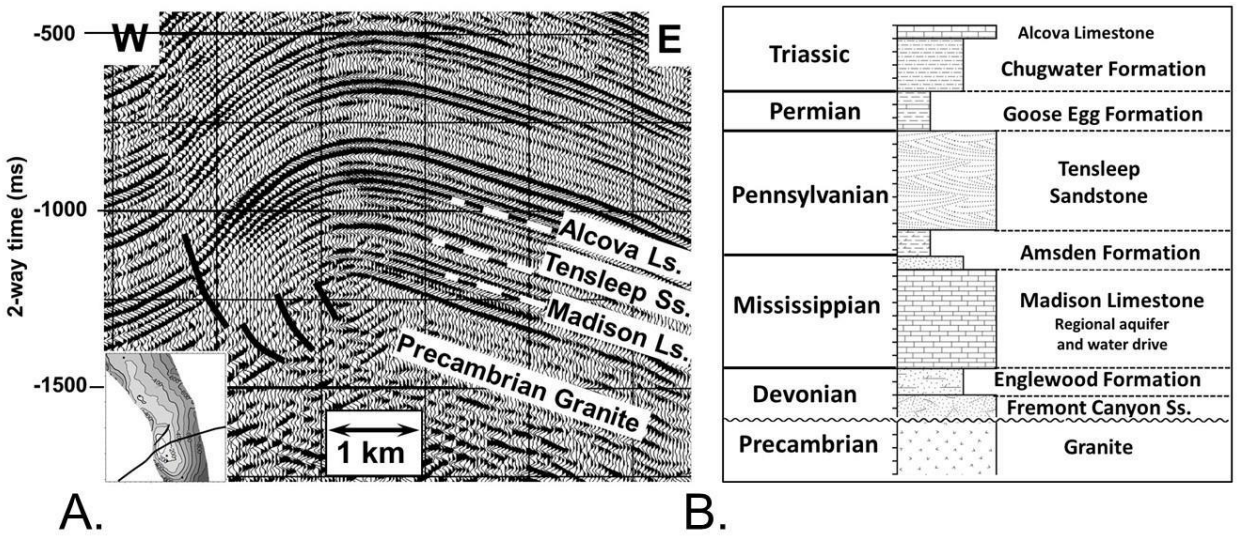

Figure 2-2: (a) West–east seismic section across the Teapot Dome. The reverse fault (shown by black line) has a southeast dip. (b) Stratigraphic column Precambrian- Triassic strata. The Madison Limestone is the regional aquifer that provides the water drive for the Tensleep reservoir, and the Goose Egg Formation is the seal (taken from Wilson et al., 2015).

The Mississippian-age Madison Limestone is a regional aquifer that provides the water drive for the Tensleep reservoir. The Chugwater and Permian Goose Egg Formations (a mixture of shale, siltstone with some sandstone) serve as the primary seal for the Pennsylvanian Tensleep reservoir (Figure 2-2b).

Fracture pattern in the Tensleep Formation

The Tensleep Formation is a tight NFR (Gilbertson, 2006; Schwartz, 2006; Smith, 2008; Lorenz and Cooper, 2013). The modeled DFN for the Tensleep reservoir developed in this study provides insights into possible CO_2-EOR strategies to extract residual oil from the Tensleep Formation at Teapot Dome, as well as in other

Tensleep reservoirs throughout Wyoming. The basis for the fracture model is tied to studies of field analogs. Cooper (2000) develops an idealized fracture model for the Late Cretaceous Parkman Sandstone member of the Mesaverde Formation based on a detailed study of outcrop fracture orientations to serve as a proxy for fracture patterns within the Tensleep reservoir and as

a basis for estimating their influence on permeability in the Tensleep Formation. He identifies three major fracture sets: hinge-parallel, hinge-perpendicular, and hinge-oblique with the hinge-parallel fractures as the dominant fracture set. Cooper (2000) uses the abutting relationship to establish the relative age of each fracture set. The hinge-parallel and hinge-perpendicular sets are interpreted to have developed coevally, whereas the hinge-oblique set predates the others. The hinge-oblique set may be a preexisting regionally distributed fracture set. Hinge-parallel and hinge-perpendicular fractures are common in Rocky Mountain anticlines (Thom and Spieker, 1931). Kennedy (2011) and Kennedy et al. (2012) carry out studies of fractures in several areas throughout the Laramide structures of Wyoming and Colorado. They also note the presence of three fracture sets: hinge-perpendicular, hinge parallel, and hinge-oblique sets.

The northwest hinge-oblique fracture set at Teapot Dome is believed to have developed during the early Laramide orogeny (Lorenz and Cooper, 2013). The hinge-oblique set is nearly parallel to the present-day S_{Hmax} trend inferred from induced fractures observed in wireline image logs from the field. Schwartz (2006) analyzes the wireline image log interpretations and compare fracture orientations interpreted from the wireline image logs with those observed at the surface by Cooper (2000). Schwartz (2006) notes that the dominant Tensleep fracture set observed in image logs through the reservoir consisted of hinge-oblique fractures with N60°W to N75°W trend (Figure 2-3).

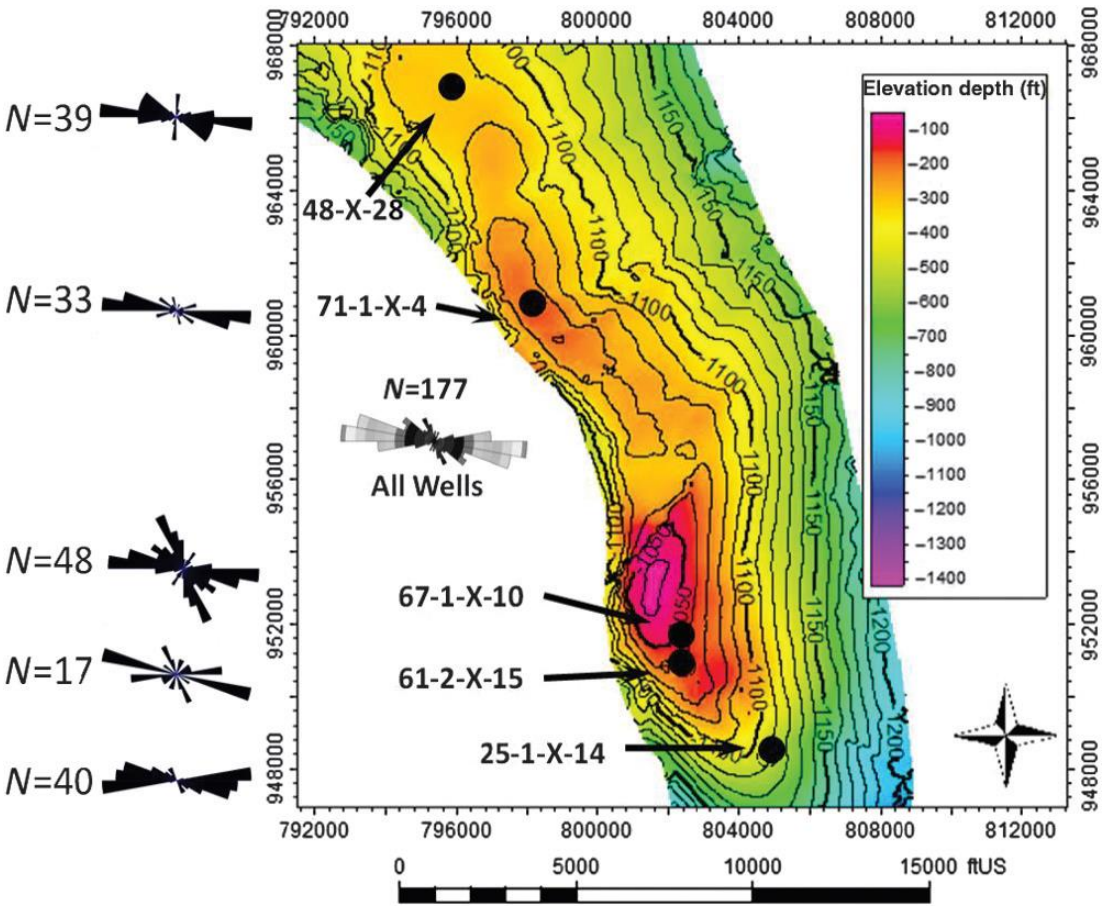

Figure 2-3: Location of wells with wireline image logs. Open fracture trends in the Tensleep Sandstone are plotted in rose diagrams for individual wells (at left). The rose diagram of open fractures (N=177) for all wells in Tensleep Sandstone is illustrated (from Wilson et al., 2015).

The hinge-oblique fracture set is interpreted to have been formed by horizontal compression oblique to the fold hinge and the compressive stress orientation producing Teapot Dome (Lorenz and Cooper, 2013). Lorenz and Cooper (2004) calculate an average fracture intensity of 0.65 m^{-1} (0.2 ft^{-1}) from the core through the Tensleep Sandstone at Teapot Dome. Wilson et al. (2015) incorporate relative intensities of 0.04 for hinge-perpendicular and 0.16 for hinge-parallel relative to the hinge-oblique fracture set in their DFN model. These relative intensities were based on the relative abundance of open fractures observed in the wireline image logs from the field.

Methods

Seismic approaches for fracture zone detection have been developed using prestack and poststack seismic data. This study focuses on the poststack attributes because of limited access to the prestack seismic data at Teapot Dome. Geometric attributes such as coherence and curvature have been used to identify fracture zones in poststack data (Lisle, 1994; Hennings et al., 2000). The curvature attribute can be related to the fracture intensity under three assumptions: The brittle rock fractures in response to applied stress, an increase in strain can be implied from an increase in curvature, and an increase in strain implies an increase in fracture intensity (Nelson, 2001). In this study, we also use curvature as a tool for fracture-zone detection with the additional assumptions that fracture zones are seismically detectable with widths comparable in size with the Fresnel zone diameter. We also assume that these fracture zones contain multiple fracture sets as noted in the field studies presented by Wilson et al. (2015).

The workflow developed in this study starts with application of SSB on the 3D poststack migration volume. The most negative curvature is computed on the SSB volume. Minimum similarity computations enhance local discontinuity in the most negative curvature volume. Finally, the edge-illumination process is used to enhance discontinuities, which are then used to distribute the fracture intensity through the model DFN.

Initially, we use SSB to enhance the seismic resolution for more robust fracture detection (Lancaster and Whitcombe, 2000). The process is designed to recover higher frequency content using the spectral characteristics of the reflection coefficient series over the interpreted bandwidth of usable signal (Figures 2-4 and 2-5).

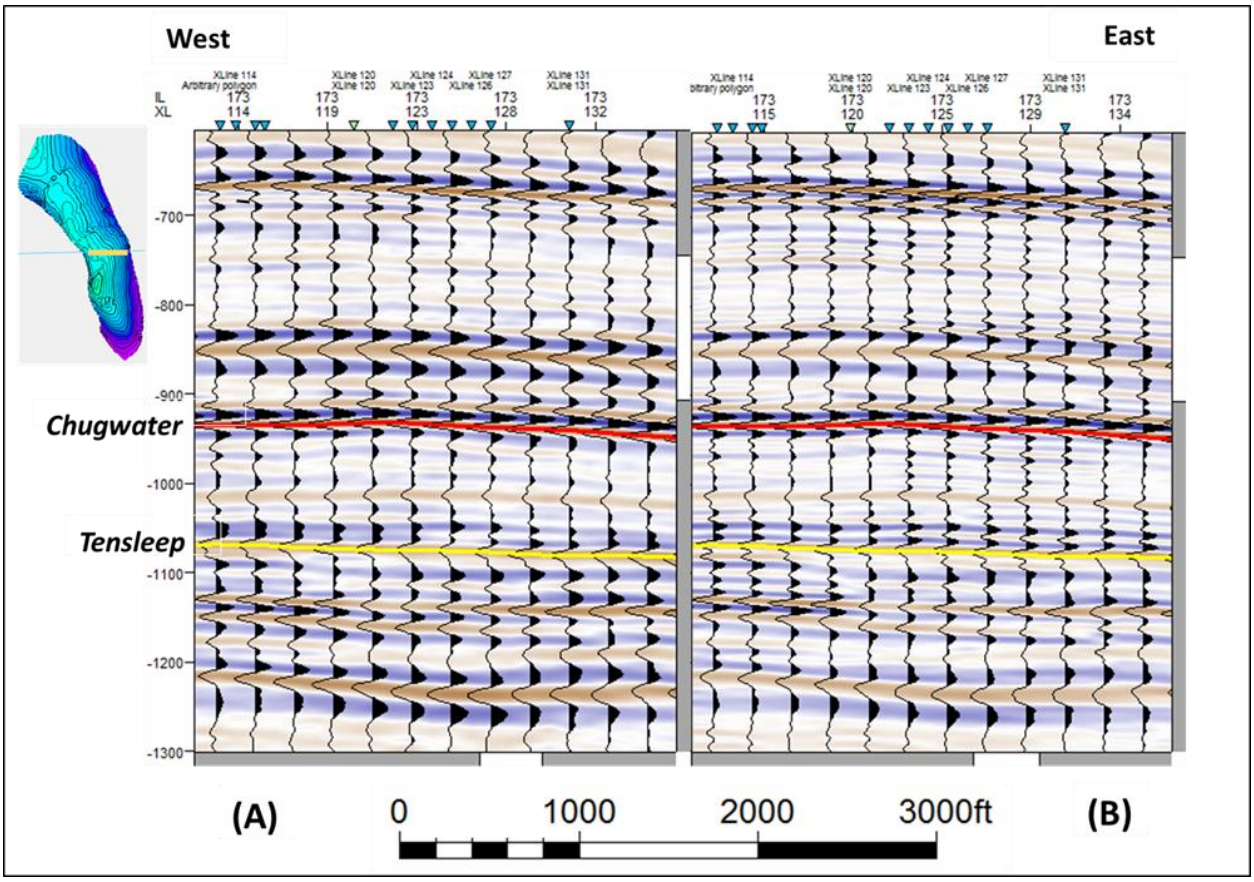

Figure 2-4: (a) Crossline 173 in the west–east direction for regular migrated stack seismic data. (b) Crossline 173 in the west–east direction for the SSB cube. Note that the higher frequencies are present right above the Tensleep reservoir and within the reservoir.

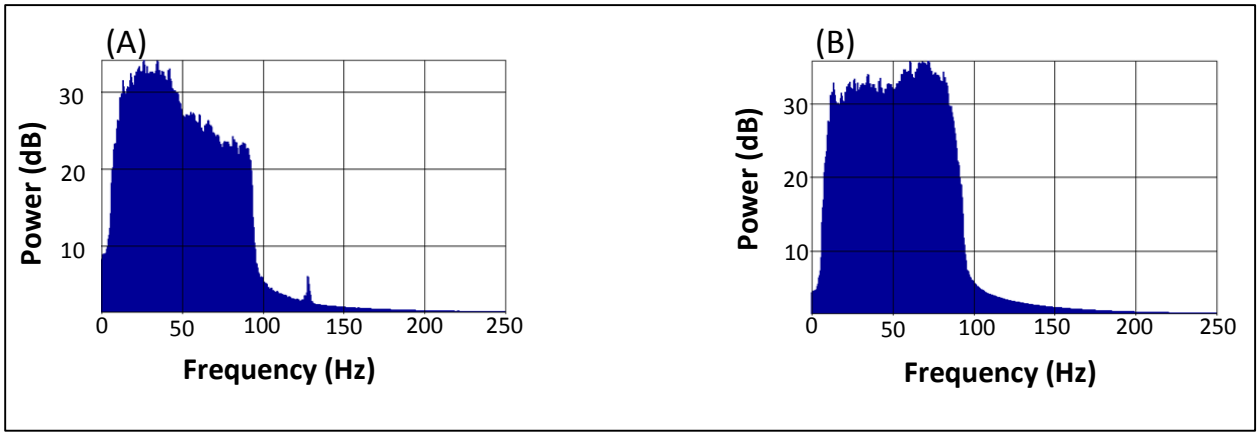

Figure 2-5: (a) Amplitude spectrum of seismic data. Note that high-frequency components have relatively low amplitude. (b) The spectrum of the seismic data after SSB. Note that high-frequency amplitudes are increased relative to the lower frequency content of the spectrum.

Empirical and theoretical studies showed that reflection coefficient series have spectra that can be described using a power law in which the spectral amplitude varies as f^{β}, where β is a positive

constant and f is the frequency (Velzeboer, 1981; Walden and Hosken, 1985). Lancaster and Whitcombe (2000) illustrate that acoustic-impedance spectra can also be described as f^{α}, where α is a negative constant. The exponents α and β are nearly constant within the local field areas. Thus, inverted seismic data should have spectral trends that are similar to spectra of impedance logs in the area. The SSB is carried out using an operator designed in the frequency domain that maps the mean seismic spectrum to the band-limited mean earth reflectivity spectrum (based on the well-log data). The operator is applied to the seismic data in the time domain to yield the SSB cube. The dominant frequency of the wavelet extracted from the SSB cube within the reservoir zone is 60 Hz and significantly higher than the dominant frequency derived from the input migrated stacked data of 44 Hz (Figure 2-5). Following the SSB step, the cube was depth converted using the velocity model developed by Wilson et al. (2013).

Fractures can alter the shear strength and elastic parameters of the rock (Goodman 1976; Brown and Scholz, 1986). The effect of the fracture zone on seismic velocities and attenuation has been modeled as a displacement discontinuity (Lutsh, 1959; Schoenberg, 1980; Cook, 1992). An increase in the fracture intensity reduces the P-wave interval velocity of a given stratigraphic interval particularly for P-waves traveling perpendicular to the fractures. Consequently, traveltimes through a simply fractured medium may increase along azimuths normal to the fracture strike compared with those parallel to the fracture strike or in a non-fractured medium. The influence on velocity will vary also with the fluid type filling the fracture: water, oil, or gas (Boadu and Long, 1996). Wilson et al. (2015) note that fracture zones observed in the Tensleep Formation exposures in Fremont Canyon, Wyoming are often wider than the Fresnel zone diameter and contain multiple fracture sets. Thus, intensely fractured zones containing multimodal fracture azimuth distributions may influence the traveltime and amplitude in the standard all-azimuth stack.

The time delay associated with decreased velocity across Fresnel zone scale fracture zones may be observable for thicker reservoirs such as the Tensleep, which is 91.4– 107 m (300–350 ft) thick in the area. The most negative curvature (short wavelength) may detect these time delays and other velocity changes associated with stress, porosity, diagenetic alteration, fluid content, and saturation (Chopra and Marfurt, 2007b; Gorbe et al., 2010). Intensely fractured zones may also form along the hinges of local folds with synclinal deformation identifiable using the most negative curvature. We also note that, in the field, zones of more intense fracturing are commonly not associated with local flexure (e.g., Wilson et al., 2015, their Figure 8). Curvature measures the degree of bending along a seismic surface or between voxels in a seismic volume (Roberts, 2001). Other studies discuss the use of various curvature attributes to detect fracture zones (e.g., Lisle, 1994; Hart et al., 2002; Hunt et al., 2010; Gao, 2013; Di and Gao, 2014). In this study, local velocity sags or flexures are extracted using the minimum similarity attribute of the most negative curvature volume. Similarity is a form of semblance-based coherence (Chopra and Marfurt, 2007a) that computes how much two or more trace segments are comparable. A similarity value of one suggests adjacent trace waveforms are equivalent, whereas zero similarity indicates that adjacent traces are completely dissimilar. Samples of a trace within a time gate are considered as components of a vector in hyperspace.

The similarity is one minus the Euclidean distance between the vectors (two trace segments) normalized to the sum of the length of vectors (Tingdahl and de Rooj, 2005). Traces of opposite polarity, for example, have a normalized Euclidean distance of one and similarity of zero.

Minimum similarity of the most negative curvature attribute was calculated using a short sliding window. The response of individual traces is compared with adjacent traces. Thus, the similarity was calculated between a central trace segment (vector) and the eight adjacent traces of the most

negative curvature cube. The minimum value of these eight similarity pairs was output for the central trace segment. Hence, the minimum similarity of the most negative curvature highlights traces with a large negative curvature that are adjacent to traces with little to no negative curvature and are interpreted to result from local velocity or structural sag. Edge illumination (ant tracking; Pederson et al., 2002, 2003) is then applied as the final step to the minimum similarity volume. The edge illumination process extracts persistent alignments of discontinuity in the minimum similarity volume. Discontinuities in this case represent discontinuities in the similarity of curvature or zones of very low or no similarity in curvature relative to adjacent traces. These alignments of discontinuity are interpreted to be associated with zones of higher fracture intensity.

Results and discussion

The fracture intensity attribute developed in this study reveals the presence of hinge-oblique discontinuities. These discontinuities are interpreted to represent zones of more intensely fractured reservoir. Although we cannot determine which discontinuities are velocity sags or flexures, the orientations of the extracted seismic discontinuities are close to those observed in wireline image logs from five wells (Figure 2-6).

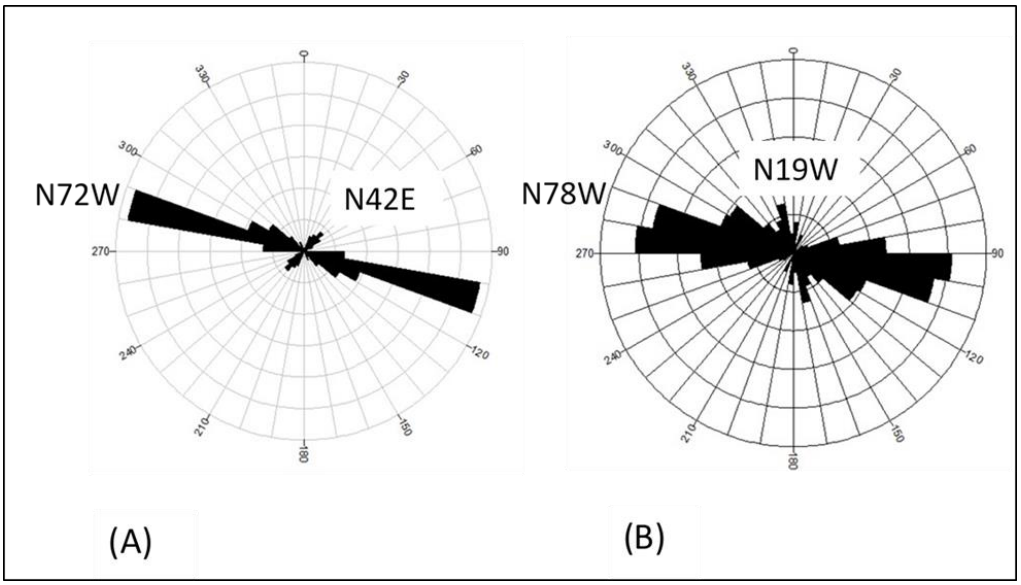

Figure 2-6: (a) Seismic discontinuities interpreted from the fracture intensity attribute. The dominant set is in the hinge-oblique direction of N72°W. The other set is N44°E, which shows oblique slip faults. (b) Rose diagram of fracture orientation interpreted from wireline image logs of five wells in the Tensleep interval. Note that the dominant set is hinge oblique at N78°W.

Discontinuities identified by this workflow fall into two sets: the N72°W set, which is close to the open fracture set identified from wireline image logs of N78°W, and the other set with N44°E trend was also observed by Wilson et al. (2015) and parallels the trend of oblique slip faults mapped at the surface by Cooper (2000) and interpreted in the 3D seismic (Friedman and Stamp, 2006). The northeast-trending discontinuities are oriented approximately 60° relative to present-day S_{Hmax}. However, S_{Hmax} during the Laramide was probably oriented closer to the east–northeast, resulting in fold formation and oblique slip on these northeast-trending faults and fracture zones. Shear displacements along these trends may have produced a low-permeability fault core surrounded by amore permeable open fracture halo (Wilson et al., 2015). Their fracture intensity attribute introduced low-permeability streaks in areas of highest discontinuity concentrated mainly along the northeast oblique-slip trend. These barriers coincided with compartmentalization inferred from production distribution.

The distribution of high-intensity zones extracted using the approach developed in this study is compared with the cumulative production data from the wells. Although the production might be

controlled by perforation intervals, shut-ins, bottom-hole pressure, subseismic anisotropy around each well, the type of completion, etc., some general trends can be observed from the modeled fracture intensity attribute (Figure 2-7a and 2-7b).

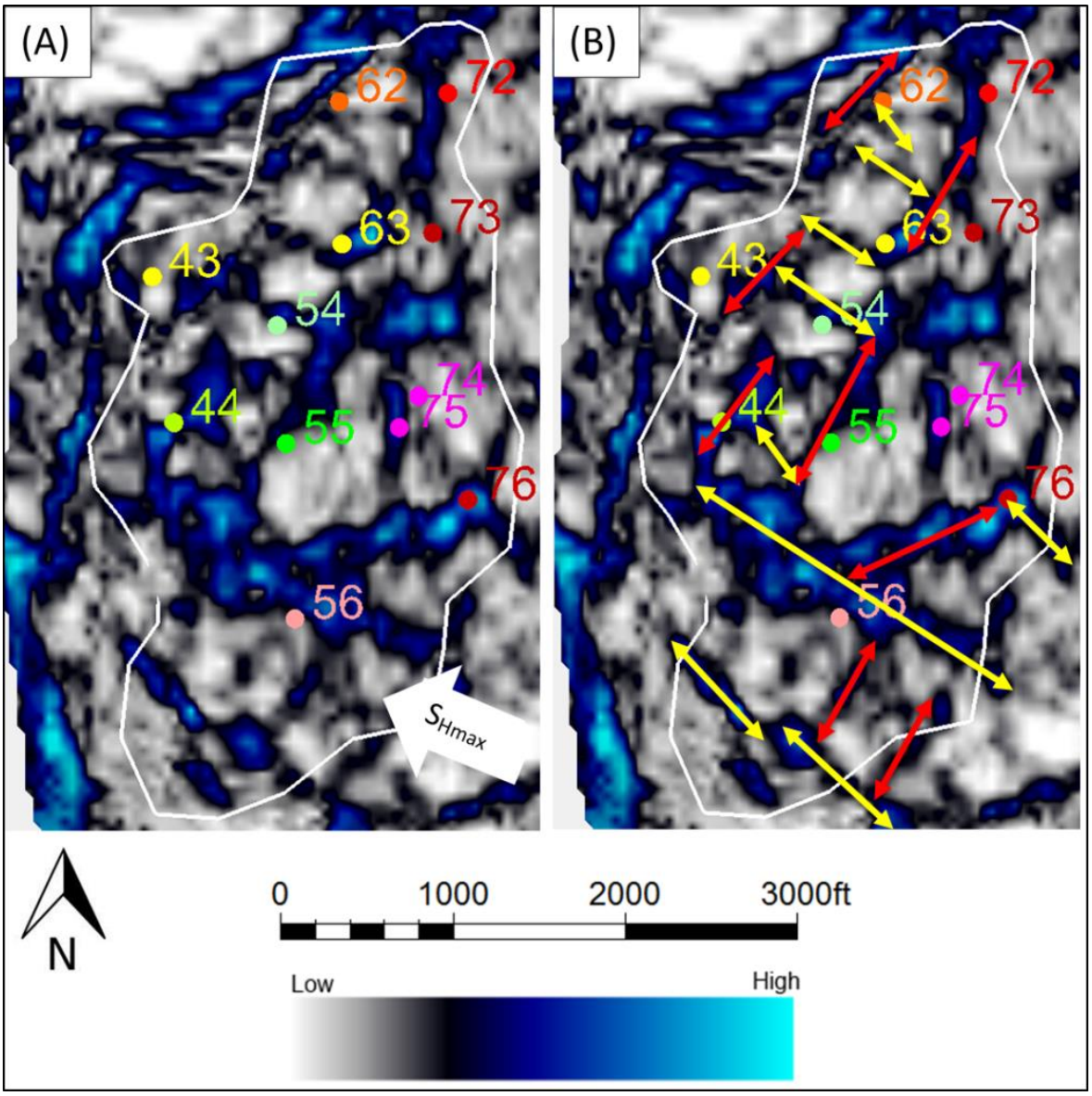

Figure 2-7: (a) The fracture intensity distribution is shown in the culmination at the Tensleep horizon along with the producing wells. (b) Discontinuity interpretation based on the fracture intensity distribution shows partitioning by the northeast and northwest discontinuities.

Generally, wells that are located on northwest-oriented discontinuities are more productive than others (e.g., wells 56 and 54). In addition, wells located on the intersection of northwest and northeast-oriented discontinuities are also productive wells (e.g., 62, 63, 44, and 76; Figure 2-8). Different production start points and various shut-ins in the production history do not allow a well by well comparison with the fracture intensity attribute.

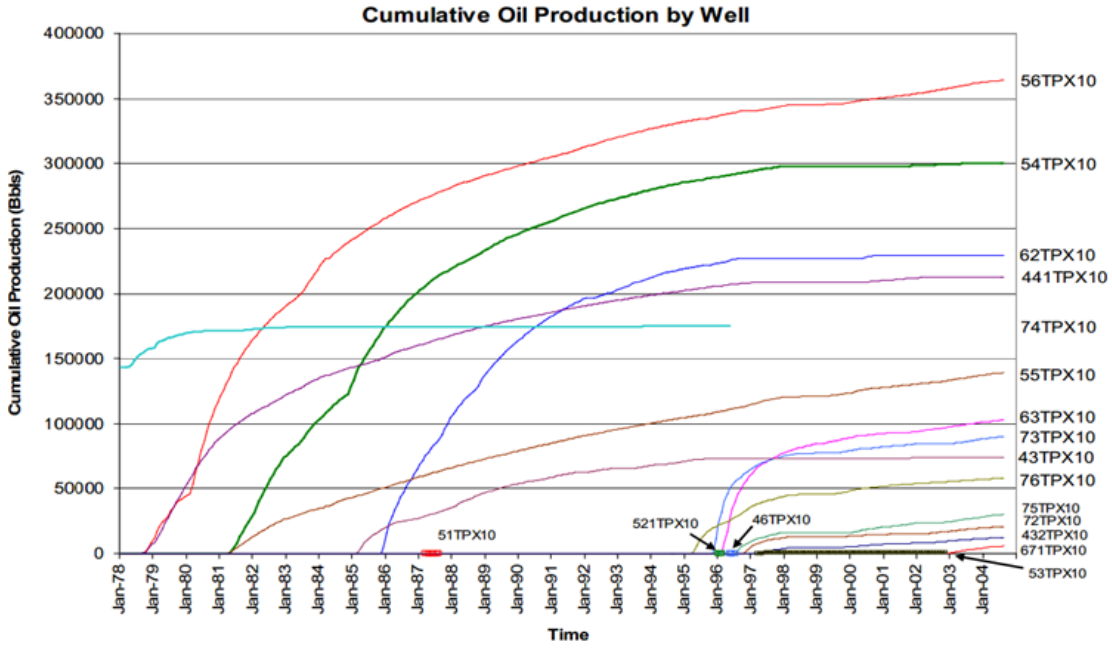

Figure 2-8: Cumulative oil production by well in the Tensleep reservoir in Teapot Dome. Wells 56-TPX-10 and 54-TPX-10 are the most prolific wells, which are located on northwest discontinuities (from Smith, 2008).

The discontinuities extracted in this study are interpreted to represent zones of increased fracture intensity containing multiple fracture sets. The northwest hinge-oblique fractures are consistently found to be the most abundant in the field analog, as well as in the wireline image logs. It may be that the northwest hinge-oblique set is also dominant within the fracture zones interpreted in this study. The trend of present-day S_{Hmax} inferred from induced fracture orientations observed in the wireline image logs is also nearly parallel to the hinge-oblique fractures identified in the reservoir (Chiaramonte, 2008; Wilson et al., 2015). The trend of S_{Hmax} is likely to keep the northwest hinge-oblique fractures open throughout the area and within the northwest-trending discontinuities and

may explain higher water and oil production in wells located along these discontinuities (Figures 2-7 and 2-8). Moreover, the overlay of the log of 10-year cumulative oil production suggests that the fracture intensity may control the production in this NFR type II reservoir (Figure 2-9a and 2-9b).

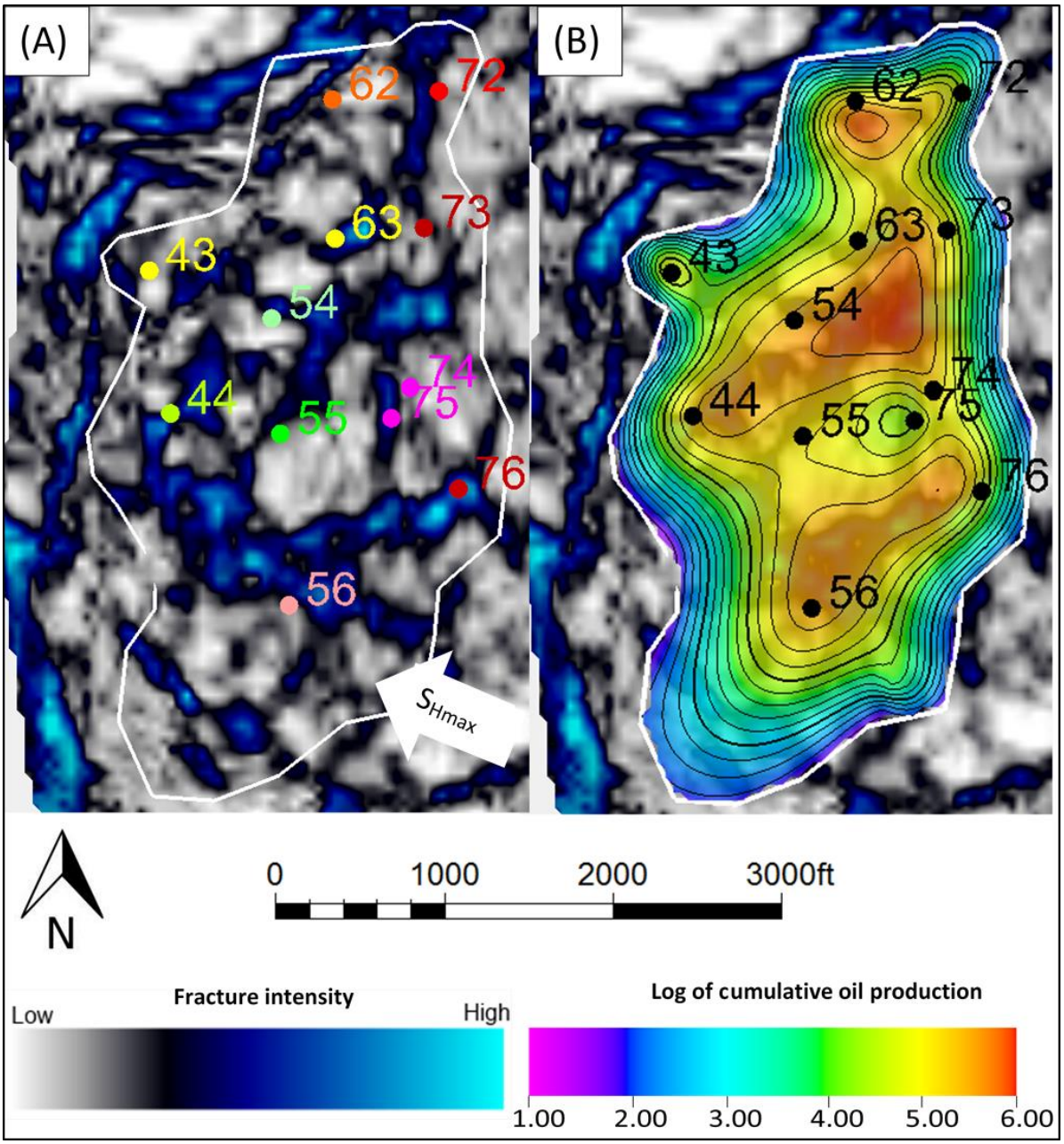

Figure 2-9: (a) Fracture intensity distribution is shown in the culmination on the Tensleep horizon along with producing wells. (b) Fracture intensity attribute overlaid by log of cumulative oil production (barrels). The fracture intensity may control the production in this field.

Suggestions for further study

The fracture intensity attribute developed in this study suggests that wells located on northwest-trending high-intensity discontinuities were among the better producing wells in the reservoir. Additional work is needed to calibrate the production history data to fracture permeability. Calibration could be achieved through continuous fracture modeling, which considers the reservoir permeability as a sum of matrix permeability (from core data) and fracture permeability (Ouenes et al., 2010). The fracture permeability is related directly to the fracture intensity. Iterative adjustments to this relationship in the final model DFN will be made during the production history matching process. Sensitivity analysis can also be used to refine interrelationships and their influence on production models. Adjustments to model parameters can be calibrated by minimizing the difference between the production history data and predicted production.

Conclusion

The most negative curvature attribute can be combined with the similarity attribute to generate an edge-enhanced volume for discontinuity extraction using an edge-illumination process. Extracted discontinuities are interpreted to result from local velocity sag produced across more intensely fractured zones or flexures. Discontinuities extracted from the seismic data are dominated by a northwest trend similar to the trend of the dominant northwest hinge-oblique fracture set identified in several wireline image logs available from the field. The modeled discontinuities are nearly parallel to S_{Hmax} and are likely to remain open during CO_2-EOR operations.

The comparison of modeled intensity and cumulative production data indicates that better producing wells are located along these northwest-trending discontinuities. However, fractures and

fracture zones can impose risks to and opportunities for production optimization. Along the northwest direction, fractures may enhance production but could also lead to early breakthrough. The complexity of fracture patterns in this reservoir presents challenges for CO_2-EOR. Using existing wells drilled in the northwest-oriented seismic discontinuities as injectors may result in early breakthrough. Therefore, injectors should not be placed on the northwest-trending seismic discontinuities. However, analysis of field analogs indicates that fracture lengths are largely concentrated between 5 and 15 m (16.4 and 49.2 ft), so they are unlikely to provide direct breakthrough pathways between injection and production wells separated by several hundred meters. The strategic location of injection wells should be refined through compositional flow simulation and rock-physics analysis. The applicability of this approach extends beyond Teapot Dome to EOR in residual oil zones in this and other tight NFR.

Acknowledgments

We would like to thank the Rocky Mountain Oil Testing Center, which provided us with the 3D seismic and log data for Teapot Dome. This study would not have been possible without the wireline image log interpretations of R. Koepsell. The use of Petrel from Schlumberger, OpendTect from dGB Earth Sciences, and FracMan from Golder Associates is greatly appreciated, and it made the analysis presented in this paper possible. We also extend our appreciation to C. Sullivan and two anonymous reviewers and the associate editor; their comments and suggestions significantly improved the paper.

REFERENCES

Allan, J. Q. S., 2003, Controls on recovery factor in fractured reservoirs: Lessons learned from 100 fractured fields: SPE Annual Technical Conference and Exhibition, 84590.

Boadu, F. K., and L. T. Long, 1996, Effects of fractures on seismic-wave velocity and attenuation: Geophysical Journal International, 127, 86–110, doi: 10.1111/j.1365-246X.1996.tb01537.x.

Brown, S. R., and C. H. Scholz, 1986, Closure of rock joints: Journal of Geophysical Research, 91, 4939–4948, doi: 10.1029/JB091iB05p04939.

Chiaramonte, L., 2008, Geomechanical characterization and reservoir simulation of a CO_2 sequestration project in a major oil field, Teapot Dome, WY: Ph.D. dissertation, Stanford University.

Chiaramonte, L., M. Zoback, J. Friedmann, V. Stamp, and C. Zahm, 2011, Fracture characterization and fluid flow simulation with geomechanical constraints for a CO_2-EOR and sequestration project Teapot Dome Oil Field, Wyoming, USA: Energy Procedia, 4, 3973–3980, doi: 10.1016/j.egypro.2011.02.337.

Chopra, S., and K. J. Marfurt, 2007a, Seismic attributes for prospect identification and reservoir characterization: SEG, Geophysical Developments 11.

Chopra, S., and K. J. Marfurt, 2007b, Seismic curvature attributes for mapping faults/fractures, and other stratigraphic features: CSEG Recorder, 32, 37–41.

Cook, N. G. W., 1992, Natural joints in rock: Mechanical, hydraulic and seismic behavior and properties under normal stress: International Journal of Rock Mechanics and Mining Sciences & Geomechanics Abstracts, 29, 198–223, doi: 10.1016/0148-9062(92)93656-5.

Cooper, S. C., L. B. Goodwin, and J. C. Lorenz, 2006, Fracture and fault patterns associated with basement-cored anticlines: The example of Teapot Dome, Wyoming: AAPG Bulletin, 90, 1903–1920, doi: 10.1306/06020605197.

Cooper, S. P., 2000, Deformation within a basement cored anticline Teapot Dome, Wyoming: M.S. thesis, New Mexico Institute of Mining and Technology.

Di, H., and D. Gao, 2014, A new analytical method for azimuthal curvature analysis from 3D seismic data: 84th Annual International Meeting, SEG, Expanded Abstracts, 1634–1638, doi: 10.1190/segam2014-0528.1.

Doelger, M. J., and D. M. Mullen, 1993, Near shore marine sandstone: Atlas of major Rocky Mountain gas reservoirs: New Mexico Bureau of Mines and Mineral Resources.

Friedmann, S. J., and V. W. Stamp, 2006, Teapot Dome: Characterization of a CO_2 enhanced oil recovery and storage site in Eastern Wyoming: Environmental Geosciences, 13, 181–199, doi: 10.1306/eg.01200605017.

Gao, D., 2013, Integrating 3D seismic curvature and curvature gradient attributes for fracture characterization: Methodologies and interpretational implications: Geophysics, 78, no. 2, O21–O31, doi: 10.1190/geo2012- 0190.1.

Gay, S. P., Jr., 1999, An explanation for "4-way closure" of thrust fold structures in the Rocky Mountains, and implications for similar structures elsewhere: The Mountain Geologist, 36, 235–244.

Gilbertson, N. J., 2006, 3D geologic modeling and fracture interpretation of the Tensleep Sandstone, Alcova anticline, Wyoming: M.S. thesis, Colorado School of Mines.

Goodman, R. E., 1976, Methods of geological engineering: West Publishing.

Gorbe, M., J. C. Pashin, and R. L. Dodge, eds., 2010, Carbon dioxide sequestration in geological media: State of the science: AAPG, Studies in Geology 59.

Hart, B. S., R. A. Pearson, and G. C. Rawling, 2002, 3D seismic horizon-based approaches to fracture-swarm sweet spot definition in tight-gas reservoirs: The Leading Edge, 21, 28–35, doi: 10.1190/1.1445844.

Hennings, P. H., J. E. Olson, and L. B. Thompson, 2000, Combining outcrop data and three-dimensional structural models to characterize fractured reservoirs: An example from Wyoming: AAPG Bulletin, 84, 830–849, doi: 10.1306/A967340A-1738-11D7-8645000102C1865D.

Hunt, L., S. Reynolds, T. Brown, S. Hadley, J. Downton, and S. Chopra, 2010, Quantitative estimate of fracture density variations in the Nordegg with azimuthal AVO and curvature: A case study: The Leading Edge, 29, 1122– 1137, doi: 10.1190/1.3485773.

Kennedy, L., 2011, Laramide transpression and block rotation followed by northeast-southwest extension, southeast Wind River Basin area, Wyoming: M.S. thesis, University of Wyoming.

Kennedy, L., E. Erslev, and K. Aydinian, 2012, Mapping Rocky Mountain Fractures: GIS methodsfor resource plays, http://www.searchanddiscovery.com/pdfz/documents/ 2012/ 41031kennedy/ndx_kennedy.pdf.html, accessed 18 February 2015.

Lancaster, A., and D. Whitecombe, 2000, Fast-track 'coloured' inversion: 70th Annual International Meeting, SEG, Expanded Abstracts, 1572–1575.

Lisle, R. J., 1994, Detection of zones of abnormal strains in structures using Gaussian curvature analysis: AAPG Bulletin, 78, 1811–1819.

Lorenz, J. C., and S. P. Cooper, 2013, Natural fractures in folded sandstones of the Tensleep Formation, Wyoming: in C. Knight, and J. Cuzella, eds., Application of structural methods to Rocky Mountain hydrocarbon exploration and development: AAPG, Studies in Geology, 65, 175–213.

Lutsh, A., 1959, The experimental determination of the extent and degree of fracture of rock faces by means of an ultrasonic reflector method: Journal of the South African Institute of Mining and Metallurgy, 59, 412–429.

Nelson, R., 2001, Geologic analysis of naturally fractured reservoirs: Elsevier.

Ouenes, A., T. Anderson, D. Klepacki, A. Bachir, D. Boukhelf, U. Araktingi, M. Holmes, B. Black, and V. Satamp, 2010, Integrated characterization and simulation of the fractured Tensleep reservoir at Teapot Dome for CO_2 injection design: SPE Western Regional Meeting, 132404.

Pedersen, S., T. Randen, L. Sonneland, and O. Steen, 2002, Automatic fault extraction using artificial ants: 72nd Annual International Meeting, SEG, Expanded Abstracts, 512–515, doi: 10.1007/3-540-26493-0_5.

Pedersen, S., T. Skov, A. Hetfield, P. Fayamendy, T. Randen, and L. Sonneland, 2003, New paradigm of fault interpretation: 73rd Annual International Meeting, SEG, Expanded Abstracts, 350–353.

Roberts, A., 2001, Curvature attributes and application to 3D interpreted horizons: First Break, 19, 85–100, doi: 10 .1046/j.0263-5046.2001.00142.x.

Schoenberg, M., 1980, Elastic wave behavior across linear slip linear slip interfaces: Journal of the Acoustical Society of America, 68, 1516–1521, doi: 10.1121/1.385077.

Schwartz, B., 2006, Fracture pattern characterization of the Tensleep Formation, Teapot Dome, Wyoming: M.S. thesis, West Virginia University.

Smith, V. L., 2008, Modeling natural fracture networks: Establishing the groundwork for flow simulation at Teapot Dome, Wyoming: M.S. thesis, West Virginia University.

Thom, W., Jr., and E. Speiker, 1931, The significance of geologic conditions in Naval Petroleum Reserve No. 3, Wyoming: United States Geological Survey.

Tindahl, K. M., and M. de Rooj, 2005, Semi-automatic detection of faults in 3D seismic data: Geophysical Prospecting, 53, 533–542, doi: 10.1111/j.1365-2478.2005.00489.x.

Velzeboer, C. J., 1981, The theoretical seismic reflection response of sedimentary sequence: Geophysics, 46, 843–853, doi: 10.1190/1.1441222.

Walden, A. T., and J. W. J. Hosken, 1985, An investigation of the spectral properties of primary reflection coefficients: Geophysical Prospecting, 33, 400–435, doi: 10 .1111/j.1365-2478.1985.tb00443.x.

Wilson, T., V. Smith, and A. Brown, 2013, Developing a strategy for CO_2-EOR in an unconventional reservoir using 3D seismic attribute workflows and fracture image logs: 83rd Annual International Meeting, SEG, Expanded Abstracts, 2563–2567.

Wilson, T., V. Smith, and A. Brown, 2015, Developing a model discrete fracture network, drilling and EOR strategy in an unconventional naturally fractured reservoir using integrated field, image log and 3D seismic data: AAPG Bulletin, 99, 735–762, doi: 10.1306/10031414015.

Zahm, C. K., and P. H. Hennings, 2009, Complex fracture development related to stratigraphic architecture: Challenges for structural deformation prediction, Tensleep Sandstone at the Alcova anticline, Wyoming: AAPG Bulletin, 93, 1427–1446, doi: 10.1306/08040909110.

Chapter 3: The Structured Gridding Implications for Upscaling Model Discrete Fracture Networks (DFN) Using Oda's Method[2]

Abstract

Upscaling of fracture permeability in a discrete fracture network (DFN) for a dual porosity model can be undertaken using Oda's method. In this study we show that grid orientation can produce significant differences in single-phase (water) production volumes estimated through flow simulation in dual porosity models when using Oda's method. A five layer synthetic model in a 500ft water zone includes thirteen vertical wells evenly distributed and perforated from top to the bottom. 10ft by 10ft structured gridding is performed in six directions: 0°, 15°, 30°, 45°, 60° and 75° counter-clockwise relative to the north. Thus, six synthetic models are generated which are only different in grid orientation. The model DFN used in this study consists of three sets: a dominant, high intensity N76°W and two lower-intensity sets that strike N28°W and N75°E. The orientation and intensity of these three fracture sets are based on the fracture sets observed in the Tensleep Formation at Teapot Dome, Wyoming, USA.

A computer code was developed for the fracture model to study the effect of grid orientation (0° to 75°) on the upscalled permeability tensor for these 3 fracture sets in just a single grid block using Oda's method. Results show that the calculated permeability tensors have maximum geometric mean for the non-zero permeability components ($k_{xx}, k_{yy}, k_{zz}, k_{xy}$) when the dominant fracture set cuts diagonally through the cell at 45° relative to the grid cell principal directions

[2] *Kavousi, P., 2015, The structured gridding implications for upscaling model discrete fracture networks (DFN) using Oda's method: SPE Reservoir Evaluation and Engineering-Reservoir Engineering (In Review).*

(i, j). The geometric mean of the permeability tensor components falls to a minimum when the dominant fracture set is parallel to either grid wall (i or j principal directions).

The single-phase (water) flow simulation for the six synthetic models reveals that the production varies in proportion to the geometric mean of the permeability tensor with grid rotation. Streamline simulation is also computed through the rotated grids. This simulation reveals the presence of multiple flow directions. Fluid flow directions vary with the fracture permeability tensor eigenvectors as the grid is rotated.

Previous studies suggest that Oda's method is limited to well-connected fracture networks. This research reveals the additional shortcoming of variability of simulated production with grid orientation even though fractures are well connected.

Introduction

Irregular fracture networks and complex fluid transfer from matrix to fractures makes fluid flow in naturally fractured reservoirs (NFR) more complex than conventional reservoirs (Sarma 2003). Well productivity and recovery efficiency are directly influenced by permeability enhancement from natural fractures in NFRs (van Golf-Racht 1982). Fractures typically have much higher permeability than matrix and are the major flow paths in NFRs. However, fractures can also form permeability barriers when secondary mineralization or infilling of fine-grained materials occurs in the formerly open fractures (Narr et al. 2006). The complexity of the reservoir fracture network must be accurately defined and incorporated in models to ensure reasonable approximation of production history through simulation. Wireline image logs, outcrop studies, core observations, and seismic data analysis provide direct and indirect measurements of fracture properties at different scales. Observations made at these different scales must be integrated to

provide a representative model of the reservoir DFN (Wilson et al. 2015; Kavousi and Wilson 2015). Fracture spacing, aperture, and length distributions can be incorporated in the reservoir model using wireline image logs, core data, and field studies (Cooper 2000; Wilson et al. 2015). While uncertainties remain, these models are consistent with observations made at a variety of scales.

Barenblatt and Zheltov (1960) introduced dual porosity (DP) concepts for fluid flow simulation in fractured reservoirs using a transfer function to model the flow between fracture and matrix medium. Warren and Root (1963) used a simplified dual porosity version of Barenblatt and Zheltov (1960) and introduced dual porosity model to the petroleum industry for single phase flow and Kazemi et al. (1976) extended it to two-phase flow. Thomas (1983) developed the dual porosity model for three-phase flow in fractured reservoirs. The key feature of their model was that flow simulation incorporates coupled flow continua: one for the matrix and the other for the DFN. Fluid flow through the fracture network along with flow from the matrix into the fracture network can be modeled with a transfer function referred to as the shape factor (Warren and Root 1963; Kazemi 1976; Penuela et al. 2002; Sarma and Aziz 2006). Efforts to compute the upscaled permeability tensor are documented by several researchers (van Golf-Racht 1982; Dershowitz 1984; Long 1985; Clemo and Smith 1997; Dershowitz et al. 2000; Karimi-Fard et al. 2004, 2006). Computation of the permeability tensor can be carried out by unstructured discretization of the fractures in grids using a finite difference or finite element approach (Baca et al. 1984; Juanes et al. 2003; Karimi-Fard and Firoozabadi 2003; Sarda et al. 2002). The finite element methods are usually computationally more expensive than finite difference methods (Karimi-Fard et al. 2004).

Karimi-Fard et al. (2004) used an unstructured control volume finite difference approach with two-point flux approximation to simulate the flow in 2D and 3D discrete fracture model (DFM).

Although DFM approaches provide a more accurate estimate of the permeability tensors, they are computationally expensive and unpractical for use in large fields (Li et al. 2015; Karimi-Fard et al. 2006). Computational constraints limit the number of fractures in such models to from 10^4 to 10^5 fractures (Dershowitz et al. 2000). In addition, unstructured gridding of large number of fractures increases the complexity of computations.

Dershowitz (1984) explored a finite element procedure to calculate the dual porosity (DP) parameters for a fractured porous medium. Fractures are discretized into a finite-element mesh. In this approach constant pressure boundary conditions are applied to two opposing faces of the DP grid cell, while no flow boundary conditions for other faces of the grid. Steady state flow through the grid cell is modeled and used to calculate a permeability tensor based on Darcy's law. Derivation of permeability tensor using flow simulation is sensitive to boundary conditions, single or dual phase, and single or dual porosity (Dershowitz et al. 2000).

Karimi-Fard et al. (2006) used the DFM and introduced a multiple sub-regions (MSR) approach to resolve the dynamic interactions within the matrix to calculate coarse-scale flow parameters of fracture-fracture, matrix-fracture, and matrix-matrix flow for a dual porosity model. Geometry of the subregions and dynamic parameters are determined by calculating local flow through discrete fracture model using the approach previously introduced by Karimi-Fard et al. (2004). Gong et al. (2008) extended MSR approach by introducing gravitational effects on phase segregation.

The earlier approach proposed by Oda (1985) calculated the permeability tensor by introducing the fracture tensor, which expresses fracture flow as a vector along fracture's unit normal and only depends on the geometry of the fractures (aperture, size and orientation). Oda's approach is commonly available in commercial software as a fast algorithm to calculate fracture permeability

tensors. However, this method does not account for fracture network connectivity and is limited to well-connected fracture networks (Dershowitz et al. 2000). Oda's method is a fast approach to estimate permeability tensor when the medium is highly fractured (Dershowitz et al. 2000; Gupta et al. 2001).

We will show in this paper that although Oda's method provides rapid estimation of the permeability tensor, it is highly dependent on the grid orientation. This uncertainty translates into significant variation in the results of DP production simulation. In this study a dual porosity simulation is conducted for model grid cells rotated relative to the DFN. The results reveal significant variation in simulated production with grid orientation. The results reveal that simulated production in a one–phase (water) model varies directly with the geometric mean of the non-zero components of the permeability tensor ($k_{xx}, k_{yy}, k_{zz}, k_{xy}$) obtained through grid rotation. The maximum geometric mean is obtained when the dominant fracture set is oriented at 45° to the grid walls or principal (i and j directions). The geometric mean falls to a minimum when the dominant fracture set is oriented parallel to the grid walls. Streamline simulations (e.g. Muskat and Wyckoff 1934; Batycky et al. 1997; King and Datta-Gupta 1998) illustrate that flow direction is approximately aligned with the fracture permeability tensor normalized eigenvectors which also vary with respect to grid orientation.

Methodology

Oda (1985) showed that the equivalent fracture permeability tensor for a fractured medium can be calculated as:

$$k_{ij} = \lambda\left(F_{kk}\,\delta_{ij} - F_{ij}\right) \tag{1}$$

where λ is a dimensionless constant with the restriction $0 < \lambda \leq \frac{1}{12}$ and F_{ij} is the fracture tensor as:

$$F_{ij} = \frac{\pi \rho}{4} \int_0^\infty \int_0^\infty \int_\Omega r^2 t^3 n_i n_j E(n, r, t) d\Omega \, \mathrm{dt} \, \mathrm{dr} \tag{2}$$

F_{kk} , the trace of F_{ij} matrix (i.e. sum of diagonal terms of fracture tensor) as:

$$F_{kk} = F_{11} + F_{22} + F_{33} \tag{3}$$

Dershowitz et al. (2000) developed an empirical estimate of the fracture tensor F_{ij}, which consisted of the weighted sum of fracture area and transmissivity as:

$$F_{ij} = \frac{1}{V} \sum_{k=1}^{N} A_k T_k n_{ik} n_{jk} \tag{4}$$

where T_k, the transmissivity of kth fracture with an aperture of e_k is:

$$T_k = \frac{{e_k}^3}{12} \tag{5}$$

V is the grid block volume, A is the fracture area, n_{ik}, n_{jk} are components of the unit normal vector of the kth fracture. Equation 4 contains a projection of the flow volume into desired Cartesian system. Then, the permeability tensor can be calculated by Equation 1. Oda's approach does not account for fractures connectivity (Dershowitz 2000).

The geometric mean of the non-zero components of Oda's permeability tensor is algebraically derived (see Appendix A). Subsequently, the grid rotation angles for which the geometric mean is a maximum and minimum are calculated. For simplicity, we refer to geometric mean of non-zero components of Oda's permeability tensor $(k_{xx}, k_{yy}, k_{zz}, k_{xy})$ as K_G.

A grid block is rotated counter-clockwise in *XY* plane around its center (Figure 3-1). As the grid rotates, the total grid-bounded fracture area, and flow capacity vary. Moreover, the unit normal vector is projected in different i and j directions. The original bounded length of the fracture within the cell is *AB* while it is *CD* after (in this example) a 30° counter-clockwise rotation. The fracture normal n, originally projected as n_i and n_j, become n'_i and n'_j after rotation (Figure 3- 1).

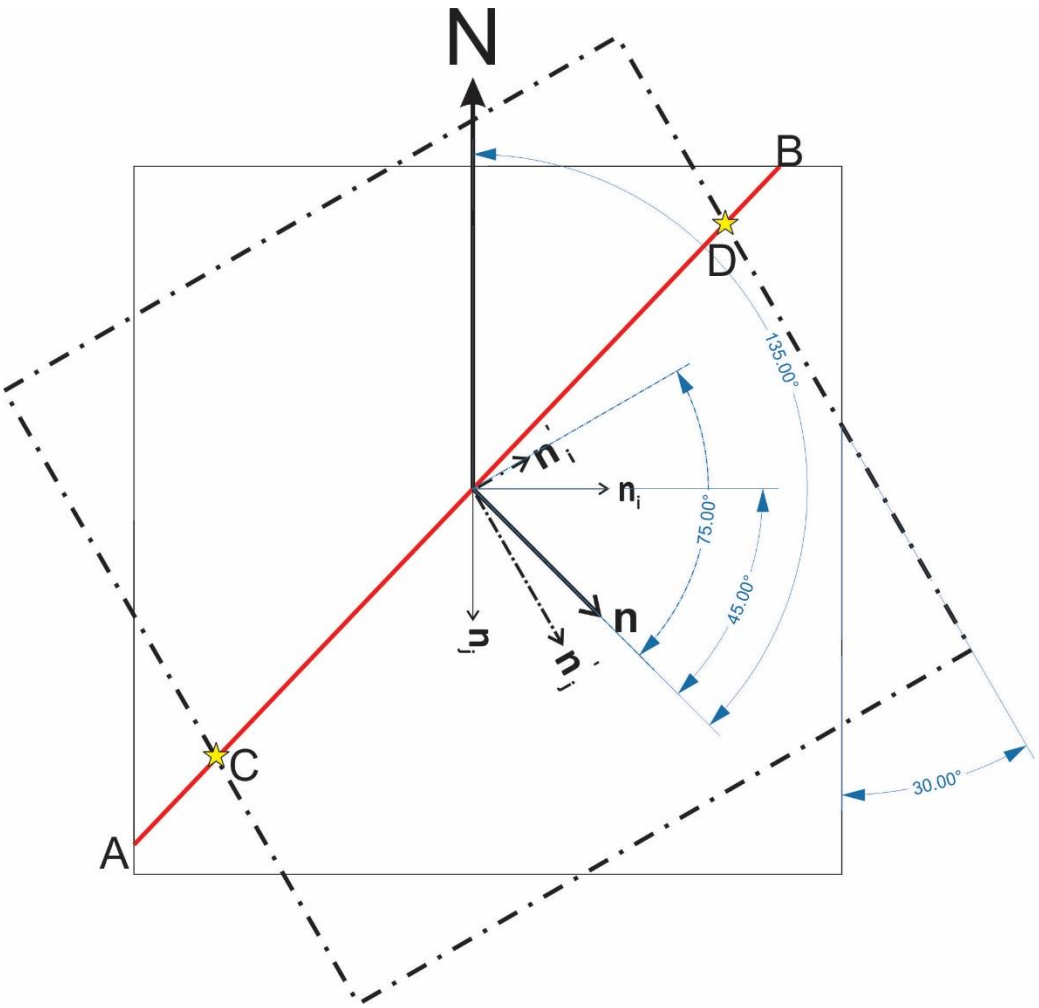

Figure 3-1: A grid block (dashed line) is rotated 30° counter-clockwise around its center. The initial fracture length is AB and has the unit normal vector projections of n_i and n_j on the initial grid block coordinate system. After 30° rotation, the length decreases to CD and has normal vector projections of n'_i and n'_j on the rotated coordinate system.

The variations of the normal vector projection and bounded fracture length introduced by rotation change the component of the permeability tensor and K_G in Oda's method. A computer code

developed in this study calculates the permeability tensor for a given grid cell rotation. Note that fracture configuration after a 90^o rotation is equivalent to the original 0^o configuration; a 105^o rotation, to 15^o, and so on, so that cases associated with 360^o of rotation are covered by these 6 rotations from 0^o to 75^o. In this study, fractures orientation are defined by three terms: the pole coordinates of the fracture center, the fracture trend defined clockwise angle that the fracture surface normal makes relative to north, and the plunge or the angle between the fracture normal and the XY plane.

The variation of K_G with grid rotation angle is documented for the single block, and multi-layer full grid cases. The K_G optimization problem is solved by assuming sets of randomely oriented vertical fractures (with plunge equal 0°) with a constant aperture of 0.00005033ft (0.0153 mm) and an intrinsic permeability of 19870 md (refer to Appendix A) for all the fractures within a grid block volume of 1ft^3 (0.028 m^3). It should be noted that $\lambda = 1/12$ is included in intrinsic permeability calculations. Therefore, using Equation 4 the permeability calculations for N randomly distributed vertical fractures (plunge equal to 0) with trends of $(\theta)_i$ within a grid block can be simplified as:

$$F_{ij} = \sum_{k=1}^{N} A_k n_{ik} n_{jk} \tag{5}$$

Where factor $(\frac{1}{V})$ in Equation 4 is equal to 1. The geometric mean of the non-zero components in the permeability tensor is:

$$K_G = \sqrt[4]{k_{xx} k_{yy} k_{xy} k_{zz}}$$

$$= \sqrt[4]{\sum_{i=1}^{N} A_i Cos^2(\theta)_i \times \sum_{i=1}^{N} A_i Sin^2(\theta)_i \times \sum_{i=1}^{N} A_i Sin(\theta)_i Cos(\theta)_i \times \sum_{i=1}^{N} A_i (Sin^2(\theta)_i + Cos^2(\theta)_i)} \tag{6}$$

The derivation of Equation 6 is presented in Appendix A.

Assuming that fracture area bounded by cell faces does not vary by grid rotation, Equation 6 is maximum when:

$$|Cos(\theta)_i| = |Sin(\theta)_i| \quad for\ i = 1,2,3, \dots, N \tag{7}$$

or when:

$$\theta_i = \frac{\pi}{4} + \frac{n\pi}{2} \quad for\ n = 0,1,2,3 \dots \tag{8}$$

A fracture normal vector with trend θ relative to north after an α degree counter-clockwise grid rotation is equivalent to a fracture normal with a trend of $\theta + \alpha$ in the unrotated system. We showed that K_G is maximum when θ satisfies Equation 8. Thus, maximum K_G occures when α is:

$$\alpha = \left(\frac{\pi}{4} + \frac{n\pi}{2}\right) - \theta_i \quad for\ n = 0,1,2,3 \dots \tag{9}$$

in a similar manner, it can be shown that the rotation angle that minimizes K_G is $\alpha - \frac{\pi}{4}$ or β where:

$$\beta = \left(\frac{n\pi}{2}\right) - \theta_i \quad for\ n = 0,1,2,3 \dots \tag{10}$$

In this optimization problem, all the fractures are considered to have negligble variations of bounded area with grid rotation ($i.e.\ \frac{\partial A_i}{\partial \theta_i} \approx 0$), but in actuality, grid rotation affects the bounded fracture area and shifts α and β by a couple of degrees depending on grid orientation, grid size and fracture pole position (especially when the fracture pole is close to the corner of the grid block). The algorithm developed in this study accounts for fracture area variations with grid rotation and shows that Equation 9 and 10 are acceptable estimates of the optimum values of α and β.

Results and Discussion

Single Block Permeability Tensor. We showed that grid rotation affects the Oda permeability tensor. In the following, we extend the evaluation of grid rotation on the Oda permeability tensor using randomely generated fractures . We generate 120 fractures consisting of three intersecting fracture sets (Table 3-1) in a 10ft by 10ft grid block with intensities and orientations similar to those interpreted in the Tensleep Formation at Teapot Dome, Wyoming, USA. The dominant fracture set strikes at N76°W (trend of 14° relative to north) and the other two sets strike at N28°W and N75° (trends of 62° and 165° respectively) (Figure 3-2).

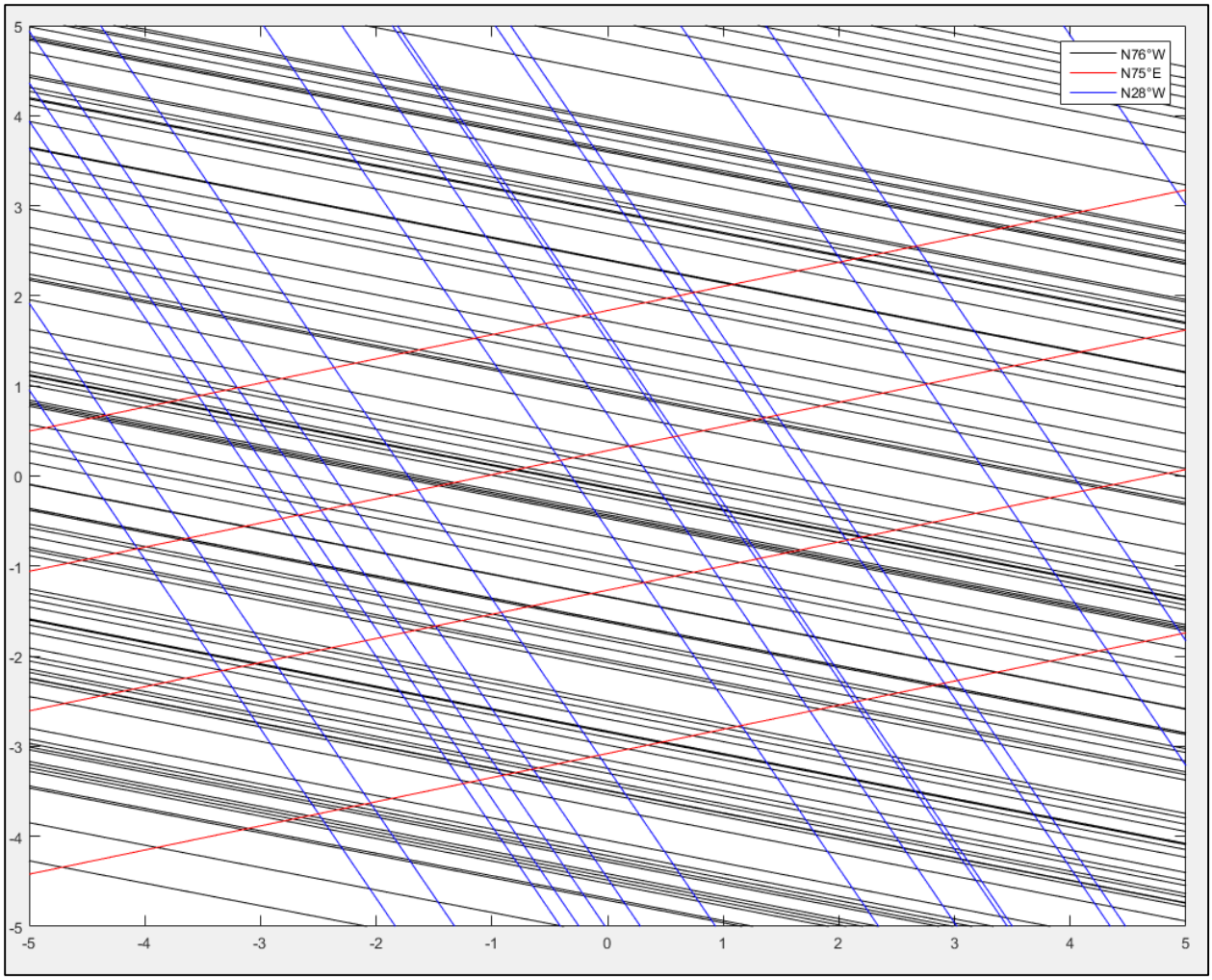

Figure 3-2: Three sets of randomly distributed fractures (total of 120 fractures) are plotted in a 10ft. by 10 ft. grid block.

Table 3-1: Three fracture sets. Set 1 is the dominant fracture set.

	Trend	**Strike**	**Aperture(ft)**	**plunge**	**No. of fractures**
Set 1	14°	N76°W	0.002	0	100
Set 2	62°	N28°W	0.002	0	16
Set 3	165°	N75°E	0.002	0	4

All fracture sets intersect cell faces. Computation of K_G (Figure 3-3) shows that K_G varies periodically with a period of 90° such that:

$$K_G(\theta) = K_G\left(\theta + \frac{\pi}{2}\right)$$

According to the Equation 9, the maximum value of K_G for a single set of fractures occurs at an α of:

$$\alpha = \left(\frac{\pi}{4} + \frac{n\pi}{2}\right) - \theta_i \quad \text{for n} = 0,1,2,3 \ldots$$

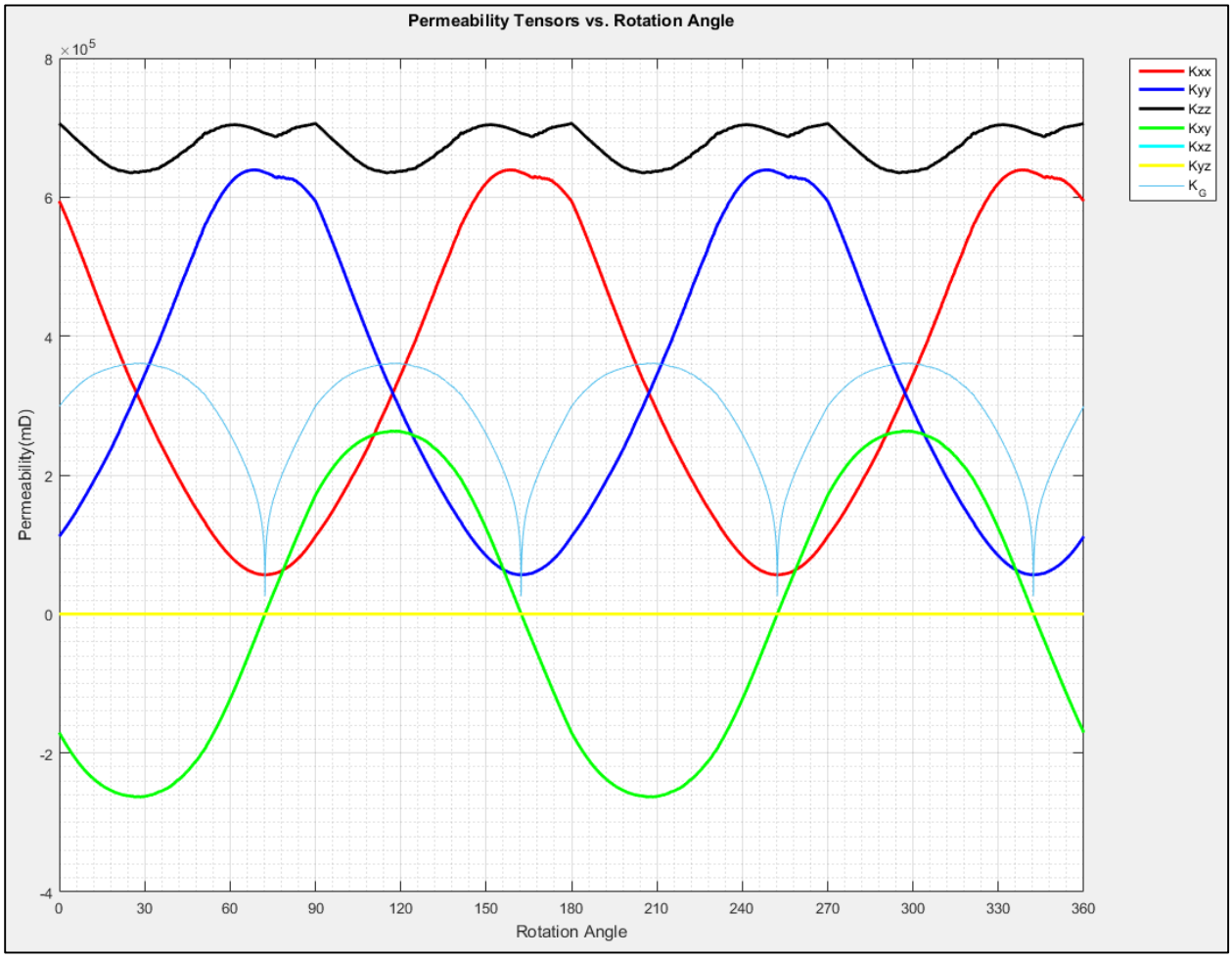

Figure 3-3: Variations of the permeability tensor versus grid rotation for fractures shown in Figure 3-2. The geometric mean of the non-zero components in the permeability tensor $(k_{xx}, k_{yy}, k_{zz}, k_{xy})$ varies approximately $2.5 \times 10^5 mD$ in response to the grid block rotation with a 90°period. Note that k_{xx} and k_{yy} swap values every 90°.

Considering that set 1, the one with 14° trend, is the dominant fracture set in the grid block, the rotation angle α that orients this set along the grid diagonal and maximizes K_G is:

$\alpha = (45° - 14°) + n(90°) = 31°$ for $n = 0,1,2,3 \ldots$

and the angle that reduces K_G to a minimum (i.e. rotates the dominant set into an orientation parallel to the faces of the cell) is:

$\beta = n(90°) - 14° = 76°$ for $n = 0,1,2,3 \ldots$

The results obtained from the computer model agree with those obtained for the simpler analytic solutions (Figure 3-3). The maximum and minimum value of K_G from the computer model occurs at 30° and 73°, respectively and are close to analytic solutions of α and β.

Synthetic model Permeability Tensor. To show the effects of the grid orientation on the fluid flow simulation, a five-layer synthetic model with 13 wells is generated with three sets of fractures common to all layers similar to those described earlier for the Tensleep Formation (Figure 3-4).

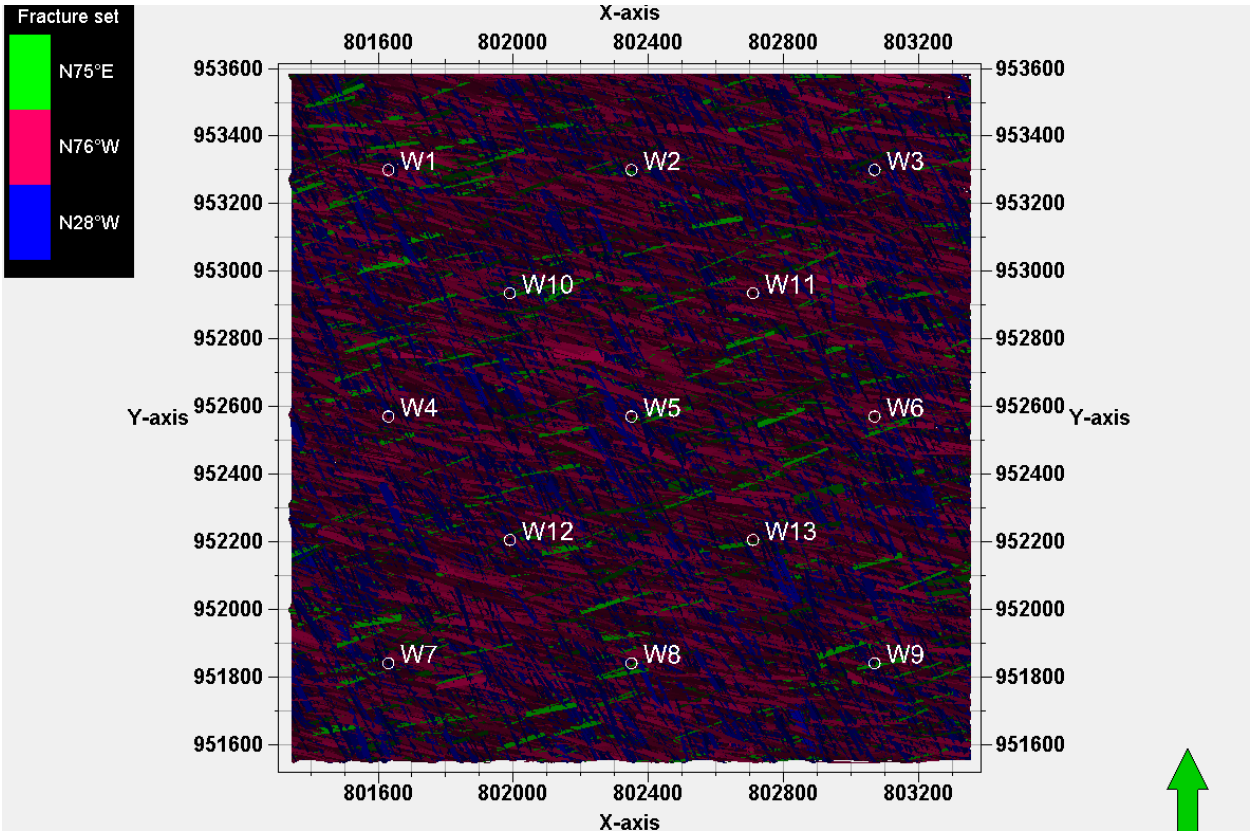

Figure 3-4: Three sets of intersecting fractures are shown. The dominant fracture set strikes N76°W.

The fractures are confined to two zones whithin the model. The reservoir pressure is 2350 psi at a depth of -250 ft subsea similar to the reservoir pressure in the Tensleep Formation at Teapot Dome, Wyoming with a surface elevation of 5200ft (Figure 3-5).

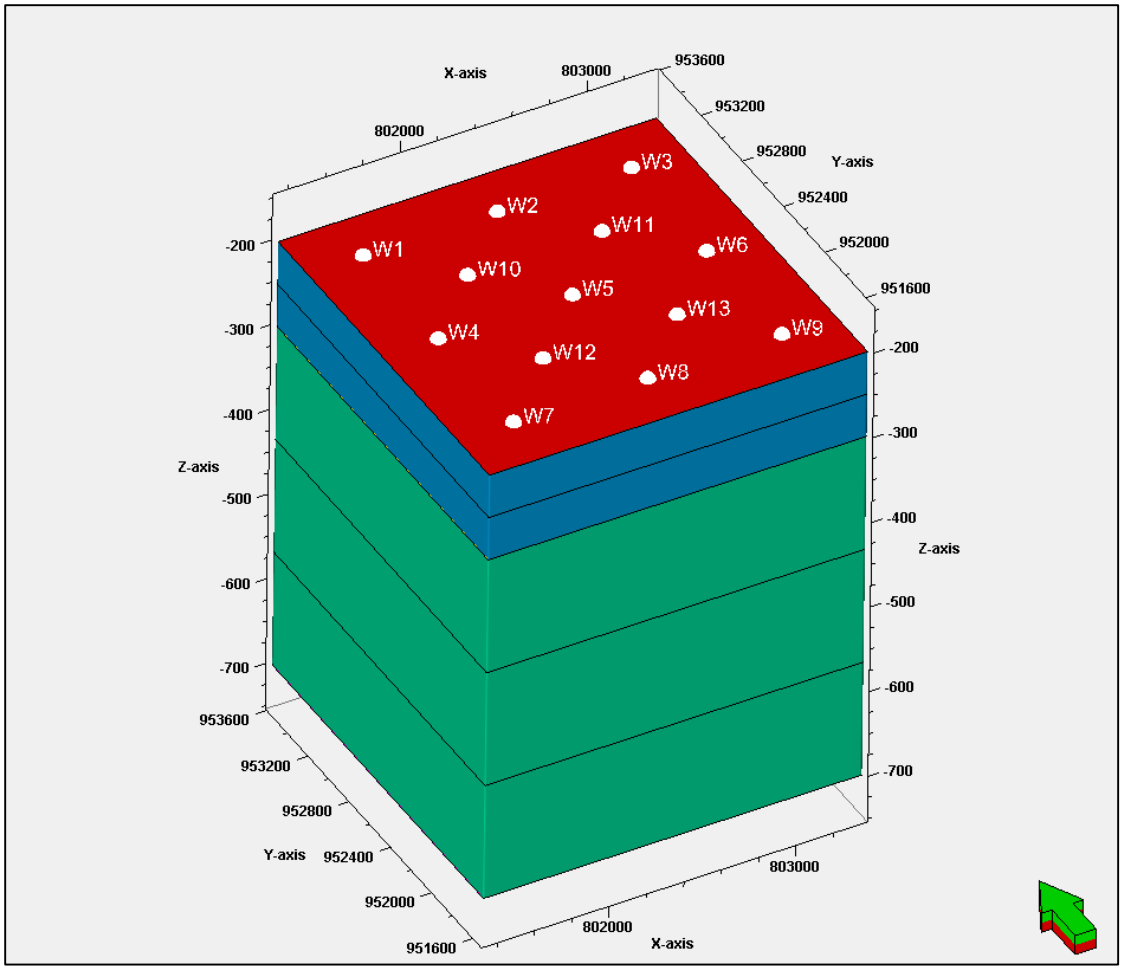

Figure 3-5: This view of the model with 13 wells perforated from -200ft to -700ft. The reservoir fluid is single phase (water).

The model matrix has a isotropic horizontal permeability of 100 md and porosity of 25% with vertical permeability of 5 md. The model is 2000ft on a side in XY plane and extends from -200ft to -700ft subsea. Grid cells whithin the model are 10ft on a side in the XY plane but have variable thickness in the Z direction. In this simulation, the reservoir is gridded in 15° increament in a counter-clockwise direction from 0° to 75°. A portion of the 10ft by 10ft grid around *W10* well is illustrated in Figure 3-6.

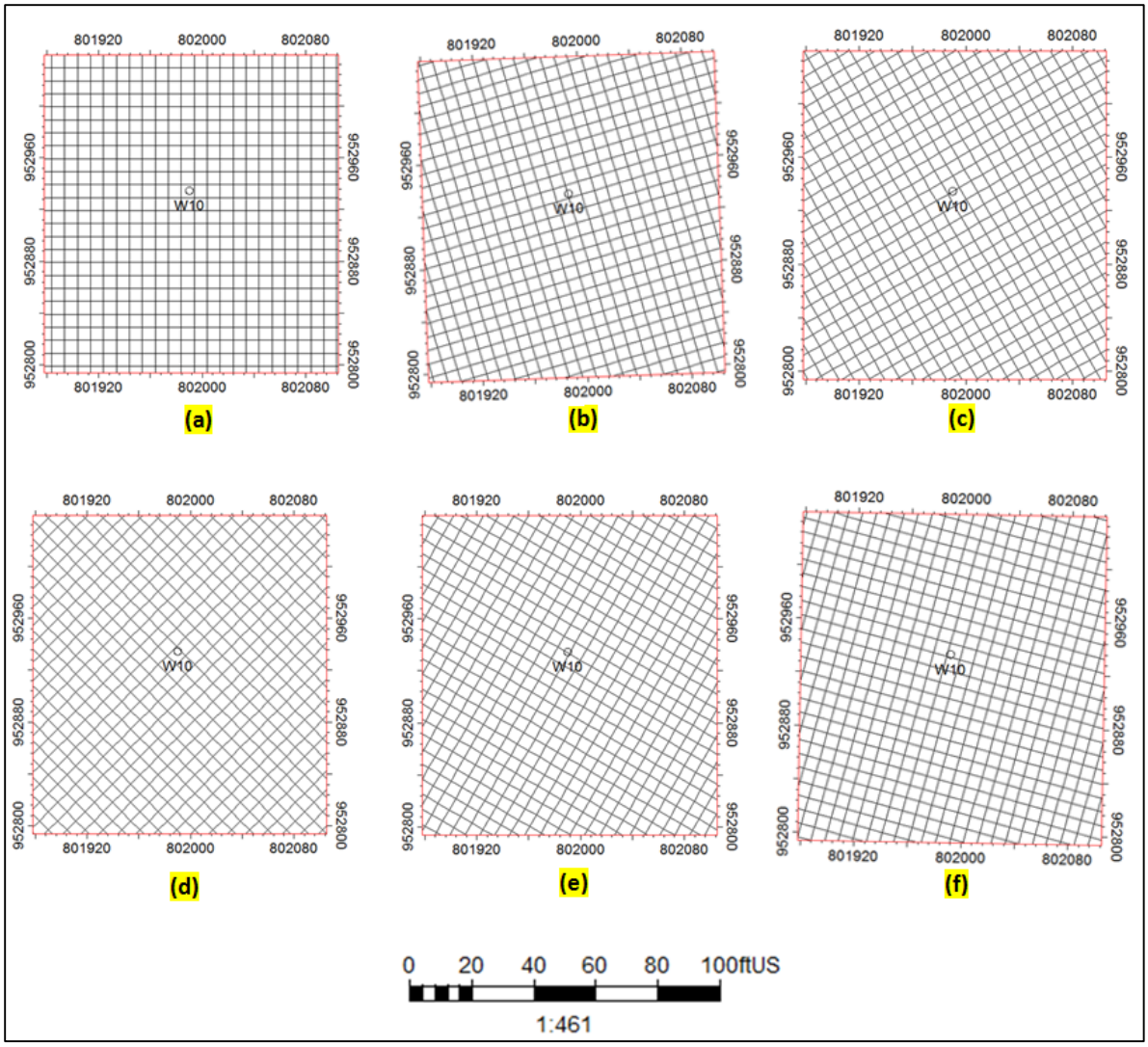

Figure 3-6: a) Grid blocks in the initial configuration have sides oriented north-south and east-west. The gridding is performed in 15° steps counter-clockwise b) 15° c) 30° d) 45° e) 60° f) 75°.

The Oda algorithm is used to upscale the permeability for three fracture sets in the gridded models. The upscaled matrix and fracture properties are exported into a dual porosity simulator to predict water production for a ten year period. The average K_G is calculated for the rotated grid and plotted along with the simulated cumulative water volume production versus the grid rotation angle (Figure 3-7). Minimum K_G occurs when the grid is oriented 75° and the dominant fracture set (N76°W) is roughly parallel to the grid walls. Our study shows that simulated water volume

production varies as K_G with rotation (Figure 3-7). The result is consistent with that obtained for the single block (Figure 3-3): i.e., maximum K_G occurs at 30° and the minimum, at 73°.

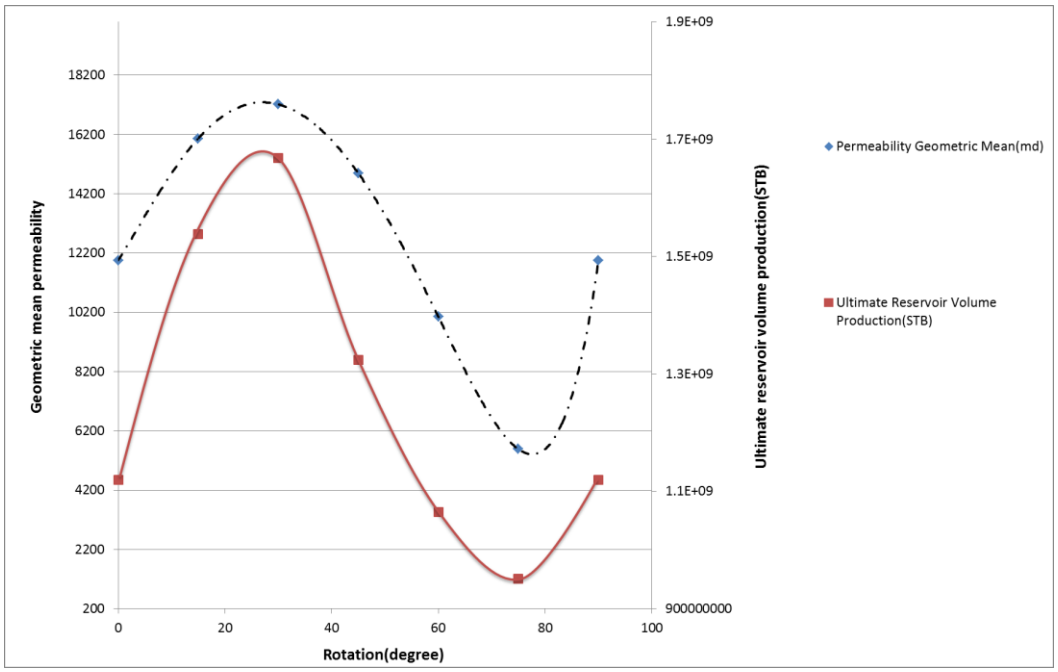

Figure 3-7: Average geometric mean of the gridded models and cumulative water production versus grid orientation.

We simulated the water production in a dual porosity simulator for the rotated grids while keeping all the matrix, fluid properties, and fracture parameters constant. The results show that variations of water production follow variations in K_G. Maximum water production occurs for water production of 30° and the minimum, at 75° (Figure 3-8).

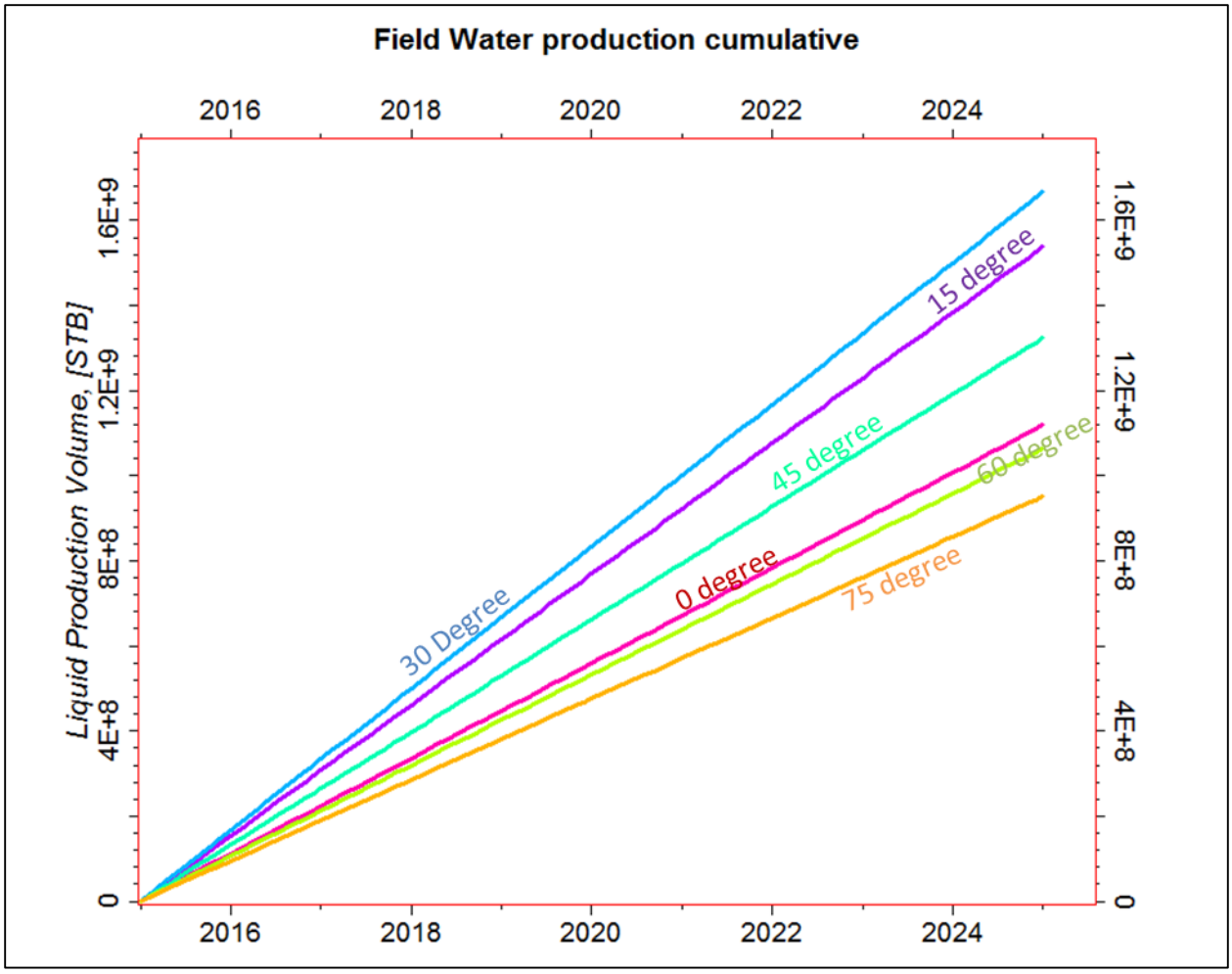

Figure 3-8: The cumulative field water production from 2015 to 2025 for six differently oriented grids. Maximum production occurs at 30° and the minimum, at 75°.

We also undertook streamline simulation (Muskat and Wyckoff 1934; Batycky et al. 1997; King and Datta-Gupta 1998) to model the flow path distribution for each grid orientation. A streamline is defined as flow direction. It is a vector that varies from point-to-point with velocity along the flow path. The advantage of streamline simulation is that fluid movement through the model from timestep $\boldsymbol{t}$ *to* $\boldsymbol{t + \Delta t}$ is portrayed with streamlines rather than cell face to cell face, as in the case for conventional finite difference simulators (Thiele et al. 2010). Streamline geometry is directly related to the distributions of static petrophysical properties distribution (e.g., fracture permeability, porosity, and matrix permeability) (Thiele et al. 2010). The streamline analysis

illustrates that grid orientation affects the flow directions through the model toward the well. For a grid orientation of 75°, the grid is nearly aligned with the dominant fracture set which strikes at N76°W (Figure 3- 9). The majority of the streamlines are nearly parallel the dominant fracture set. However, the other two lower intensity fracture sets also affect the permeability tensors and hence the streamlines. This finding can also be observed from the single block case where at 73°, k_{xx} goes to minimum and k_{yy} goes to its maximum. When the grid is oriented 30° counter-clockwise in the single block case (Figure 3-3) both k_{xx} and k_{yy} get closer to each other so that flow is aligned with grid axes. The k_{xy} lead to flow in oblique directions toward the well.

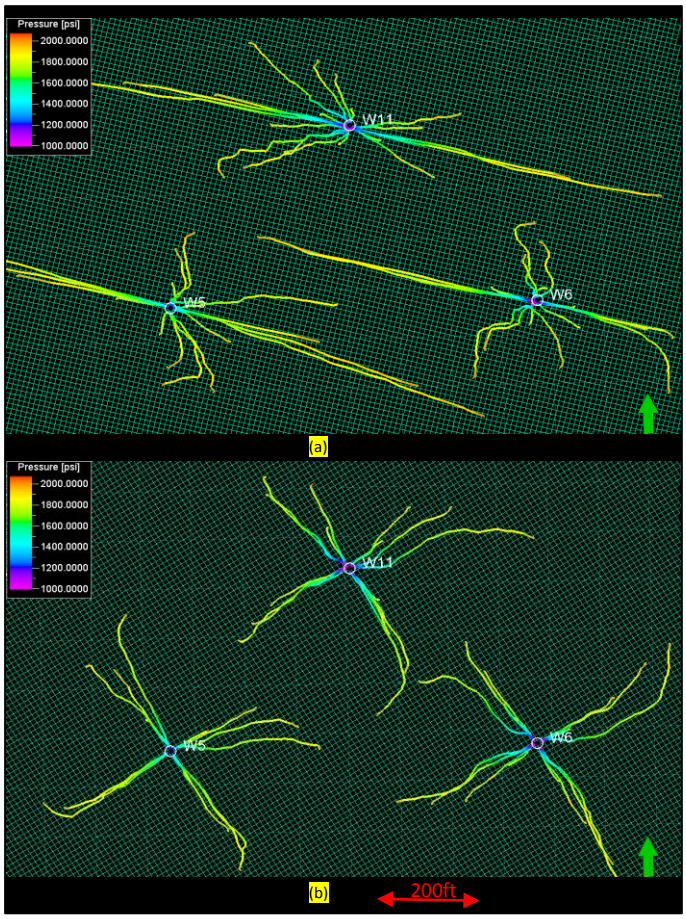

Figure 3-9: The streamline results, color-scaled to reservoir pressure after 10 years of water production for the three wells in a) Grid with a 75° orientation. Most of the streamlines are aligned in N75°W which is close to strike of dominant fracture set (N76°W). b) The streamlines when the grid is oriented at 30°. The grid size is 10ft by 10ft.

The flow directions follow the eigenvectors of the fracture permeability tensor through cells around the well. The length of the eigenvectors corresponds to the eigenvalues of the fracture permeability tensor. The maximum eigenvalue is in *z* direction since the fractures in the models are all vertical. In Figure 3-10A, the grid is oriented at 75° and the eigenvectors are aligned with the grid walls. Smaller eigenvectors are approximately perpendicular to the dominant N76°W fracture set. The other two fracture sets produce non-zero eigenvectors orthogonal to the dominant set and facilitate the flow in that direction. Much of the flow from streamline simulation is aligned with the greater eigenvector which is parallel to the dominant fracture set (Figure 3-10A). When the grid is rotated 30° (Figure 3-10B), the eigenvectors have equal length in the *i* and *j* directions. In this case, the other two sets contribute more to the flow toward the well.

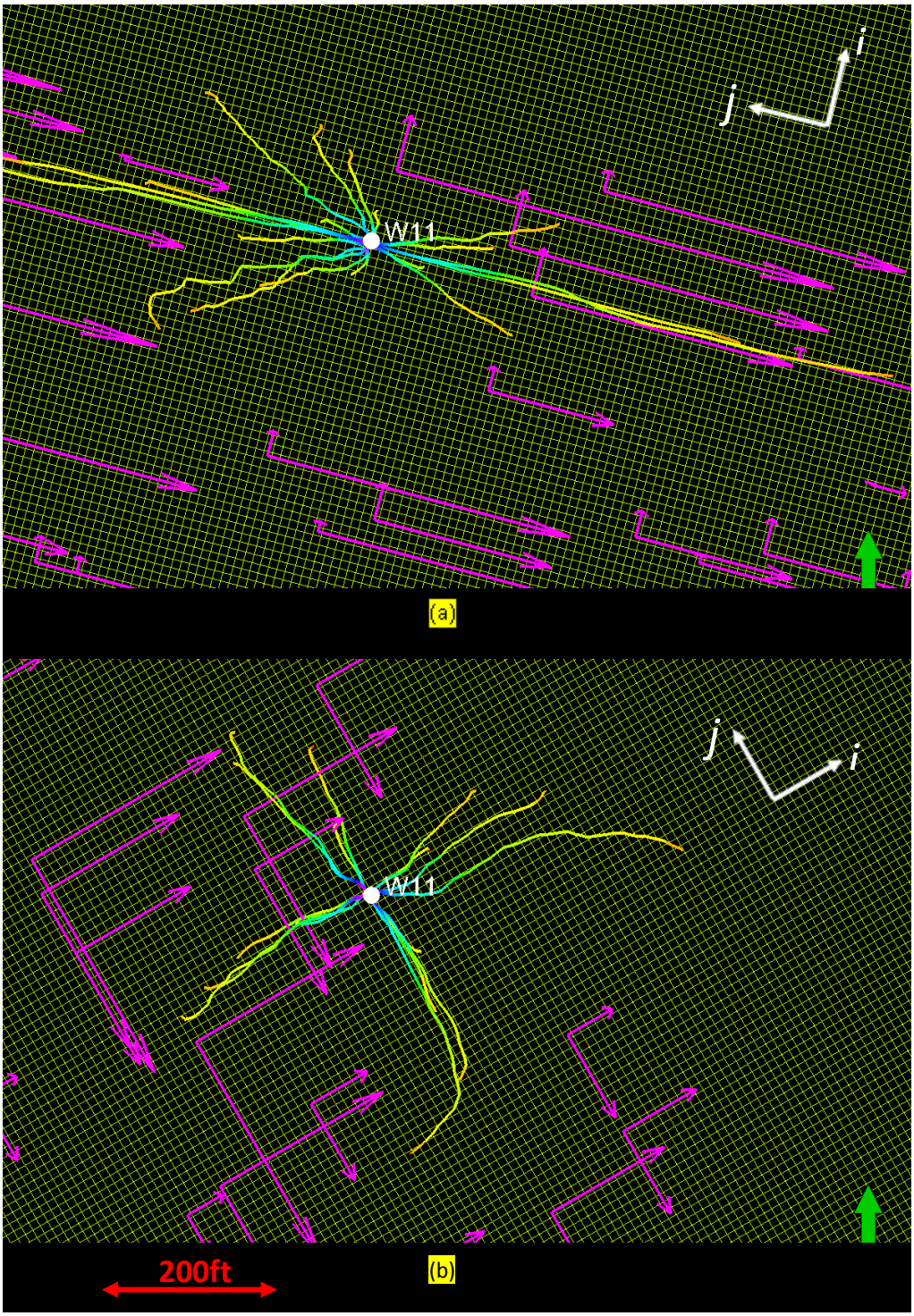

Figure 3-10: Streamlines are shown for well W11 along with eigenvectors (red arrows) with lengths proportional to the eigenvalues for some cells around the well. Eigenvectors vary with the grid orientation. a) The grid is oriented at 75°. The eigenvectors in the j direction (nearly parallel dominant fracture set) are larger than the eigenvectors in i direction. b) The grid is oriented 30° degree relative to north. The eigenvalues and eigenvectors are approximately equal in the i and j direction. The streamlines are nearly orthogonal and parallel to the eigenvector trends.

Conclusions

- Grid block orientation relative to the DFN influences the Oda upscaled permeability tensors and hence the fluid simulation results.
- When grid walls are oriented parallel and perpendicular to the dominant fracture set, the geometric mean of the Oda permeability tensor components (K_G) drops to a minimum as does the simulated cumulative production.
- Any grid rotation angle which brings the dominant fractures to a 45° angle diagonally through the grid block local principal directions (i, j) maximizes K_G and simulated cumulative production.
- The eigenvector analysis and streamline simulations reveal multiple flow directions through a DFN dominated by a single set.
- The results reveal that arbitrarily oriented grids, such as a north-south or inline-crossline grid orientation will lead to non-unique permeability tensor components, cumulative production, and streamlines distribution. Well test data along with the injection tests could shed some light on flow direction and orientation of fracture permeability tensor components and hence optimum grid orientation.

Acknowledgments

The Author would like to thank Dr. Paul Lapointe from Golder Associates Inc. for helpful discussions and comments. This research was not possible without the supports and insightful comments from Dr.Thomas Wilson in the Geology department at West Virginia University.

Nomenclature

α The rotation angle which maximize the permeability geometric mean, deg.

β The rotation angle which minimize the permeability geometric mean, deg.

δ_{ij} The Kronecker delta.

θ Trend, the angle between fracture unit normal and north in clockwise, deg.

μ Kinematic viscosity, [M/LT], cp.

ρ Volume density of fractures, [L^{-3}], ft^{-3}.

λ Dimensionless material-dependent constant.

Ω Solid angle corresponding to the surface of a unit sphere, deg.

A_k Fracture area, [L^2], ft^2.

$E(n,r,t)$ The probability density function that describes fractures with unit normals oriented inside a small solid angle $d\Omega$

F_{ij} The fracture tensor, [L^2], mD.

F_{kk} The trace of the fracture tensor matrix, [L^2], mD.

k_{ij} The permeability tensor, [L^2], mD.

K The intrinsic permeability, [L^2], mD.

K_G The geometric mean of the non-zero components in permeability tensor.

n Unit normal vector of fracture surface.

n_j, n_i The components of fracture unit normal vector.

n_{ik} , n_{jk} The components of the unit normal vector on k^{th} fracture.

V Grid block volume, [L^3], ft^3.

Subscripts

i, j, k Arbitrary orthogonal coordinate system components

G geometric mean of

REFERENCES

Baca, RG, RC Arnett, DW Langford. 1984. Modelling fluid flow in fractured-porous rock masses by finite-element techniques. *International Journal for Numerical Methods in Fluids* **4** (4): 337-348.

Barenblatt, GI, Iu P Zheltov, IN Kochina. 1960. Basic concepts in the theory of seepage of homogeneous liquids in fissured rocks [strata]. *Journal of applied mathematics and mechanics* **24** (5): 1286-1303.

Batycky, RP, Martin J Blunt, Marco R Thiele. 1997. A 3D field-sc ale streamline-based reservoir simulator. *SPE Reservoir Engineering* **12** (04): 246-254.

Clemo, Tom, Leslie Smith. 1997. A hierarchical model for solute transport in fractured media. *Water Resources Research* **33** (8): 1763-1783.

Cooper, SP. 2000. Deformation within a basement-cored anticline Teapot Dome, *Wyoming. [MS thesis]: New Mexico Institute of Mining and Technology* **274**.

Dershowitz, Bill, Paul LaPointe, Thorsten Eiben et al. 2000. Integration of Discrete Feature Network Methods With Conventional Simulator Approaches. *SPE Reservoir Evaluation & Engineering* **3** (02): 165-170.

Dershowitz, William Simon. 1984. Rock joint systems. Massachusetts Institute of Technology.

Gong, Bin, Mohammad Karimi-Fard, Louis J Durlofsky. 2008. Upscaling discrete fracture characterizations to dual-porosity, dual-permeability models for efficient simulation of flow with strong gravitational effects. *SPE Journal* **13** (01): 58-67.

Gupta, A, G Penuela, R Avila. 2001. An integrated approach to the determination of permeability tensors for naturally fractured reservoirs. *Journal of Canadian Petroleum Technology* **40** (12).

Juanes, Ruben, Javier Samper, Jorge Molinero. 2002. A general and efficient formulation of fractures and boundary conditions in the finite element method. *International Journal for Numerical Methods in Engineering* **54** (12): 1751-1774.

Karimi-Fard, M, LJ Durlofsky, K Aziz. 2004. An Efficient Discrete-Fracture Model Applicable for General-Purpose Reservoir Simulators. *SPE Journal* **9** (02): 227-236.

Karimi-Fard, Mohammad, Abbas Firoozabadi. 2003. Numerical simulation of water injection in fractured media using the discrete-fracture model and the Galerkin method.*SPE Reservoir Evaluation & Engineering* **6** (02): 117-126.

Karimi-Fard, M, B Gong, LJ Durlofsky. 2006. Generation of coarse-scale continuum flow models from detailed fracture characterizations. *Water resources research* **42** (10).

Kavousi Ghahfarokhi, Payam, Thomas H Wilson. 2015. Fracture intensity attribute for the Tensleep reservoir at Teapot Dome, Wyoming, USA. *Interpretation* **3** (3): SZ41-SZ48.

Kazemi, H, LS Merrill Jr, KL Porterfield et al. 1976. Numerical simulation of water-oil flow in naturally fractured reservoirs. *Society of Petroleum Engineers Journal* **16** (06): 317-326.

King, Michael J, Akhil Datta-Gupta. 1998. Streamline simulation: A current perspective. *In Situ* **22** (1): 91-140.

Li, Junchao, Zhengdong Lei, Guan Qin et al. 2015. Effective Local-Global Upscaling of Fractured Reservoirs under Discrete Fractured Discretization. *Energies* **8** (9): 10178-10197.

Long, Jane, Peggy Gilmour, Paul A Witherspoon. 1985. A Model for Steady Fluid Flow in Random Three-Dimensional Networks of Disc-Shaped Fractures. *Water Resources Research* **21** (8): 1105-1115.

Muskat, M, RDt Wyckoff. 1934. A theoretical analysis of water-flooding networks.*Transactions of the AIME* **107** (01): 62-76.

Narr, Wayne, David W Schechter, Laird B Thompson. 2006. *Naturally fractured reservoir characterization*, Richardson, TX: Society of Petroleum Engineers (Reprint).
Oda, Mc. 1985. Permeability tensor for discontinuous rock masses. *Geotechnique* **35** (4): 483-495.
Penuela, G, F Civan, RG Hughes et al. 2002. Time-dependent shape factors for interporosity flow in naturally fractured gas-condensate reservoirs.Paper SPE 75234 presented at SPE/DOE improved Oil Recovery Symposium,Tulsa,13-17 April.
Sarda, S, L Jeannin, R Basquet et al. 2002. Hydraulic Characterization of Fractured Reservoirs: Simulation on Discrete Fracture Models. *SPE Reservoir Evaluation & Engineering* **5** (02): 154-162.
Sarma, Pallav, Khalid Aziz. 2006. New Transfer Functions for Simulation of Naturally Fractured Reservoirs with Dual Porosity Models. *SPE Journal* **11** (03): 328-340.
Sarma, Pallav. 2003. New transfer functions for simulation of naturally fractured reservoirs with dual porosity models, Stanford University.
Thiele, Marco R, RP Batycky, DH Fenwick. 2010. Streamline simulation for modern reservoir-engineering workflows. *Journal of Petroleum Technology* **62** (01): 64-70.
Thomas, L Kent, Thomas N Dixon, Ray G Pierson. 1983. Fractured reservoir simulation. *Society of Petroleum Engineers Journal* **23** (01): 42-54.
van Golf-Racht, Theodor D. 1982. *Fundamentals of fractured reservoir engineering*, Elsevier (Reprint).
Warren, JE, P Jj Root. 1963. The behavior of naturally fractured reservoirs. *Society of Petroleum Engineers Journal* **3** (03): 245-255.
Wilson, Thomas H, Valerie Smith, Alan Brown. 2015. Developing a model discrete fracture network, drilling, and enhanced oil recovery strategy in an unconventional naturally fractured reservoir using integrated field, image log, and three-dimensional seismic data. *AAPG Bulletin* **99** (4): 735-762.

Appendix A

The intrinisic permeability for each fracture can be computed using the cubic law as follows:

$$K = \frac{1}{12}(e^2) \times 9.4131 \times 10^{13} \quad = \frac{1}{12}(0.00005033^2) \times 9.4131 \times 10^{13} \; = \; 19870 \; mD \tag{A-1}$$

Where K is the intrinsic fracture permeability and e is the aperture.

The 3D fracture tensor F_{ij} is a symetric second order tensor that expresses frature flow as a vector along the fracture unit normal as:

$$F = \begin{bmatrix} F_{ii} & F_{ij} & F_{ik} \\ F_{ji} & F_{jj} & F_{jK} \\ F_{ki} & F_{kj} & F_{kk} \end{bmatrix} \tag{A-2}$$

where:

$$F_{ii} = \frac{1}{V}\sum_{k=1}^{n} A_k e_k k_k \sin(Trend_k)\sin(Trend_k) \quad \text{(A-3)}$$

$$F_{ij} = F_{ji} = \frac{1}{V}\sum_{k=1}^{n} A_k e_k k_k \sin(Trend_k)\cos(Trend_k) \quad \text{(A-4)}$$

$$F_{jj} = \frac{1}{V}\sum_{k=1}^{n} A_k e_k k_k \cos(Trend_k)\cos(Trend_k) \quad \text{(A-5)}$$

$$F_{ik} = F_{ki} = \frac{1}{V}\sum_{k=1}^{n} A_k e_k k_k \sin(Trend_k)\sin(Plunge_k) \quad \text{(A-6)}$$

$$F_{jk} = F_{kj} = \frac{1}{V}\sum_{k=1}^{n} A_k e_k k_k \cos(Trend_k)\sin(Plunge_k) \quad \text{(A-7)}$$

$$F_{kk} = \frac{1}{V}\sum_{k=1}^{n} A_k e_k k_k \sin(Plunge_k)\sin(Plunge_k) \quad \text{(A-8)}$$

For the case where $e_k k_k = 1\ ft.mD$ and $V = 1ft^3$ for all fractures, the permeability tensor can be simplified as follows:

$$k_{ij} = \left(F_{kk}\,\delta_{ij} - F_{ij}\right) =$$

$$\begin{bmatrix} \sum_{i=1}^{N} A_i(Sin^2(\theta)_i + Cos^2(\theta)_i) & 0 & 0 \\ 0 & \sum_{i=1}^{N} A_i(Sin^2(\theta)_i + Cos^2(\theta)_i) & 0 \\ 0 & 0 & \sum_{i=1}^{N} A_i(Sin^2(\theta)_i + Cos^2(\theta)_i) \end{bmatrix} -$$

$$\begin{bmatrix} \sum_{i=1}^{N} A_i Sin^2(\theta)_i & \sum_{i=1}^{N} A_i Sin(\theta)_i Cos(\theta)_i & 0 \\ \sum_{i=1}^{N} A_i Sin(\theta)_i Cos(\theta)_i & \sum_{i=1}^{N} A_i Cos^2(\theta)_i & 0 \\ 0 & 0 & 0 \end{bmatrix} =$$

$$\begin{bmatrix} \sum_{i=1}^{N} A_i Cos^2(\theta)_i & -\sum_{i=1}^{N} A_i Sin(\theta)_i Cos(\theta)_i & 0 \\ -\sum_{i=1}^{N} A_i Sin(\theta)_i Cos(\theta)_i & \sum_{i=1}^{N} A_i Sin^2(\theta)_i & 0 \\ 0 & 0 & \sum_{i=1}^{N} A_i(Sin^2(\theta)_i + Cos^2(\theta)_i) \end{bmatrix} \quad \text{(A-9)}$$

SI Metric Conversion Factors	
STB × 1.589873	E−01= m^3
cp × 1.0	E-03=Pa.s
ft × 3.048	E-01= m
mD × 9.869233	E−04= mm^2
psi × 6.894757	E+00= kPa

Chapter 4: CO_2-EOR Analysis

Abstract

The Tensleep Formation at Teapot Dome, Wyoming is a naturally fractured reservoir that has been studied for CO_2-EOR. A realization of fractures is generated using a discrete fracture network (DFN) approach. The model DFN has three fracture sets: a dominant, high intensity N76°W set and two lower-intensity sets that strike N28°W and N75°E. The fracture intensity in the model DFN is extracted from a most negative curvature dissimilarity attribute extracted from the post-stack 3D seismic data. In addition, probable deformation bands are incorporated in the model as permeability barriers parallel to N40°E striking S_1 fault. The generated model DFN is plugged into a dual porosity compositional reservoir simulator and adjusted to obtain a production history match. A three parameter Peng-Robinson equation of state (EOS) is calibrated against the swelling tests laboratory data to obtain accurate phase behavior for CO_2-EOR in the Tensleep reservoir. We undertook a sensitivity analysis on fracture aperture in the model DFN. Our results show that an aperture multiplier of 5 (permeability multiplier of 5^3=125) in the DFN considerably decreases the difference between simulated and field production history. Additional assessments suggest a lower fracture permeability in the vertical direction is needed to obtain the history match. We show that an aperture multiplier of 5 might overestimate K_z and causes significant water-coning and consequently less oil production from the reservoir. The K_z multiplier of 125 is then decreased to 62.5 to counteract water-conning from the aquifer and approximate the oil production history. Subsequently, a streamline simulation is undertaken to evaluate fluid flow patterns in the

history matched model. Results show that the designed permeability barriers (interpreted as possible deformation bands) compartmentalize the reservoir.

The history matching effort is followed by evaluation of two CO_2-EOR models. CO_2 is injected in the B1 Tensleep Sandstone from the end of the production history (December, 2005) for 3 years at an injection rate of 1 MMSCF/day. The first model includes three horizontal injectors parallel to the main fracture set and the second model has three horizontal injection wells perpendicular to the dominant fracture set. Although immediate CO_2 breakthrough is observed in both models, model 1 yields a higher oil recovery and a lower CO_2 mole fraction at the surface. The oil recovery improvement is less than 700 MSTB for both models. Finally we show that ultimate CO_2-EOR recovered oil can vary up to 150 MSTB and depends on how impermeable the permeability barriers are.

Presentation Sequence

This chapter starts with an introduction to fractured reservoir simulation and CO_2-EOR processes and implications. Then the static modeling section covers fracture framework modeling, gridding, and petrophysical modeling. Relative permeabilities and capillary pressure data analysis is presented in the rock physics section. Subsequently, a PVT (pressure, volume, and temperature) section covers the steps needed to develop an equation of state (EOS) for the compositional simulation. The history matching section covers the simulation of the field production history and provides an input for CO_2-EOR simulation. The streamline simulation section includes visualization of streamlines in the history matched model. Thereafter, a CO_2-EOR analysis is presented followed by a conclusions section. Finally, some recommendations are presented that could improve the accuracy of the model.

Introduction

Naturally fractured reservoirs (NFR) are challenging to model because fracture networks are often complex and incorporate fluid transfer from matrix to the fractures. High permeability fractures typically cause major fluid flow in fractures rather than matrix to matrix block. However, they can also act as flow barriers when mineralized or through infilling of fine-grain materials in formerly open fractures. Wireline image logs, outcrop studies, core observations, and seismic data analysis provide direct and indirect measurements of fracture properties at different scales. Observations made at these different scales must be integrated to provide a representative model of the reservoir DFN (Wilson et al. 2015; Kavousi and Wilson, 2015). Fracture spacing, aperture, and length distributions can be incorporated in the reservoir model using wireline image logs, core data, and field studies (Cooper, 2000; Wilson et al. 2015). While uncertainties remain, these models are consistent with observations made at a variety of scales.

Barenblatt et al. (1960) introduced dual porosity (DP) concepts for fluid flow simulation in fractured reservoirs using a transfer function to model the flow between fracture and matrix medium. Warren and Root (1963) used a simplified dual porosity version of Barenblatt et al. (1960) and introduced a dual porosity model to the petroleum industry for single phase flow and Kazemi et al. (1976) extended it to two-phase flow. Thomas et al. (1983) developed the dual porosity model for three-phase flow in fractured reservoirs. The key feature of their model was that flow simulation incorporates coupled flow continua: one for the matrix and the other for the DFN. Fluid flow through the fracture network along with flow from the matrix into the fracture network can be modeled with a transfer function referred to as the shape factor (Kazemi et al. 1976, Penuela et al. 2002, Sarma and Aziz, 2004; Warren and Root, 1963). In recent years Karimi-Fard et al. (2003) used an unstructured control volume finite difference approach with two-point

flux approximation to simulate the flow in 2D and 3D discrete fracture models (DFM). Although DFM approaches provide a more accurate results, they are computationally expensive and unpractical for use in large fields (Li et al. 2015a; Gong et al. 2008). Computational constraints limit the number of fractures in such models to from 10^4 to 10^5 fractures (Dershowitz et al. 2000). In addition, unstructured gridding of a large number of fractures increases the complexity of computations.

Gong et al. (2008) used the DFM and introduced a multiple sub-regions (MSR) approach to resolve the dynamic interactions within the matrix to calculate coarse-scale flow parameters of fracture-fracture, matrix-fracture, and matrix-matrix flow for a dual porosity model. Geometry of the subregions and dynamic parameters are determined by calculating local flow through the discrete fracture model using the approach previously introduced by Karimi-Fard et al. (2003). Gong et al. (2008) extended the MSR approach by introducing gravitational effects on phase segregation.

Dershowitz et al. (2000) used Oda's method (Oda, 1985) in a model DFN to build the permeability tensor field in a dual porosity simulation. This integrated approach is more practical for large fields. Oda (1985) calculated the permeability tensor by introducing the fracture tensor, which expresses fracture flow as a vector along the fracture's unit normal and only depends on the geometry of the fractures (aperture, size and orientation). Oda's approach is commonly available in commercial software as a fast algorithm to calculate fracture permeability tensors. However, this method does not account for fracture network connectivity (Dershowitz et al. 2000). Oda's method is a fast approach to estimate the permeability tensor when the medium is highly fractured (Dershowitz et al. 2000; Gupta et al. 2001).

We use a DFN along with the Oda's method to simulate productions in a fully compositional dual porosity simulator for the Teapot Dome oilfield, Wyoming (Figure 4-1). The matched reservoir model is then used in a compositional simulator to model CO_2-EOR. CO_2-EOR can increase ultimate oil recovery by 7-23% of original oil in place (Jarrell et al. 2002). CO_2-EOR efficiency significantly depends on optimization of the injection process which requires a thorough understanding of reservoir heterogeneities and phase behaviors (Li et al. 2015b). Injected CO_2 usually follows less resistant flow paths such as fractures or high permeability channels to production wells. This effect is intensified by the low viscosity of CO_2 at reservoir conditions. Although optimum well location relative to reservoir heterogeneities increases sweep efficiency, early breakthrough cannot be avoided in most cases, just postponed (Li et al. 2015b). CO_2 and oil have multiple contact miscibility. It is a dynamic fluid-mixing process in which CO_2 initially mixes with the oil and makes it lighter. This process continues by vaporization of oil components into CO_2 rich phase. Exchanges of components continues until no interfaces remain between the CO_2-enriched and oil-enriched CO_2 phases (Jarrell et al. 2002). Although miscibility is a function of reservoir temperature and pressure, only pressure controls the miscibility in isothermal reservoirs (Chiaramonte, 2009).

Minimum miscibility pressure (MMP) refers to a pressure at which miscibility occurs. It can be achieved by injecting CO_2 at a higher pressure than MMP or enriching the gas with intermediate-weight hydrocarbons (Li et al. 2015b). Injected CO_2 displaces oil, develops miscibility, swells oil, and reduces oil viscosity (Chung et al. 1988). CO_2-EOR sweep efficiency can be greatly influenced by well pattern, well type, injection rate, reservoir heterogeneity, phase behavior, mass transfer of components between gas and oil phases, density contrast between phases, MMP, and many other

parameters (Li et al. 2015b; Khorsandi et al. 2014; Araktingi and Orr, 1993; Chung et al. 1988). These complexities make CO_2- EOR difficult to accurately simulate.

Wadleigh (2005) implemented a CO_2-EOR simulation for RMOTC (Rocky Mountain Oil Testing Center) during the planning of CO_2-EOR pilot tests in the Tensleep reservoir at Teapot Dome. He used a Peng-Robinson (1976) equation of state (EOS) and calibrated it against the swelling test data from Hycal (2004). The model has constant porosity and permeability for each layer. Friedmann and Stamp (2006) used this model and predicted 30-40% oil recovery improvement by CO_2-EOR. Gaviria (2005) developed a model with variable fracture permeabilities (20000-40000mD) derived from fracture apertures obtained from CT scans of cores. He showed that a pseudo-miscible black oil fluid model could not represent the CO_2-EOR and sequestration project at Teapot Dome and noted that a fully compositional simulation is necessary. In addition, fully compositional history matching was not achieved due to simulation errors. Chiaramonte (2009) implemented a fully compositional simulation using Wadleigh (2005) EOS along with stochastic petrophysical properties for matrix, with the addition of constant fracture porosity and permeability for each layer. Fracture permeabilities have lower values perpendicular to the main fracture set which strikes at N76°W to account for anisotropy. She observed a CO_2 breakthrough after 16 days when injecting 1 MMSCF/day for 6 weeks in well 44-1-TPX-10 while producing at 56-TPX-10, 43-2-TPX-10, 55-TPX-10, 63-TPX-10, and 75-TPX-10 in vicinity of 44-1-TPX-10 injector well(refer to Figure 4-1 for well locations). A well control strategy including shut in the wells until the pressure rises was applied and yielded a 28% oil recovery improvement within 5 years.

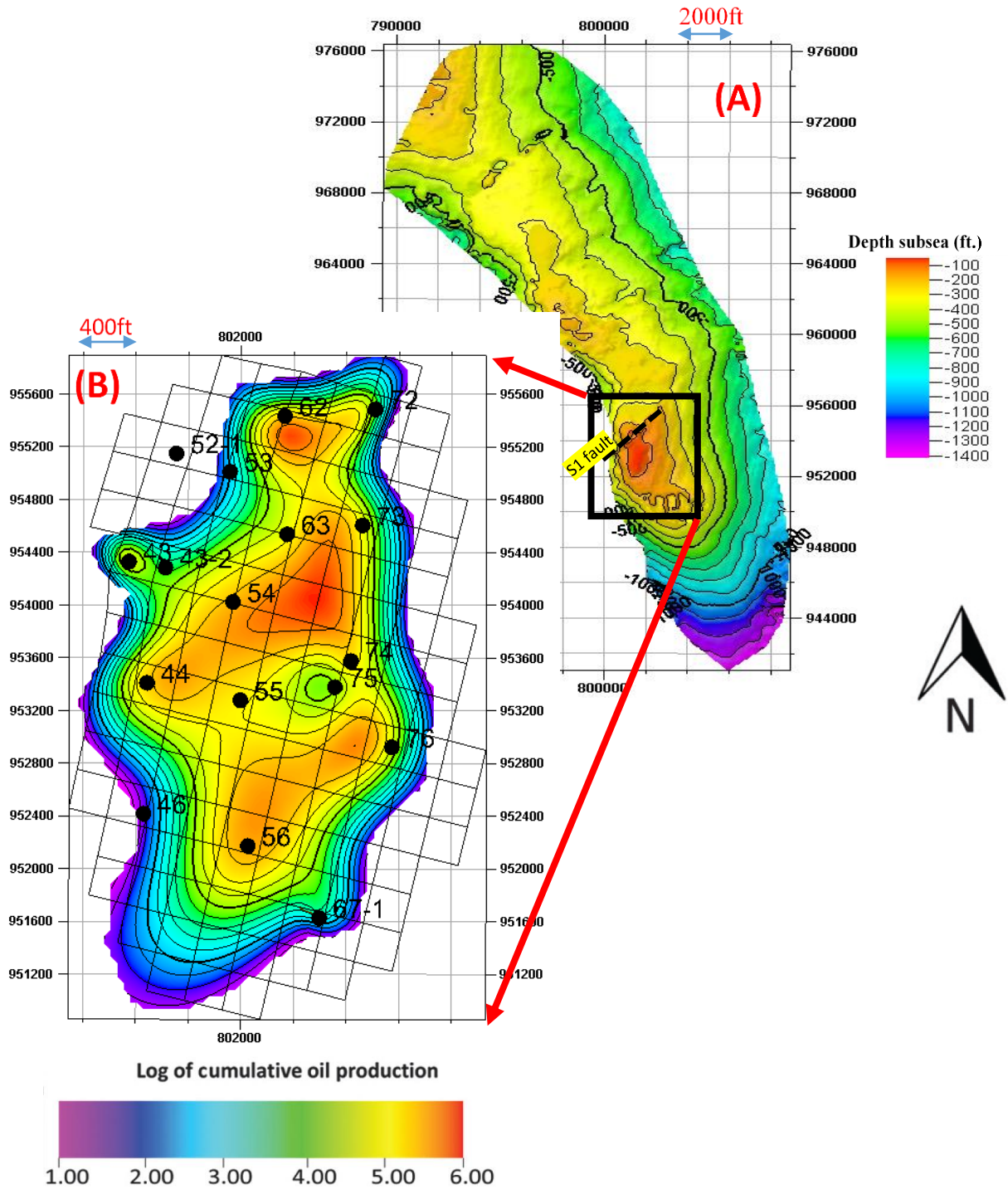

Figure 4-1: A) The Tensleep horizon interpreted from 3D seismic data shown in subsea depth (ft.) B) Contour map of cumulative oil production (bbl) from 1978 to 2004 in Section 10 overlaid by the reservoir grid for flow simulation. The gridding size is 300ft by 300ft and it is approximately oriented parallel to the main fracture set (N76°W). Note that suffix "-TPX-10" is removed from the well names for visualization.

Static Modeling

Fracture Model Framework: A model discrete fracture network (DFN) is generated using the fracture aperture and length distributions proposed by Wilson et al. (2015) and a fracture intensity attribute proposed by Kavousi and Wilson (2015). Wilson et al. (2015) used wireline image logs and statistically showed that fracture apertures are log-normally distributed with the mean log electrical aperture of -1.805 (corresponding to 0.01568mm). Texas and Ferguson (2002) conducted a CT scan of two cores retrieved from well 48-X-28 at depth of 5565ft (Core A) and 5566ft (Core B). They reported open and mineralized fractures (filled with high density minerals such as crystalline dolomite in both cores). The statistical parameter for aperture distribution in Core A and Core B are presented in Table 4-1.

Table 4-2: mean and standard deviation of apertures observed in CT scan of Core A and B from well 48-X-28.

	Mean [mm]	Standard Deviation [mm]
Core A	0.222	0.577
Core B	0.537	0.757

Fracture aperture distribution in cores are not measured under overburden pressure and show larger values than those measured in wireline image logs (Figure 4-2).

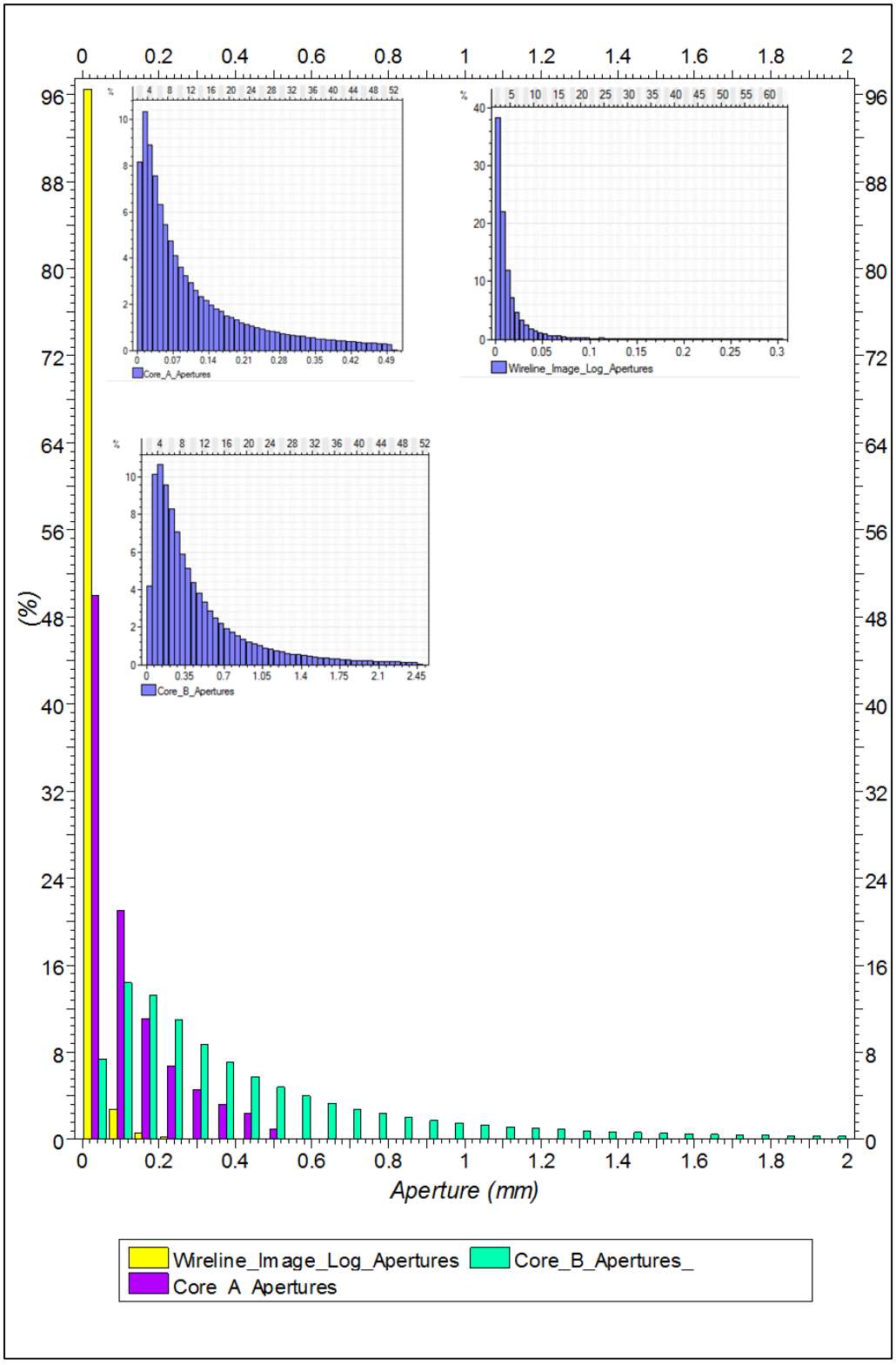

Figure 4-2: Apertures are log-normally distributed in the wireline image logs, Core A, and Core B. Note apertures measured in Core A and Core B are under no overburden pressure. We use the wireline image log aperture distribution for the base case in the history matching.

Wilson et al. (2015) suggested a power-law distribution for fracture length with the majority of the fracture length between 5m (16.4ft) and 15m (49.2ft). In this study we made the following assumptions:

1- All Fractures are vertical in the Tensleep reservoir at Teapot Dome.
2- Fractures in each zone (A Sand, B Dol, B1Sand, B2 Sand, C Dolomite, and Amsden) have heights equal to the zone height.
3- Fractures are parallel plates with constant aperture.
4- Oil production effects on fracture apertures during the production history are assumed to be negligible.

Gridding: Kavousi (2016) showed that upscaling of the fracture permeability tensor using Oda's method (Oda, 1985) is direction dependent and will generate different results for different grid orientations when used in a dual porosity reservoir simulator. There are three fracture sets in the Tensleep Formation at Teapot Dome: a dominant, high intensity N76°W set and two lower-intensity sets that strike N28°W and N75°E. With these three intersecting fracture sets, the permeability tensor varies with gridding orientation (Figure 4-3). As a rule of thumb, off-diagonal terms of permeability tensors should be close to zero to improve the computation speed (Kavousi, 2016). Thus, we used a grid with an orientation of N72°W, roughly parallel to the dominant fracture set in the reservoir. Using this orientation, the off-diagonal permeability terms are approximately equal to zero and can be neglected in flow simulation.

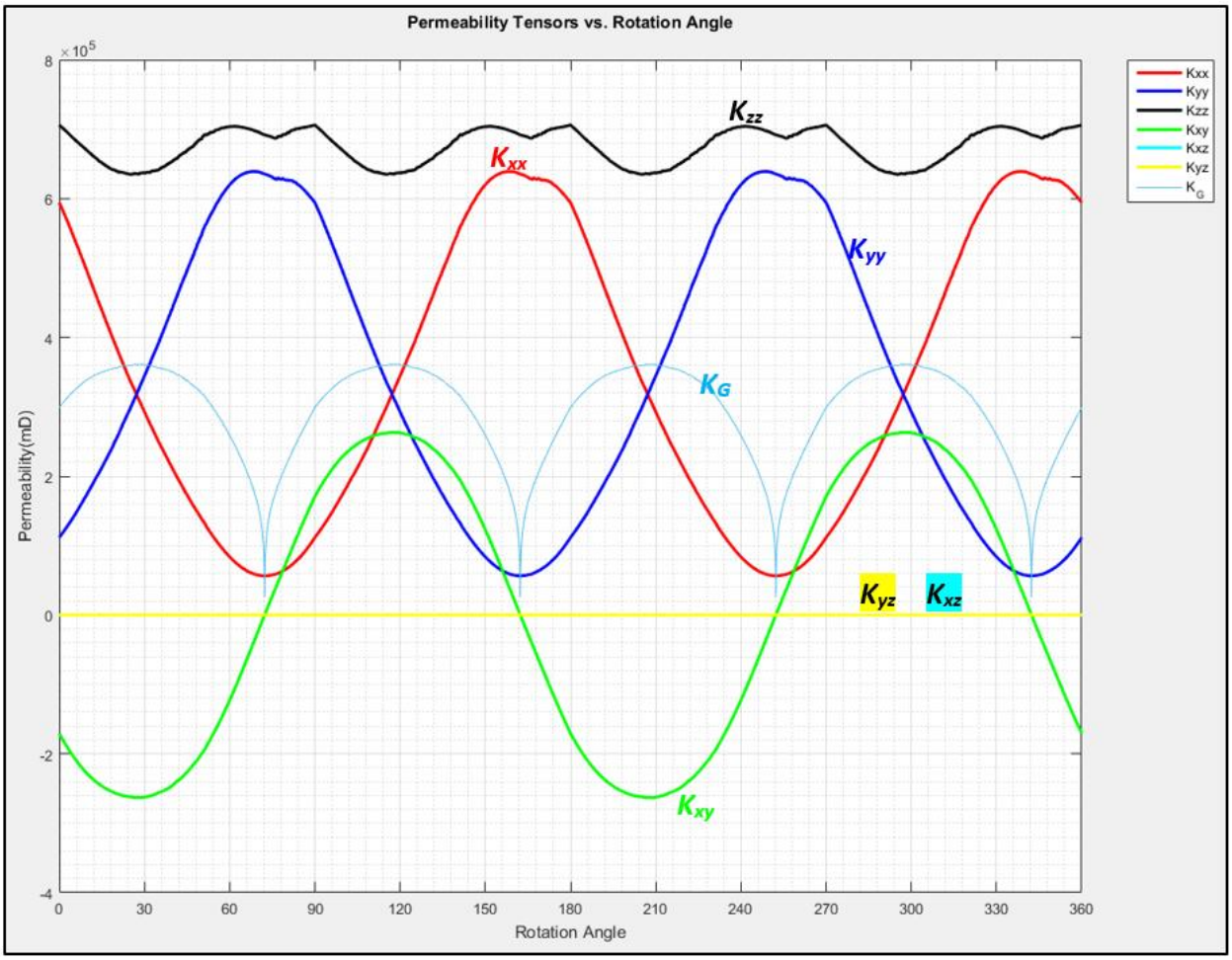

Figure 4-3: the components of the permeability tensor varies with the grid orientation, note that at around 72°, the tensor off-diagonal components are close to zero. Note k_{xz} and k_{yz} are zero since the fractures in the grid are all vertical.

The model used in this study has 300 ft. by 300ft. grid cells as proposed by Chiaramonte (2009) and Gaviria (2006).

Petrophysical Modeling: Chiaramonte (2009) used core data of 8 wells which penetrated Tensleep Formation at Teapot Dome for reservoir petrophysical modeling: 11-AX-11, 43-TPX-10, 44-1-TPX-10, 54-TPX-10, 55-TPX-10, 56-TPX-10, 62-TPX-10, and 71-AX-15 (Figure 4-4).

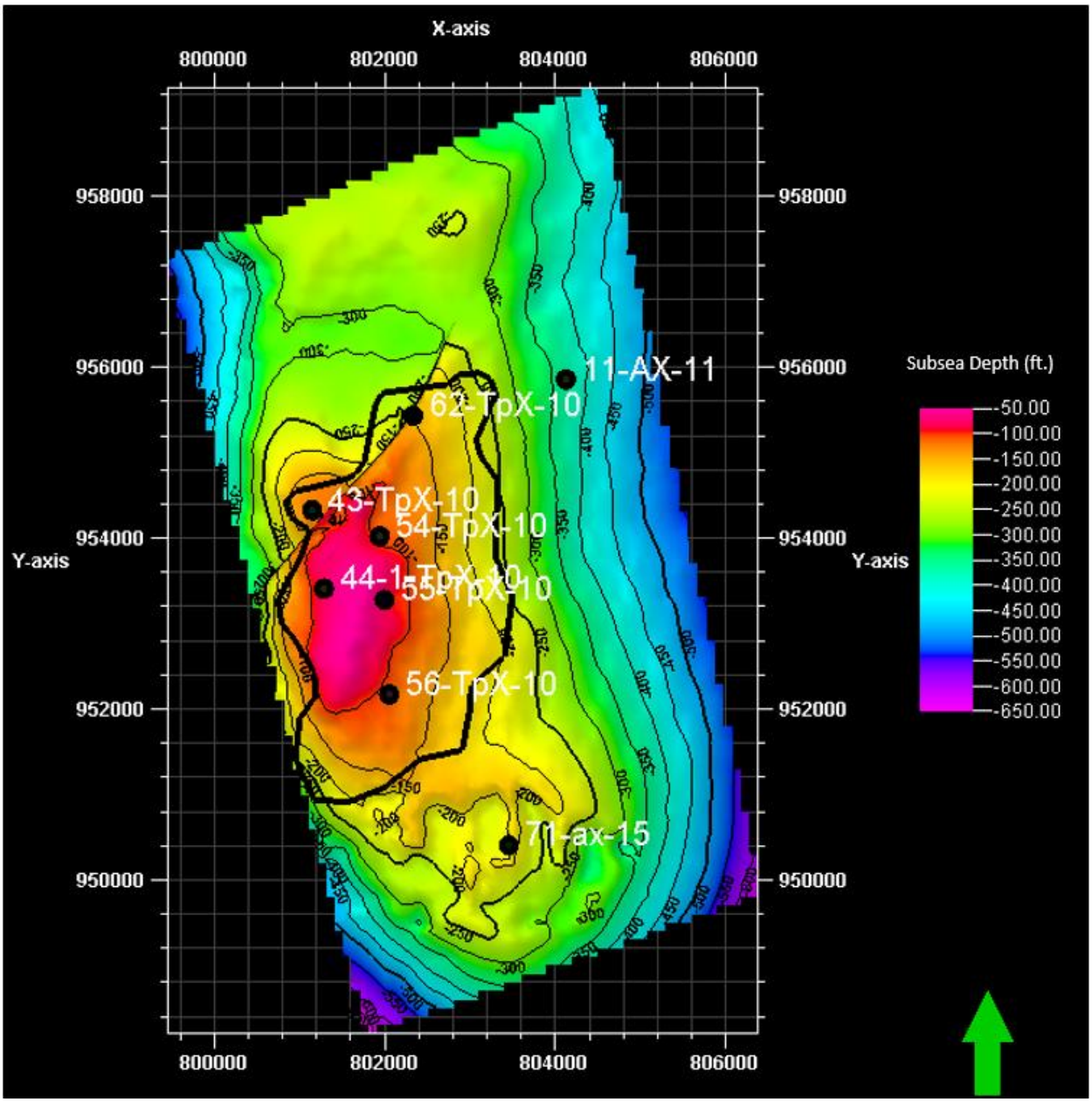

Figure 4-4: Locations of 8 Wells with core data used in Chiaramonte (2009) reservoir modeling study are shown on Tensleep structure. The black polygon over the A Sand horizon shows areal extent of high oil production zones. Subsea depth and coordinates are in feet.

In this study we assign the mean values of porosity and permeability from the cores for each zone as (Table 4-2).

Table 4-3: Matrix porosity (ft^3/ft^3), permeability (mD.), and average cell thickness (ft.) for the Tensleep static model (modified after Chiaramonte (2009)).

Zone	Porosity%	Horizontal permeability	Vertical permeability	Number of the layers	Average cell thickness
A Sand	4.74	3.69	1.11	2	23
B Dolomite	3.03	0.21	0.10	1	26.29
B1 Sand	10.54	29.31	6.14	1	19
B2 Sand	6.95	3.45	1.05	2	26.25
Aquifer	20	10	2.53	8	50

Vertical permeabilities are calculated based on the core data from well 48-X-28 in the Tensleep Formation (RMOTC reports) (Figure 4-5).

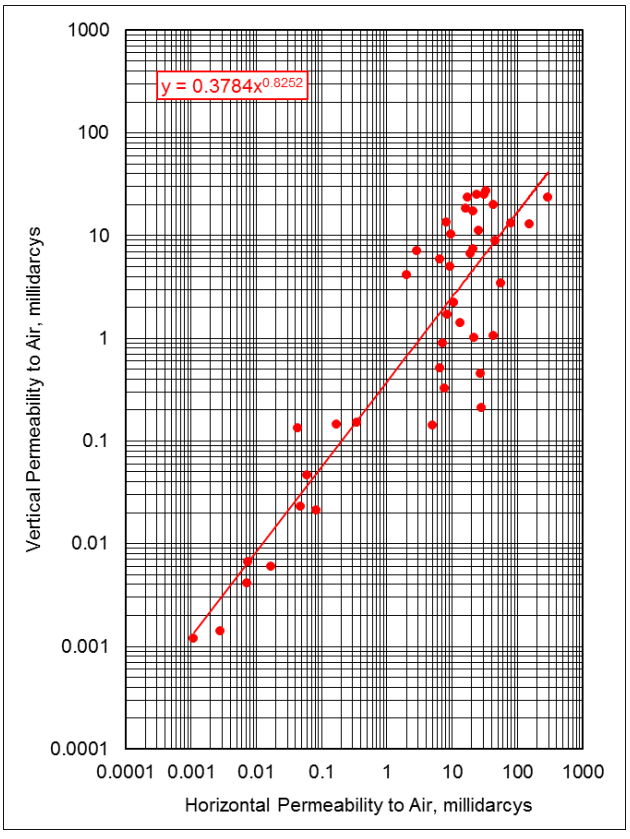

Figure 4-5: The vertical air permeability vs. horizontal permeability in core data from well 48-X-28 (Courtesy of RMOTC).

Fracture intensity: Kavousi and Wilson (2015) used minimum dissimilarity of most negative curvature attribute extracted from post stack 3D seismic data to generate a fracture intensity attribute. The designed fracture intensity is upscaled to the reservoir grid for each zone (Figure 4-6). Fracture intensity average for all zones varies from 1 fracture per feet to 1 fracture per 10ft. These two limits are the maximum and minimum fracture intensities reported for the Tensleep Formation by Chiaramonte (2009). She assigned a constant fracture intensity of 1 fracture every 10ft for A Sand, 1 fracture every 10ft for B Sand, 1 fracture every 3ft for B Dolomite, and one fracture per feet for C Dolomite and C Sand. These values were assigned based on Lorenz and Cooper (2004) observations from core data of well 48-X-28.

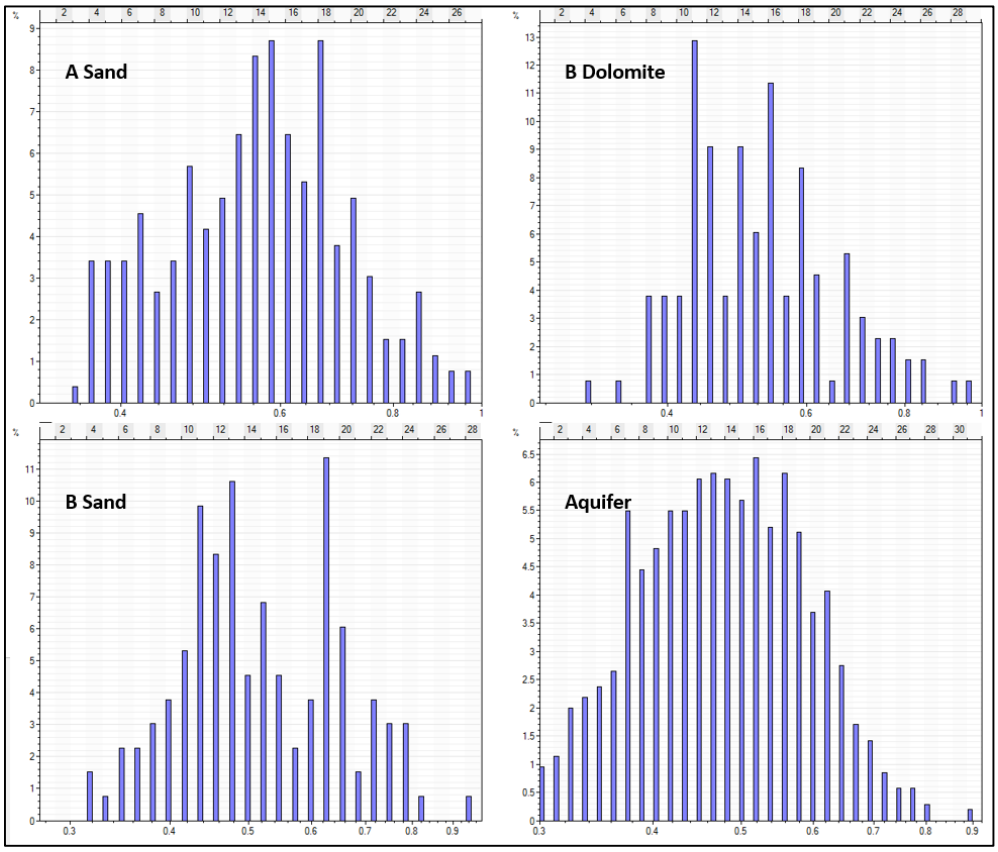

Figure 4-6: distributions of the fracture intensity attribute for each zone in the grid. Note that the B Sand fracture intensity histogram consists of the B1 Sand and B2 Sands. The aquifer includes C Dolomite and C sand.

Kavousi and Wilson (2015) qualitatively relate the fracture intensity attribute to the production history of the field. They showed that wells located on NW seismic discontinuities are in general more productive that wells located on the NE direction. NW discontinuities are interpreted as possible open fracture zones which mainly include N76°W fracture set (Figure 4-7). Wilson et al. (2015) showed that the dominant fracture set (N76°W) is roughly parallel to the present-day maximum horizontal compressive stress (S_{hmax}) inferred from drilling induced fractures. They also interpreted permeability barriers roughly parallel to the S_1 fault.

In this study, NE seismic discontinuities are interpreted as possible low-permeability deformation bands (Figure 4-7). Chiaramonte (2009) showed that a 3300 psi reservoir pressure increase is necessary to make the S_1 fault leaky in the Tensleep Formation at Teapot Dome. We assume the same threshold pressure along the S_1 fault and along the interpreted permeability barriers roughly parallel to the S_1 fault during the flow simulation. This threshold pressure is included in flow simulation as the maximum bottom hole pressure for injectors.

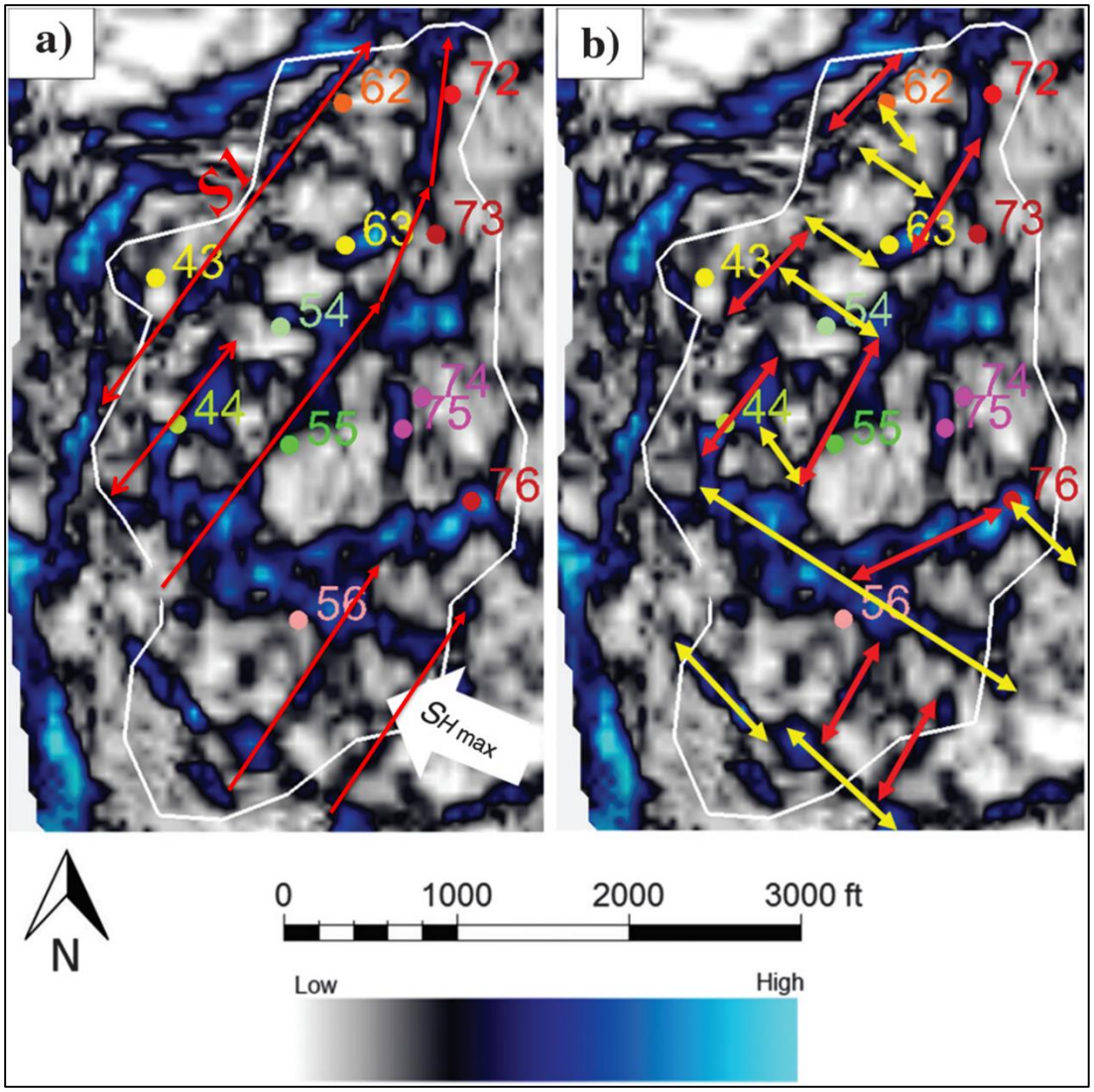

Figure 4-7: a) Possible deformation bands are shown by red arrows, note that they are parallel to sub-parallel to the S_1 fault. b) The fracture intensity attribute introduced by Kavousi and Wilson (2015). Wells located on the NW discontinuities (yellow arrows) are more productive than wells on the NE discontinuities (red arrows).

The interpreted permeability barriers along with S_1 fault are incorporated into the static model of the Tensleep reservoir (Figure 4-8). Note that model S_1 fault does not exactly follow the real S_1 fault with strike of N37°E (Figure 4-8). S_1 fault and permeability barriers are constrained to flow the grid boundaries. Thus, their trend is an average around N30°E.

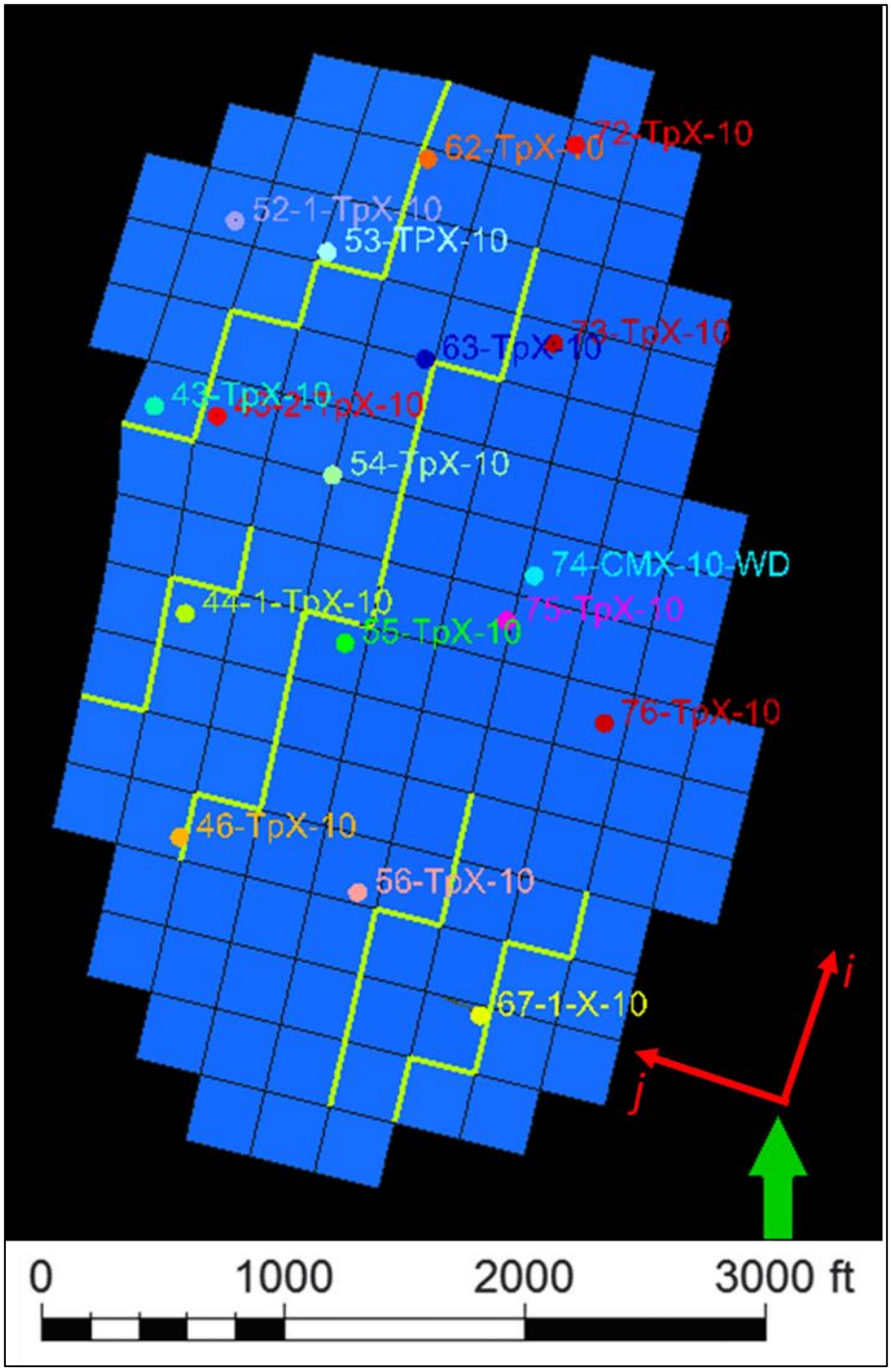

Figure 4-8: The permeability barriers are roughly parallel the S1 fault. The grids j direction is almost parallel to the dominant fracture set (N76°W). The grid block size is 300ft by 300ft. Note $K_{xx}=K_i$ and $K_{yy}=K_j$.

Aquifer: The Tensleep reservoir at Teapot Dome has a strong aquifer and a water drive production mechanism (Friedman and Stamp, 2006). The Mississippian Madison Limestone is the

regional aquifer that provides the reservoir water drive for the Tensleep reservoir at Teapot Dome (RMOTC). The model aquifer is located directly below the B2 sandstone and maintains the reservoir pressure around 2300 psi to 2350 psi.

Rock Physics

Matrix Relative permeabilities: Relative permeability laboratory tests are made on Sample *A* from well 62-TPX-10 and samples *B, C,* and *D* from 43-TPX-10 (RMOTC reports). The relative permeabilities for water-oil and oil-gas phases are illustrated in Figure 4-9. The initial oil saturation (S_{ro}) and water saturation (Sw_i) vary from 12.5% to 22.1% and 28.7% to 56.3% respectively (Gaviria, 2005).

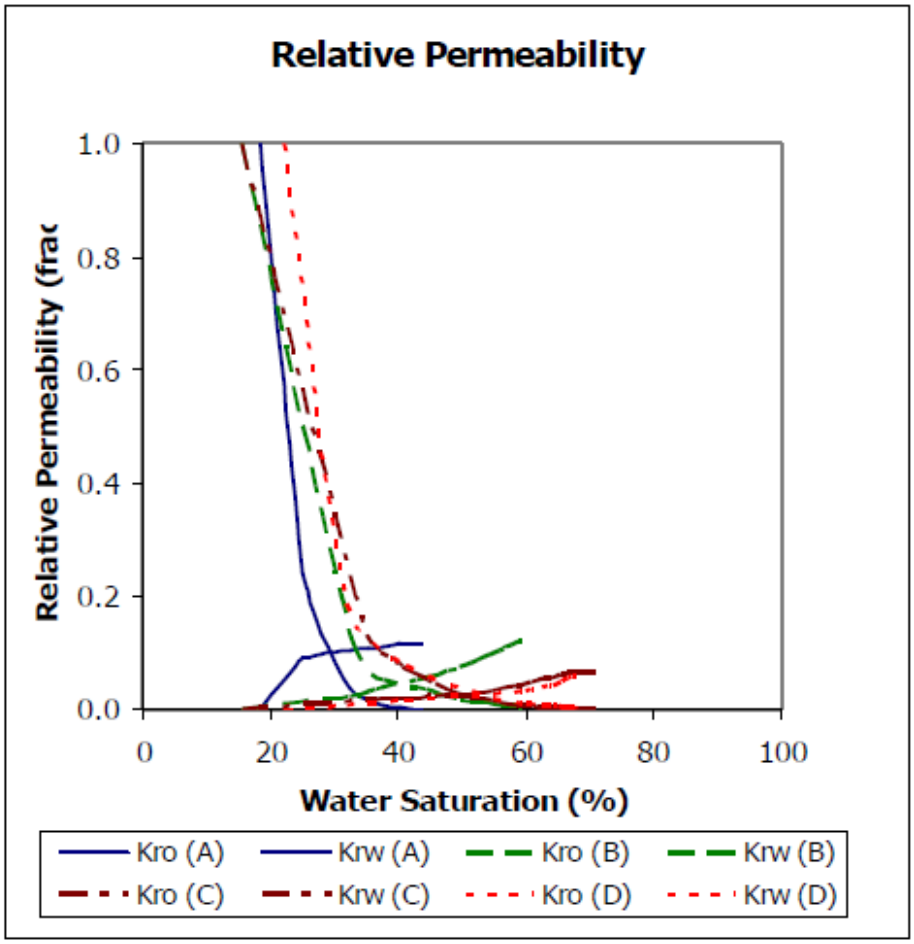

Figure 4-9: The relative permeability of 4 samples from the Tensleep reservoir (after Gaviria 2006).

The samples in Figure 8 are smoothed by Gaviria (2005) for oil-water (Figure 4-10A) and oil-gas phases (Figure 4-10B).

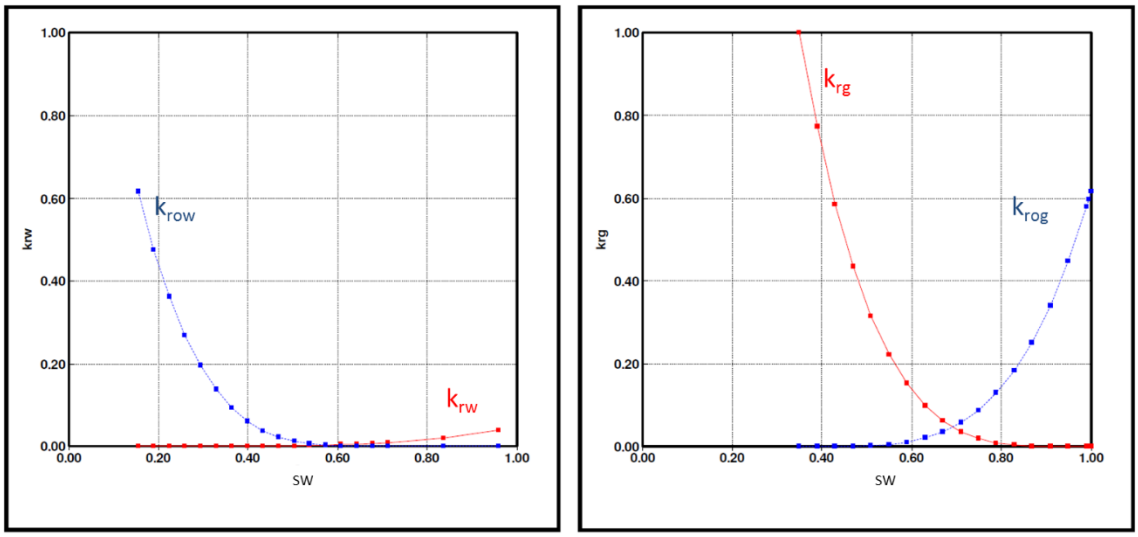

Figure 4-10: A) The smoothed relative permeability of the oil-water system obtained for a sample from Tensleep reservoir. B) Gas-oil relative permeabilities (after Gaviria, 2006).

Fracture Relative permeabilities: There are no available relative permeability data for fractures in the Tensleep Formation. Typically the relative permeability of fractures for each phase is assumed to vary lineally with the phase saturation (Gaviria, 2006) (Figure 4-11). The original experiment by Romm (1966) was implemented on two parallel glass plates. The results showed a linear dependency between phase relative permeability and phase saturation. However, this assumption ignores fracture rugosity due to compaction or mineralization. Moreover, the capillary pressure and wettability can also affect the fluid flow interference (Gaviria, 2006).

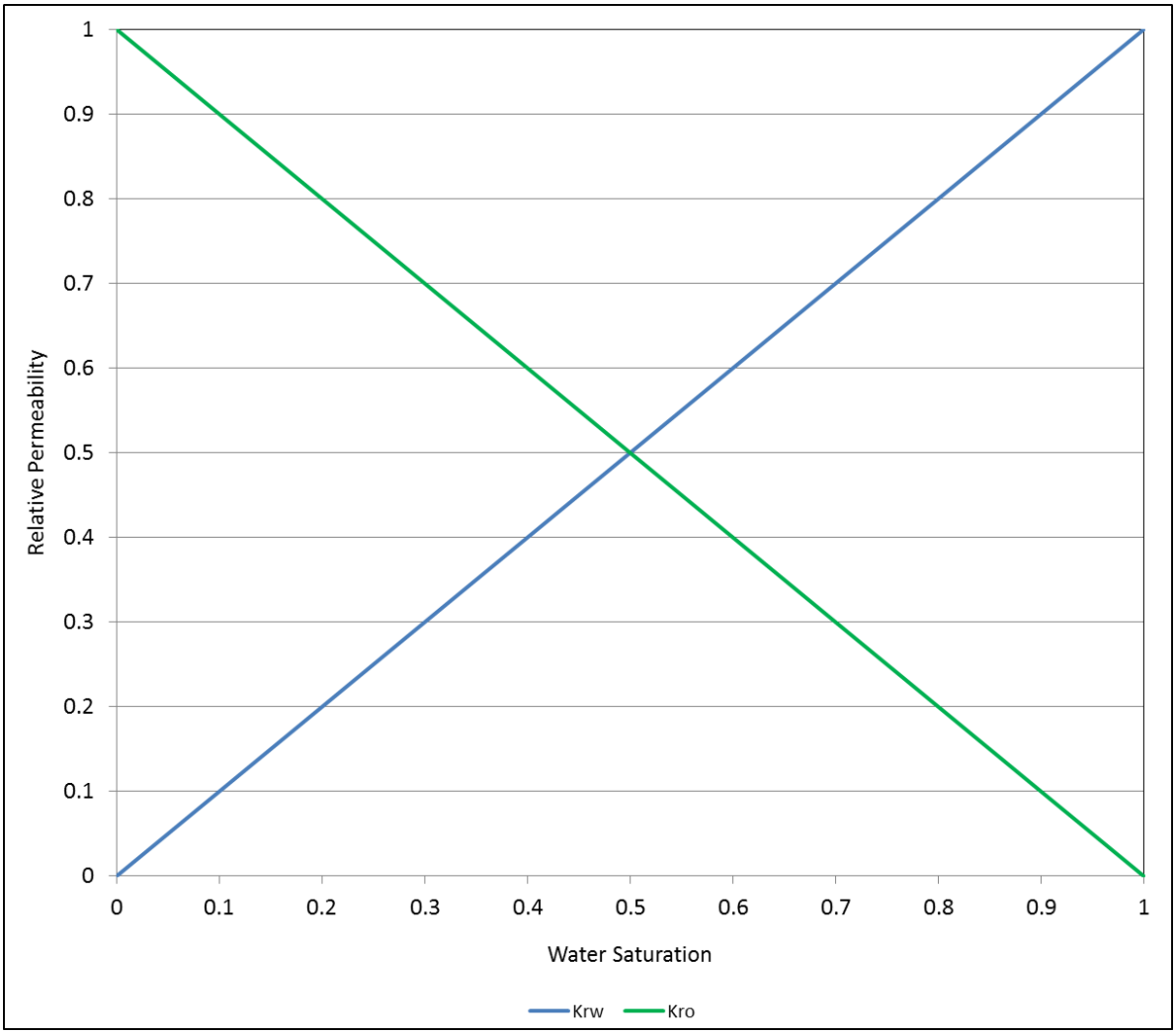

Figure 4-11: Oil-water relative permeabilities are assumed to vary linearly with water saturation.

Capillary Pressure: Capillary pressure tests were carried out for three samples using an air-brine system (Gaviria, 2006). Sample *E* from well 56-TPX-10 and sample *F* and *G* from 44-1-TPX-10 (Figure 4-12). The analysis showed a low displacement pressure (1psi) which indicates well sorted grains (Van Golf-Racht, 1982).

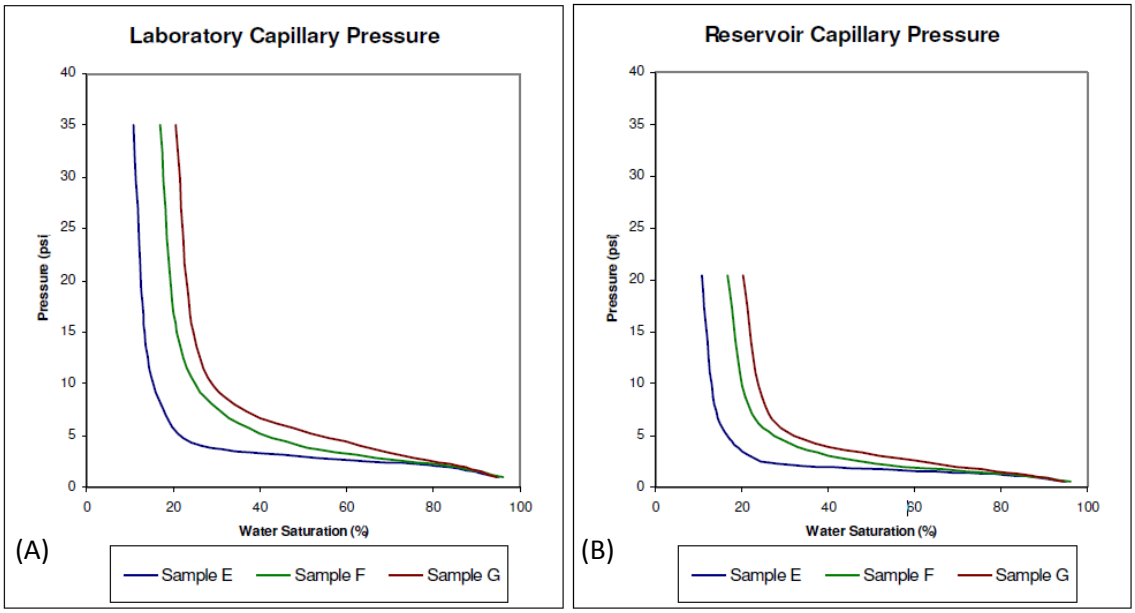

Figure 4-12: A) Capillary pressure test is carried out for sample E, F, and G using an air-brine system. The curves show the pressure needed to decrease water saturation in the samples. B)The capillary pressure curves are adjusted for oil-water system (190.4 °F) (after Gaviria, 2006).

PVT Analysis

Oil production from the Tensleep reservoir at Teapot Dome consists of a sulfurous saturated black oil (Gaviria, 2006). The fluid properties are summarized in Table 4-3.

Table 4-4: Oil properties of the Tensleep reservoir at Teapot Dome, Wyoming (RMOTC reports).

Gas-oil ratio	4 SCF/STB
Initial reservoir pressure at -110ft subsea	2300 psi
Oil Gravity	31° API
Bubble point pressure	40-70 psi
Oil viscosity at 60°F and 42psi	3.5 cp
Minimum Miscibility Pressure(MMP)	1300 psi

Only one oil sample is available with swelling tests by Hycal Energy Resource Laboratories which shows oil volume and viscosity variations with amount of CO_2 injected at a reservoir temperature of 190.4°F (Hycal, 2004). The sample is from well 72-TPX-10 taken in 2004. It has very low amounts of light components (Methane, Ethane and propane) and abundant heavy components up

to C30+.This could explain the low bubble point pressure between 40-70psi and very low GOR of 4 SCF/STB (Table 4-4)(Gaviria, 2006).

Table 4-5: The oil sample composition at the surface condition.

Component	**Sample Mole Fraction**
CO_2	0.08
N_2	0.13
C_1	0.02
C_2	0.12
C_3	0.17
i-C_4	0.08
n-C_4	0.22
i-C_5	0.15
n-C_5	0.3
C_6	1.29
C_{7+}	97.44
Mole Weight C_{7+}	303.85
Density $C_{7+\text{ at }60°F,\ gr/cm^3}$	0.8972
Temperature(°F)	190.4

An equation of state (EOS) is necessary to analytically predict oil phase behavior during CO_2 injection process. Peng-Robinson (1976) EOS is one of most the popular equations for PVT descriptions of non-ideal gas and gaseous hydrocarbons. The three parameters EOS (Equation 1) is used in this study.

$$P = \frac{RT}{v-b} - \frac{a(T)}{v(v+b)+b(v-b)} \qquad (1)$$

Where P is pressure, R is the gas constant, T is the absolute temperature, v is molar volume.

b and $a(T)$ are:

$$b = 0.07780\frac{RT_c}{P_c} \qquad (2)$$

$$a(T) = 0.45724 \frac{R^2 T_C^2}{P_c} \propto (T) \quad (3)$$

Where,

$$\propto (T) = \left[1 + m\left(1 - \left(\frac{T}{T_c}\right)^{0.5}\right)\right]^2 \quad (4)$$

And m, the intermediate function in equation of state is

$$m = 0.37464 + 1.54226\omega - 0.26992\omega^2 \quad (5)$$

T_c is critical temperature, P_c is critical pressure and ω is acentric factor (i.e. measure of non-sphericity of molecules). Thus, a 3-parameter Peng-Robinson EOS should be adjusted for a mixture of compounds to find molar volumes v. The three parameters T_c, P_c and ω are known for some compounds such as methane, ethane, and etc. However, oil samples from reservoirs typically have thousands of complex compounds with unknown T_c, P_c and ω (Gaviria, 2006). Thus, a calibration with the laboratory PVT data is usually necessary to obtain a reliable EOS.

Gaviria (2006) split C_{6+} components of Sample *A* into five pseudo-components C_6-C_{12}, C_{13}-C_{19}, C_{20}-C_{27}, C_{28}-C_{29} and C_{30+}. The resulted Peng-Robinson Equation of State (EOS) parameters with 13 components parameters are summarized in table 4-5. Gaviria (2006) matched the EOS response with the swelling tests laboratory data (Figure 4-13).

The simulation speed depends on number of components in EOS (Gaviria, 2006). We performed a lumping on Gaviria's EOS components to fit an 8 component EOS to the laboratory data. The 8 component EOS is presented in Table 4-6.

Table 4-6: The Peng-Robinson EOS parameters for 13 components (after Gaviria (2006)).

Component	Mw	PC(atm)	Tc(K)	Omega A	Omega B	Acentric factor	Vc(ft^3/lb-mole)
CO_2	44.0	72.8	304.2	0.4572	0.0778	0.225	0.094
C_1	16.0	45.4	190.6	0.4572	0.0778	0.008	0.099
C_2	30.1	48.2	305.4	0.4572	0.0778	0.098	0.148
C_3	44.1	41.9	396.8	0.4572	0.0778	0.152	0.203
iC_4	58.1	36.0	408.1	0.4572	0.0778	0.176	0.263
nC_4	58.1	37.5	425.2	0.4572	0.0778	0.193	0.255
iC_5	72.2	33.4	460.4	0.4572	0.0778	0.227	0.306
nC_5	72.2	33.3	469.6	0.4572	0.0778	0.251	0.304
C_6-C_{12}	121.2	26.9	592.5	0.4572	0.0778	0.342	0.468
C_{13}-C_{19}	219.4	17.6	732.5	0.4572	0.0778	0.595	0.809
C_{20}-C_{27}	323.5	13.4	829.0	0.4572	0.0778	0.823	1.114
C_{28}-C_{29}	398.0	11.5	884.3	0.4572	0.0778	0.981	1.307
C_{30+}	637.6	8.1	1030.0	0.4572	0.0778	1.289	1.816

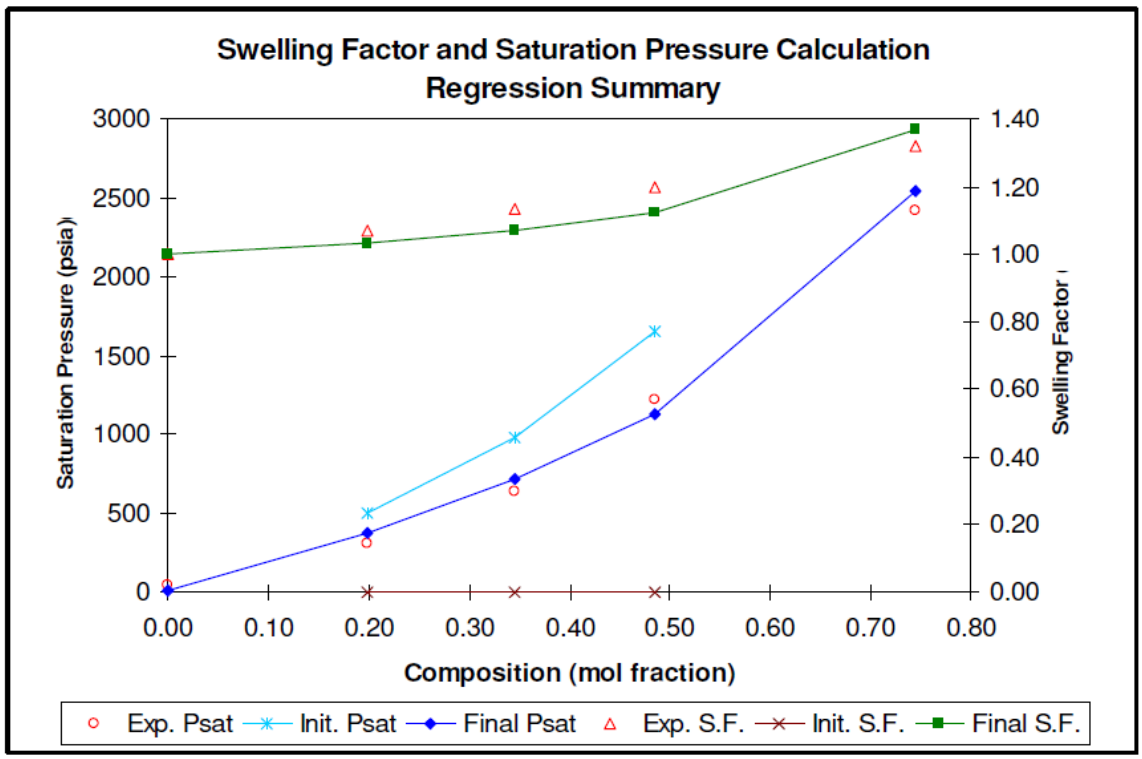

Figure 4-13: The swelling tests for the 13 component EOS and experimental data (from Gaviria (2006)). The horizontal axis "Composition" shows the mole fraction of CO_2 added to the oil sample. Init Psat and Init S.F. are modeled saturation pressure and swelling factor before regression.

Table 4-7: The 8-components Peng-Robinson EOS parameters.

Component	Mw	PC (atm)	Tc (°K)	Omega A	Omega B	Acentric factor	Vc (lb./mole)
CO_2	44.0	72.8	304.2	0.4572	0.0779	0.225	0.094
C1-C3	22.6	46.1	215.1	0.4572	0.0779	0.048	0.10961
C4-C5	93.9	34.0	458.1	0.4572	0.0779	0.478	0.2868
C6-C12	157.4	25.9	566.1	0.4572	0.0779	0.556	0.4725
C13-C19	215.04	15.6	734.2	0.4572	0.0779	0.558	0.8194
C20-C27	467.12	14.4	809.8	0.4572	0.0779	0.790	1.119636
C28-C29	518.9	9.3	810.2	0.4572	0.0779	0.948	1.306902
C30+	632.3	5.3	838.9	0.4572	0.0779	1.201	1.888011

The 8 component EOS parameters are tuned to fit the swelling test data from well 72-TPX-10 oil sample. The resulting EOS properly outputs the oil sample response to the swelling tests (Figure 4-14). The swelling tests show that oil responds to CO_2 injection with volume increase and viscosity reduction. We modeled the liquid viscosity at each swelling test step and compared that with laboratory results (Figure 4-15). The 8-component EOS simulates the liquid viscosity reductions with a reasonable error at each swelling test step.

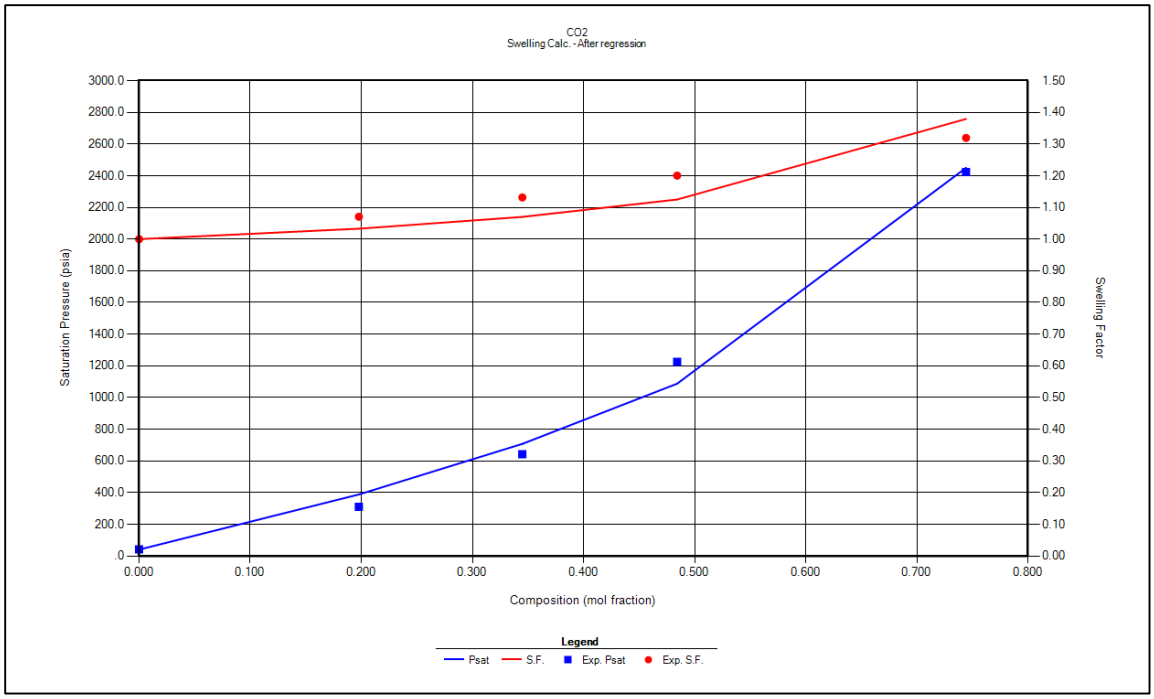

Figure 4-14: Saturation pressure and swelling factor calculated in the swelling experiments and model EOS are plotted against mole fraction CO_2 added to the oil sample from well 72-TPX-10 at 190.4°F. The saturation pressure increases as higher mole fraction of CO_2 is added to the fluid sample.

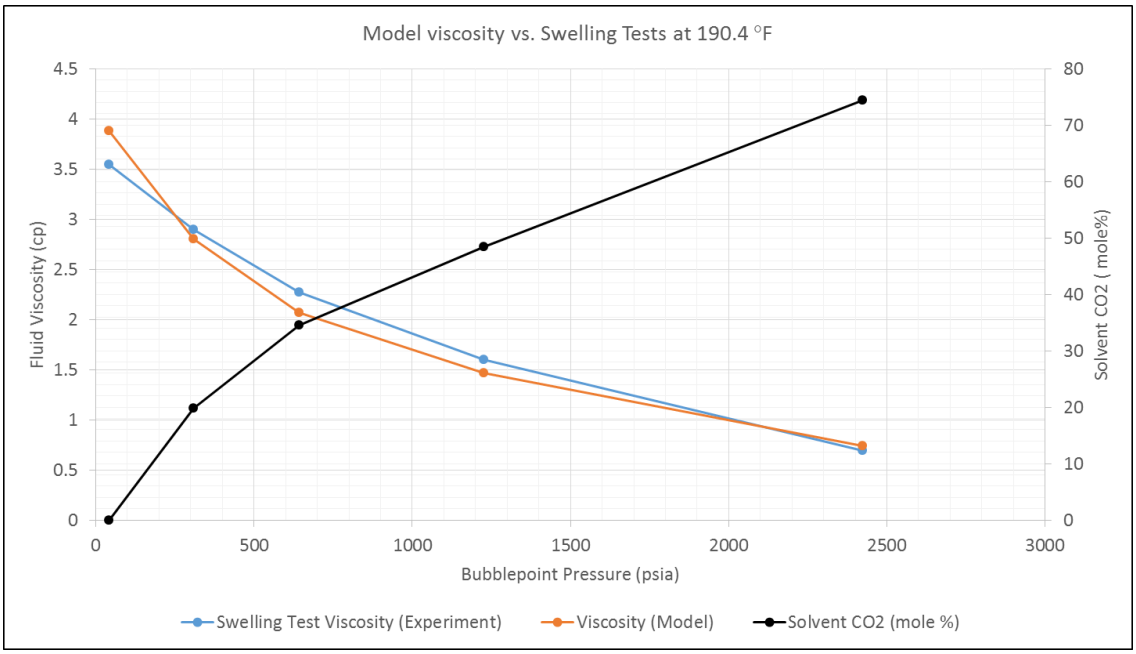

Figure 4-15: Fluid viscosity is plotted vs. bubble point pressure at each swelling test step. The modeled viscosity reduction curve (orange line) is close to the swelling test viscosity results (blue line).

The viscosity reduction at the reservoir condition (2330 psi, 190.4°F) after CO_2 injection is modeled (Figure 4-16). The viscosity reduction from 3.45cp to 0.9cp is obtained from the fitted EOS.

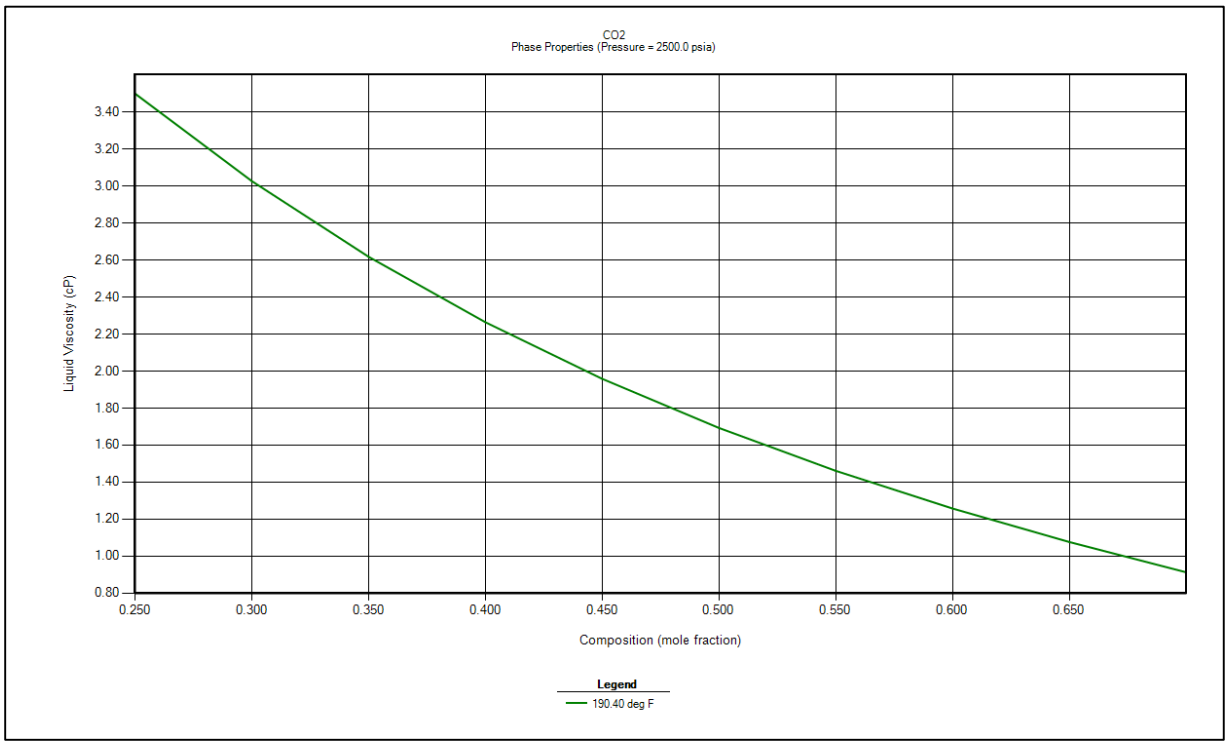

Figure 4-16: The oil viscosity at the reservoir temperature (190.4°F) and pressure (2330 psi) versus mole fraction of CO_2. The oil viscosity decreases by adding more CO_2 mole fractions.

History matching

We perform a sensitivity analysis on the fracture aperture and tune the reservoir model to obtain a production history match. The history matching in this study has a high degree of uncertainty. There are two main sources of uncertainty. Bottom-hole pressures and perforation intervals are not known for the producers.

We add two constraints to diminish uncertainties for fluid flow simulation. We build a static model that contains 3.8 million bbl. oil (i.e. add an original oil in place constraint) as estimated by Friedman and Stamp (2006). Secondly, the field water production (the dominant produced phase)

is set as a production constraint and the model fracture aperture distribution and fracture vertical permeabilities are changed to obtain an oil production history match.

Sensitivity analysis: We set the model DFN fracture aperture as an uncertain parameter which needs to be tuned in the history matching. As mentioned in Chapter 2, Dershowitz (2000) simplified Oda (1985) formulations for upscaling fracture permeability tensor as,

$$k_{ij} = \lambda\left(F_T\,\delta_{ij} - F_{ij}\right) = \begin{bmatrix} k_{ii} & k_{ij} & k_{ik} \\ k_{ji} & k_{jj} & k_{jk} \\ k_{ki} & k_{kj} & k_{kk} \end{bmatrix} = \lambda \begin{bmatrix} F_T & 0 & 0 \\ 0 & F_T & 0 \\ 0 & 0 & F_T \end{bmatrix} - \lambda \begin{bmatrix} F_{ii} & F_{ij} & F_{ik} \\ F_{ji} & F_{jj} & F_{jk} \\ F_{ki} & F_{kj} & F_{kk} \end{bmatrix}$$

$$= \lambda \begin{bmatrix} F_T - F_{ii} & F_{ij} & F_{ik} \\ F_{ji} & F_T - F_{jj} & F_{jk} \\ F_{ki} & F_{kj} & F_T - F_{kk} \end{bmatrix} \tag{6}$$

λ is a dimensionless constant with the restriction $0 < \lambda \leq \frac{1}{12}$,and F_{ij} is a symetric second order tensor that expresses fracture flow as a vector along the fracture unit normal. F_T is the Trace of fracture tensor as,

$$F_T = F_{\mathrm{ii}} + F_{\mathrm{jj}} + F_{\mathrm{kk}} \tag{7}$$

Each component in F_{ij} tensor can be calculated as,

$$F_{ij} = \frac{1}{V}\sum_{k=1}^{N} A_k T_k n_{ik} n_{jk} \tag{8}$$

Where T_k is fracture transmissibility of k^{th} fracture with aperture e_k as,

$$T_k = \frac{{e_k}^3}{12} \tag{9}$$

Substituting T_k from Equation 9 into Equation 8 yields,

$$F_{ij} = \frac{1}{12V}\sum_{k=1}^{n} A_k e_k^3 n_{ik} n_{jk} \tag{10}$$

Where V is grid block volume, A is the fracture area, n_{ik}, n_{jk} are components of the unit normal vector of the k^{th} fracture. Equation 10 shows a projection of the flow volume into desired Cartesian system.

Doubling the fracture aperture in equation 10 will increase tensor permeability components by a factor of 8 in equation 6. We tested the cubic relationship for a limited number of cells in B1 Sand fracture network. Results show that the permeability tensor will vary cubically with the aperture multiplier (Figure 4-17).

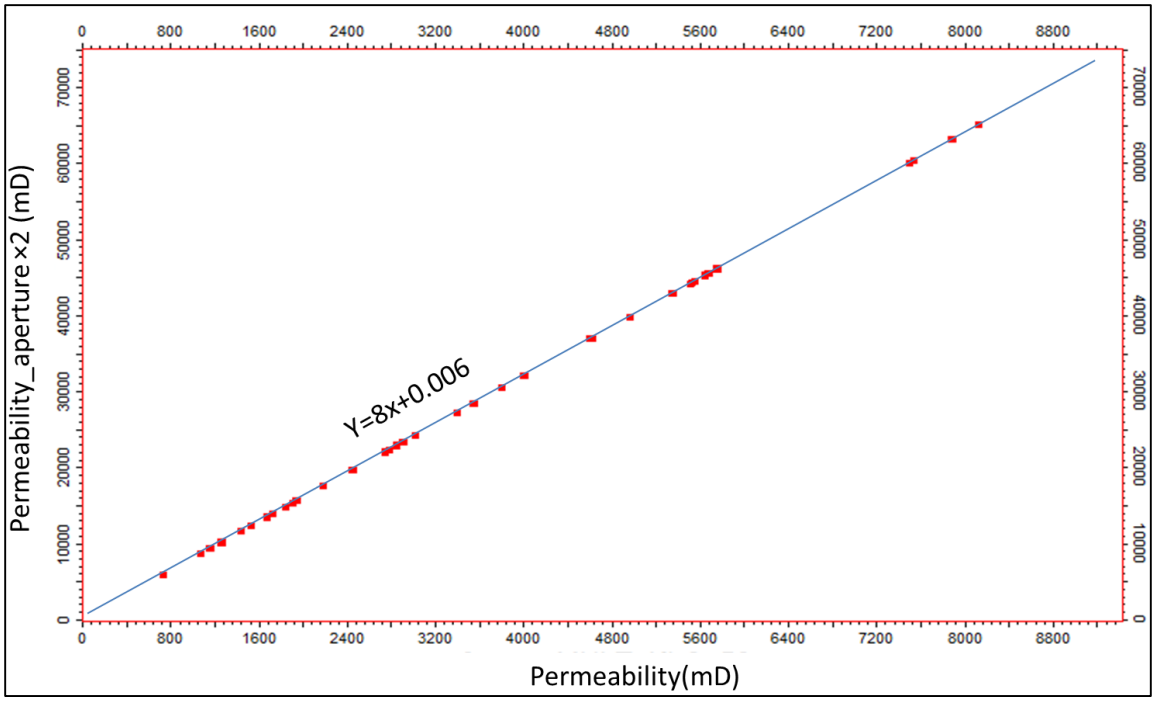

Figure 4-17: Doubling the fractures apertures in a model DFN will multiply its upscaled permeability tensors by 8.

Thus, we use the static model along with an uncertain multiplier (MLT) for the fracture apertures in the history matching process. The results show that an aperture multiplier of 5 (i.e. a

permeability multiplier of 5^3=125) considerably increases model oil production and decreases the difference between model oil production and the field oil production history (Figure 4-18). This aperture multiplier places the aperture distribution closer to those measured in well 48-X-28 cores (Figure 4-19).

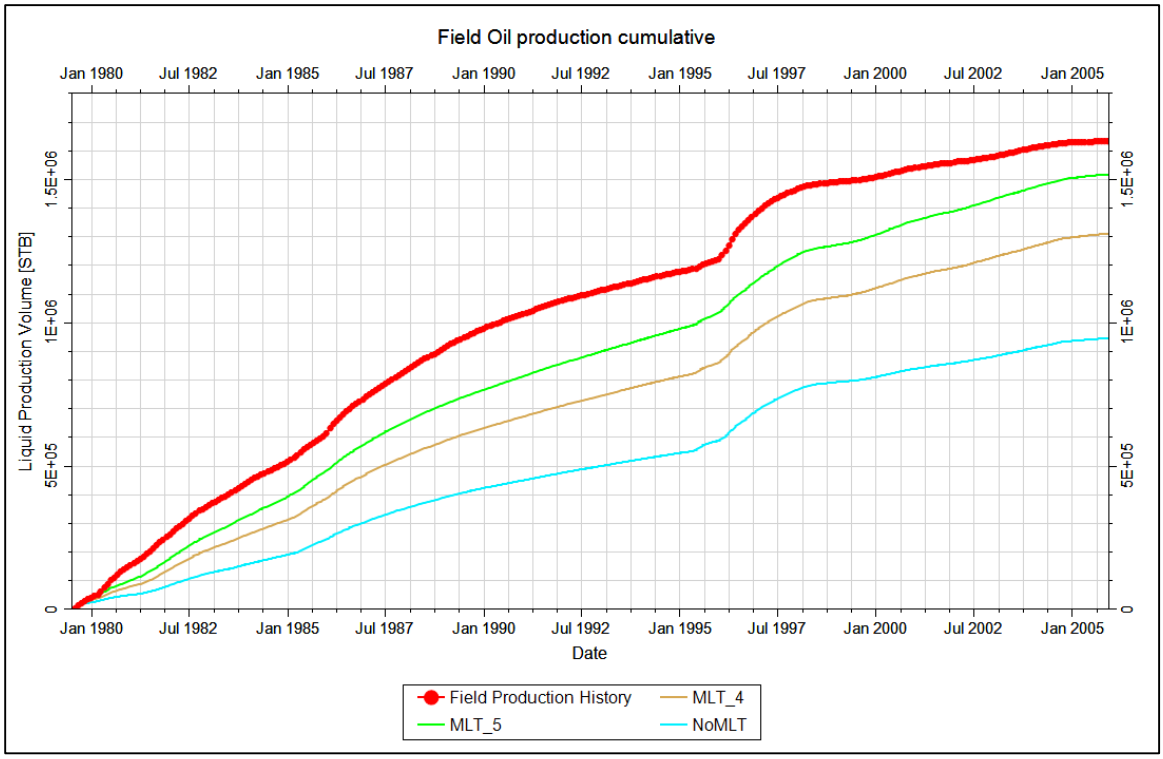

Figure 4-18: Field oil production cumulative for aperture multiplier (MLT) of 1, 4, and 5. A multiplier of 5 brings the model oil production closer to the history data (a permeability multiplier of 125 for K_x, K_y, and K_z). K_z is changed in the next step to obtain a closer match.

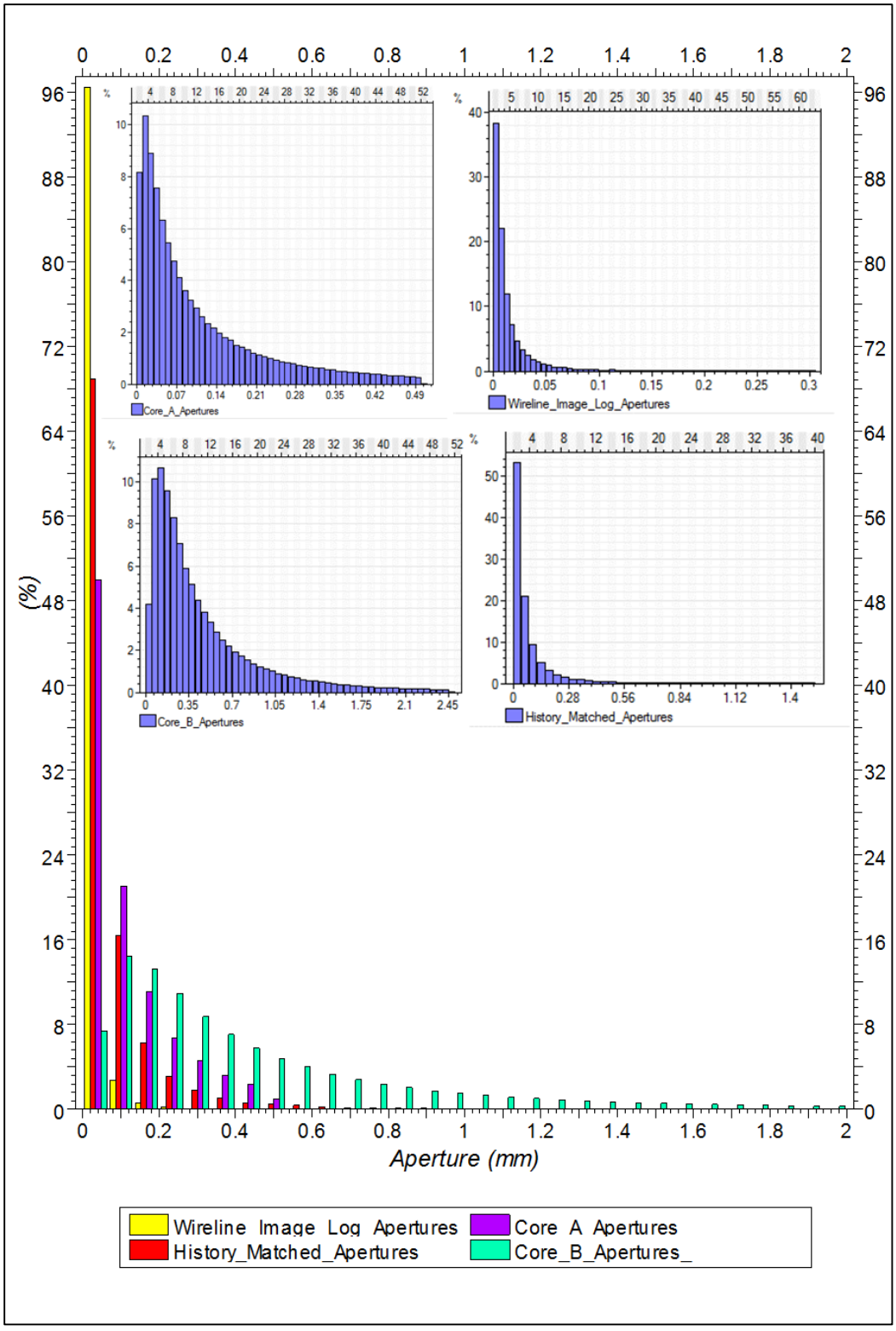

Figure 4-19: Figure 4-2 is modified to include the history matched aperture distribution. History matched model has aperture distribution closer to Core A aperture distribution.

We conducted a sensitivity analysis with fractures k_z on a base model with MLT equal to 5 (MLT_5 in Figure 4-18). Results show that lower k_z considerably improves the model oil production (Figure 4-18). We suspected that an aperture MLT of 5 overestimates k_z and causes water conning. Van Golf-Racht (1984) simulated the effect of k_z on water conning effect in a fractured reservoir. He conducted dual porosity flow simulation cases with k_z of 100mD, 10mD, 1mD, and a horizontal (radial) fracture permeability of 1000mD around a well. The water breakthrough time in perforations are 4 days, 40 days, and 400 days, respectively. The water conning effect increases with k_z/k_r ratio. The worst case of water conning in the fractured reservoir happens where $k_r \ll k_z$. An early water conning dramatically lower the oil production from the field (Van Golf-Racht, 1984). The Tensleep reservoir at Northwest Lake Creek oil field, Wyoming is reported to have water coning because of high density of vertical fractures known as "fracture conning" (Green and Ziemer, 1953). Water conning is also reported for the highly fractured Tensleep reservoir at Little Buffalo Field, Wyoming (Lorenz and Cooper, 2013).

Thus, we output the water saturation around well 56-TPX-10 (the most productive well in the field) to evaluate possible water conning. Two cases are conducted to evaluate water conning around the well. The first case has a k_z multiplier of 125 and the second case has a multiplier of 15.625, respectively equivalent to *K_z_original* and *K_z_DividedBy8* models in Figure 4-20. Case 1 water saturation profile reveals that water flows upward from the aquifer through fractures closest to the

well and hinders the oil production from more distant fractures. In case 2 water sweeps the oil within the fractures around the well and decreases oil saturation inside the fractures (Figure 4-21).

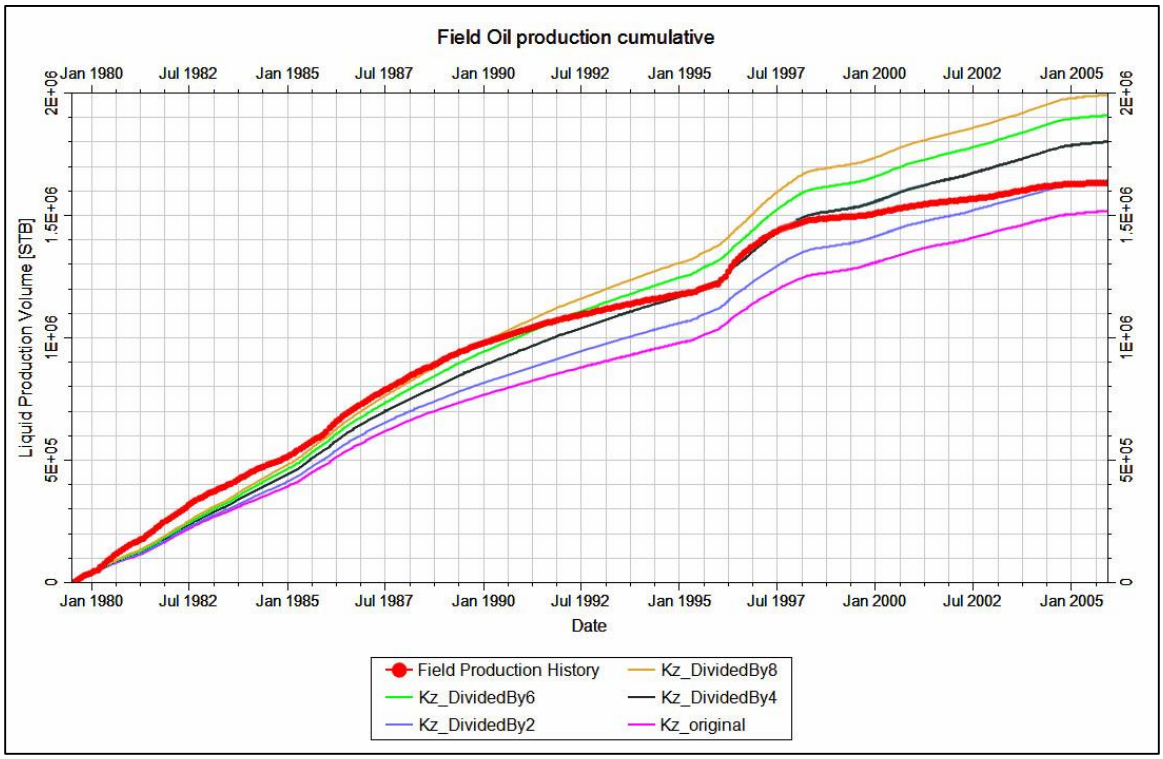

Figure 4-20: The Kz_original is the model with a MLT of 5. Results show that model oil production increases as lower fracture Kz is assigned to grid blocks.

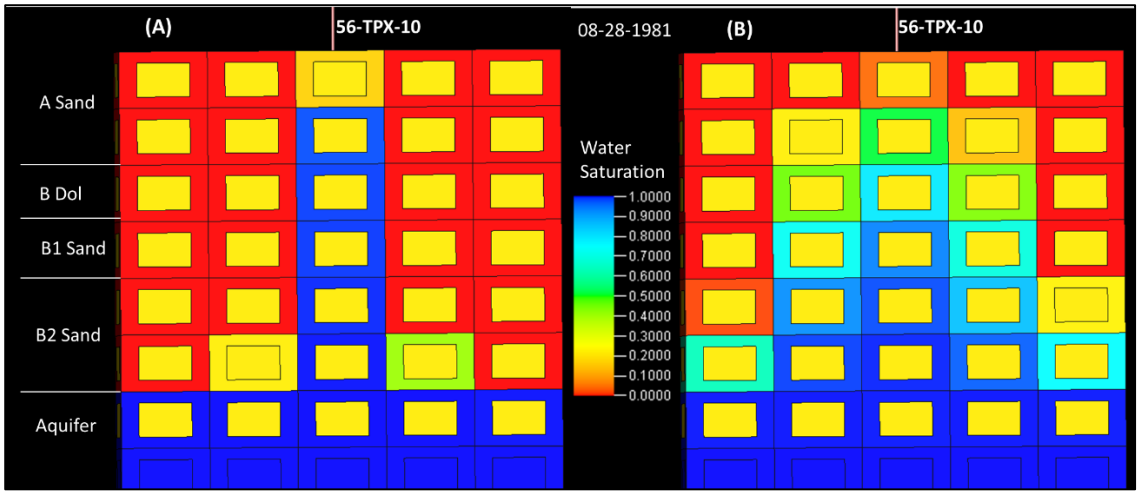

Figure 4-21: A) Water saturation profile around well 56-TPX-10 for case 1 where K_z is multiplied by 125, water flows through fractures close to the well and farther fractures are not affected by aquifer. B) Case two where K_z is multiplied by 15.625. Aquifer influences more fractures and move the oil toward the well. The conning effect is more pronounced in case 1 where oil production is considerably decreased.

We assigned a MLT of 5 and divided the fractures k_z by 2 to get a closer history match (Figure 4-22). This is equivalent to permeability multiplier of 125 for k_x and k_y, and a permeability multiplier of 62.5 for k_z. Additional tuning of the model is performed around several wells to obtain the final history match (Table 4-7).

Table 4-8: Additional tuning of the model (K_z_DividedBy2) around several wells. The rest of the wells in the field are left unchanged.

Well Name	k_x multiplier	k_y multiplier	k_z multiplier
75-TPX-10	0.1	0.1	10
76-TPX-10	0.1	0.1	20
62-TPX-10	150	150	0.005
72-TPX-10	1	1	0.2
73-TPX-10	1	1	0.35
44-1-TPX-10	1	1	20
56-TPX-10	1	1	0.7
63-TPX-10	1	1	0.05

It should be noted that well 62-TPX-10 has permeability multipliers of 150 for horizontal permeabilities. Considering the location of well 62-TPX-10 relative to the S_1 fault (Figure 4-8), one plausible explanation is that the S_1 fault may have a low permeability core surrounded by a

higher permeability zones within the wider damage zone (Wilson et al, 2015; Caine et al. 1996). Thus, higher horizontal permeabilities could be one way to simulate the production history data for well 62-TPX-10. While this reservoir model is non-unique, it is based on field data, is a good approximation of the reservoir fracture network, and provides insights into the influence of reservoir parameters on production variability.

We will show later in this chapter that the transmissibility multiplier for the permeability barriers casts high uncertainties on the oil production from the Tensleep reservoir at Teapot Dome. More oil is produced from the Tensleep reservoir when the permeability barriers are leaky.

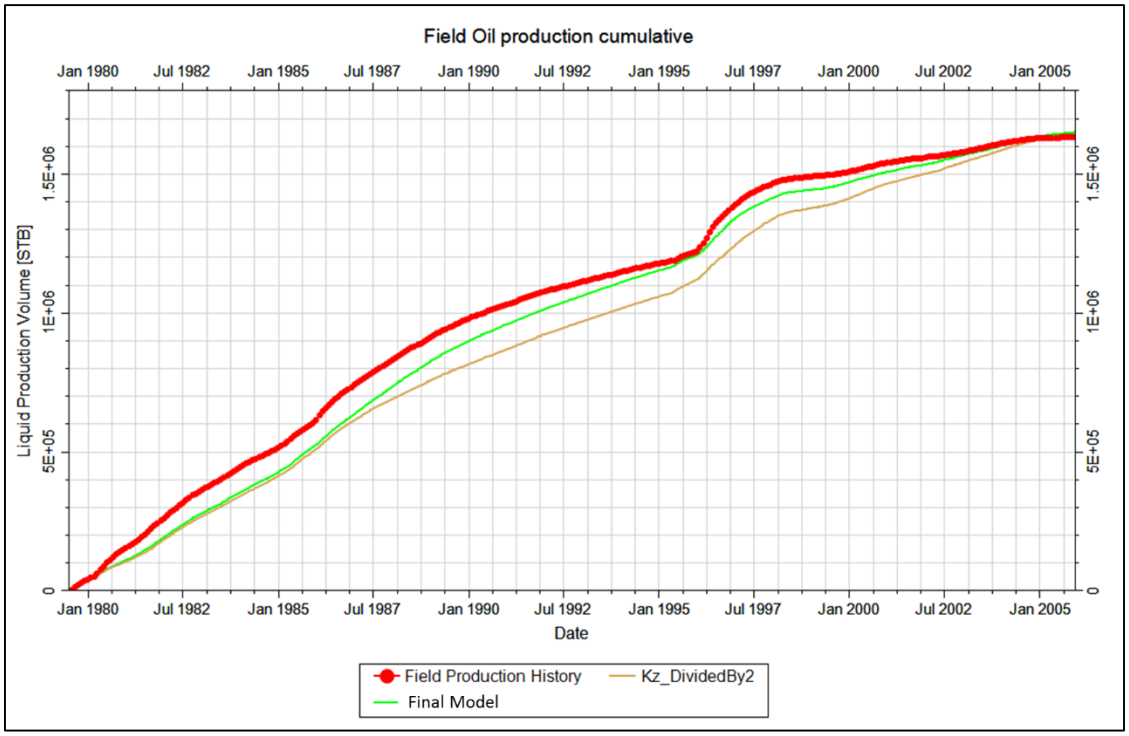

Figure 4-22: The final model is achieved after local tuning of Kz_DividedBy2 model.

The field oil production rates show that the final model approximates the major production history variations observed in the field (Figure 4-23). The final model oil production is shown for main producers in Teapot Dome (Figure 4-24 and 4-25). Although the model oil rate does not perfectly

match the history data, the model ultimately produces cumulative oil volume equal to actual cumulative field production.

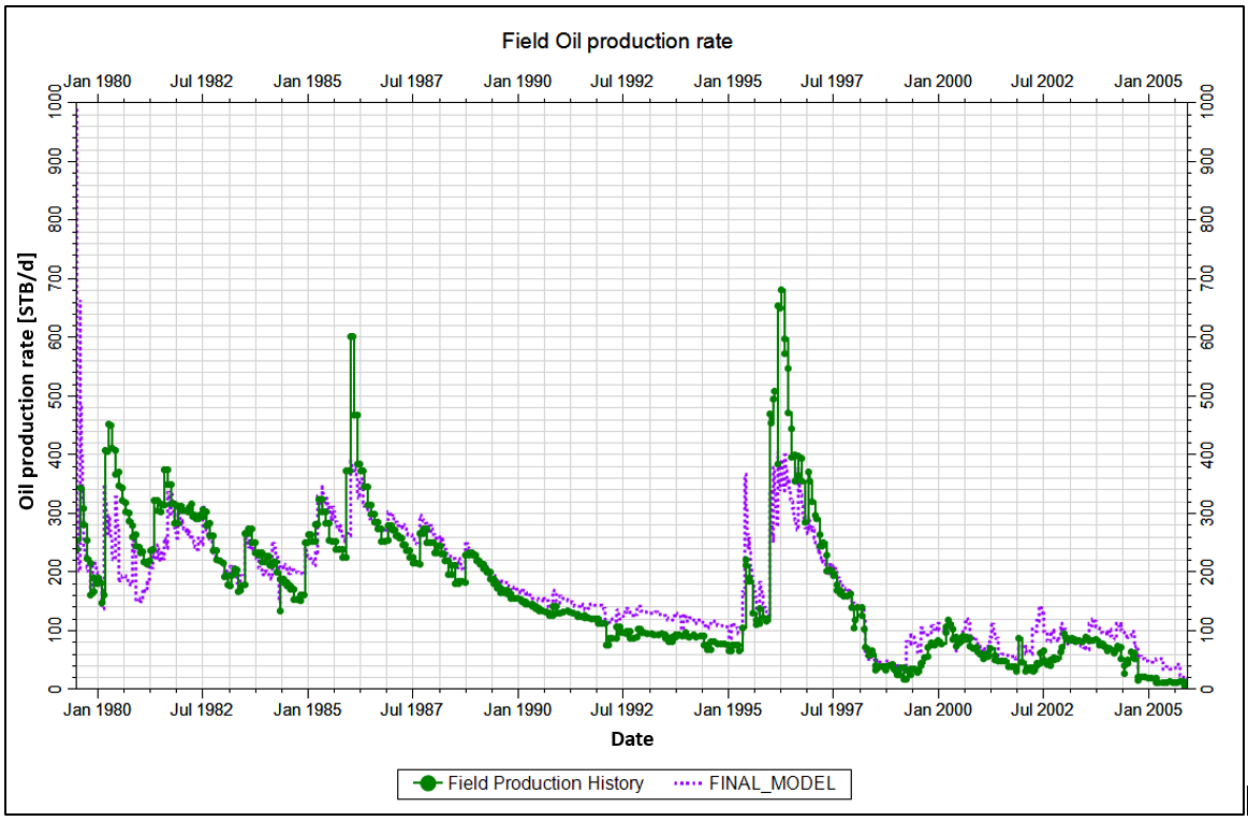

Figure 4-23: Field oil production rate from the final model is shown against the production history data for the entire field. The model production approximates the major variations in field production history.

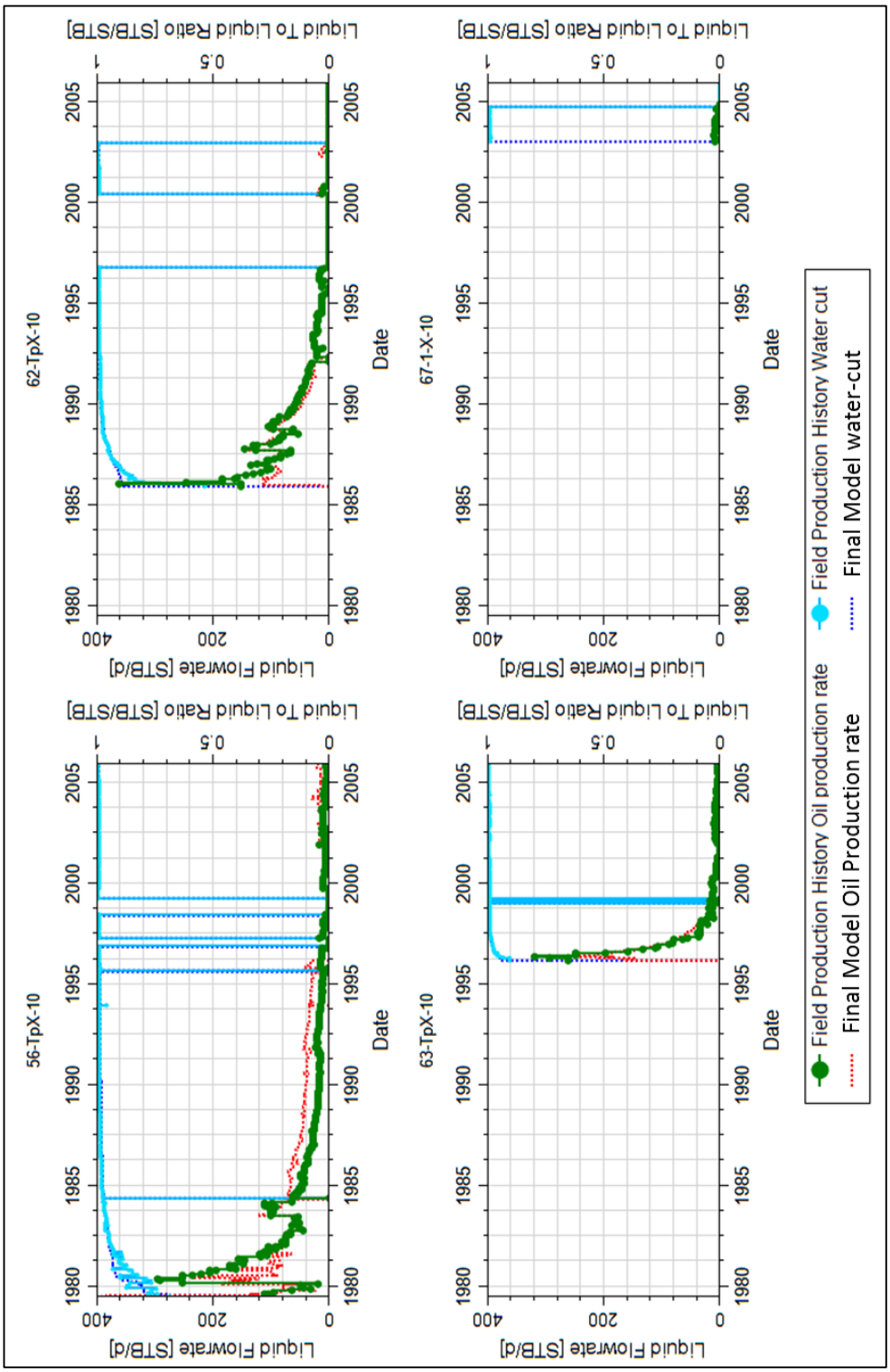

Figure 24: The oil production from the final model and vs production history data for the producing wells in the culmination.

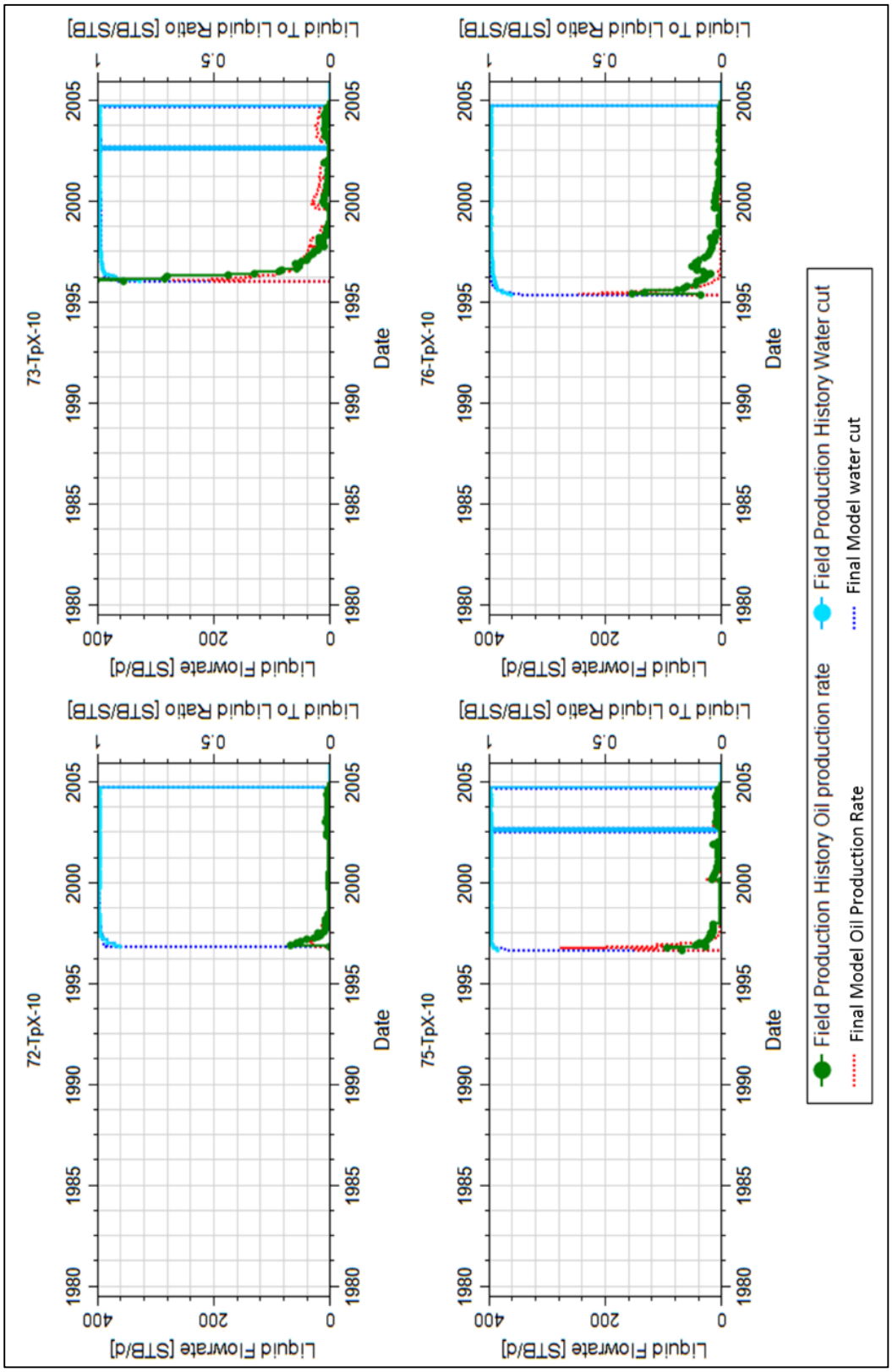

Figure 4-25: The oil production from the final model and vs production history data for several wells.

In the final model all faults are represented as permeability barriers (i.e. transmissibility multiplier equal to 0). We implemented a sensitivity analysis (SA) on the fault transmissibility multiplier and for the permeability barriers. The Eclipse uncertainty parameter MULTFLT is used to control the sealing quality of the faults. A MULTFLT equal to 1 represents a completely leaky fault, while a MULTFLT equal to zero shows a sealing fault. The sensitivity analysis shows that oil production is at its minimum when faults are sealing and at a maximum when faults are completely leaky (Figure 4-26). The uncertainty amount is around 300 MSTB in cumulative oil production. We will consider MULTFLT parameter as uncertain in the CO_2-EOR analysis conducted for the Tensleep Reservoir at Teapot Dome.

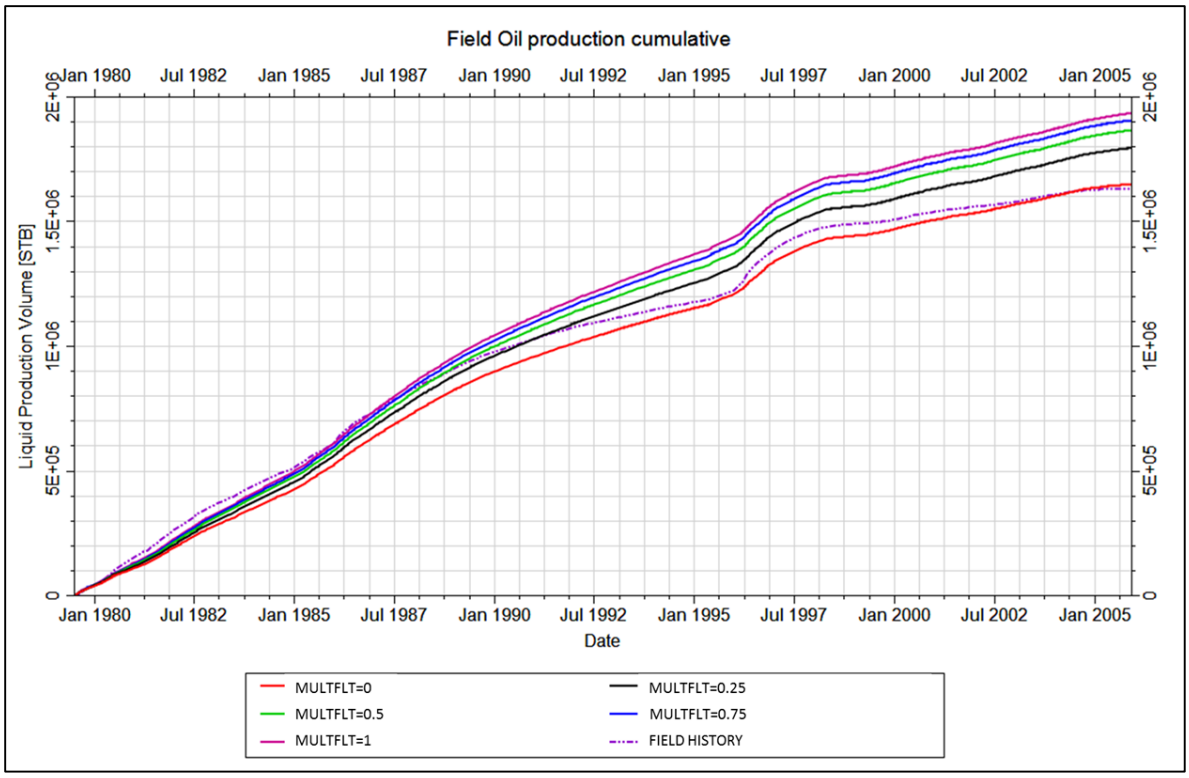

Figure 4-26: Fault multiplier influences the oil production. A multiplier close to 1 means leaky faults and yields higher oil production.

Streamline Analysis

We undertook streamline simulation (Muskat and Wyckoff 1934; Batycky et al. 1997; King and Datta-Gupta, 1998) to visulaize flow paths in the history matched model. A streamline is defined as flow path or flow direction. It is a vector that varies from point-to-point with velocity along the flow path. The matched model streamlines show flow patterns perturbed by permeability barriers. Streamlines do not cross permeability barriers, which shows, as designed, the reservoir does not communicate across the permeability barriers (Figure 4-27).

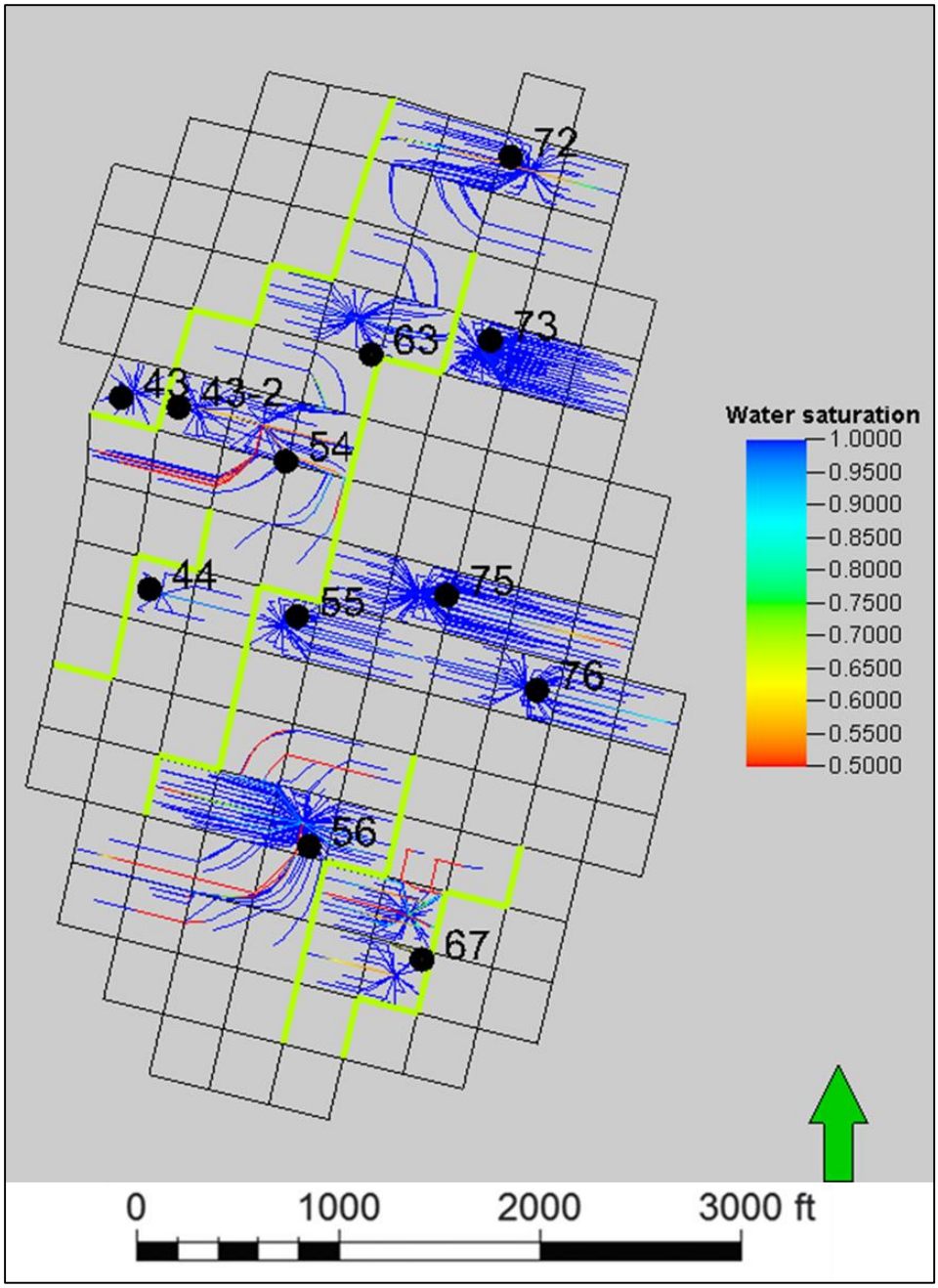

Figure 4-27: Streamline analysis on 03-28-2004 for water saturation around producing wells. The streamline simulator assigns the streamlines to the center of the grids where wells are located. The model is producing mainly water. Well 56-TPX-10 is the most oil prolific well in this field. Note how streamlines change around permeability barriers.

CO_2-EOR

At this point, the input static model has been tuned to match the production history of the field and it is now possible to model CO_2-EOR. The 8-component EOS developed earlier in this chapter is used in a compositional simulator (Eclipse 300) to model CO_2-EOR in the Tensleep reservoir at Teapot Dome, Wyoming. Two models are designed for CO_2-EOR using three horizontal wells within the B1 sandstone (Figure 4-28). In model 1 (denoted as m1), the injectors are parallel to the dominant fracture set (N76°W); and in model 2 (m2), injectors are perpendicular to the dominant fracture set (N14°E). Alternatively, this puts the m1 and m2 laterals perpendicular and parallel, respectively to the flow barriers.

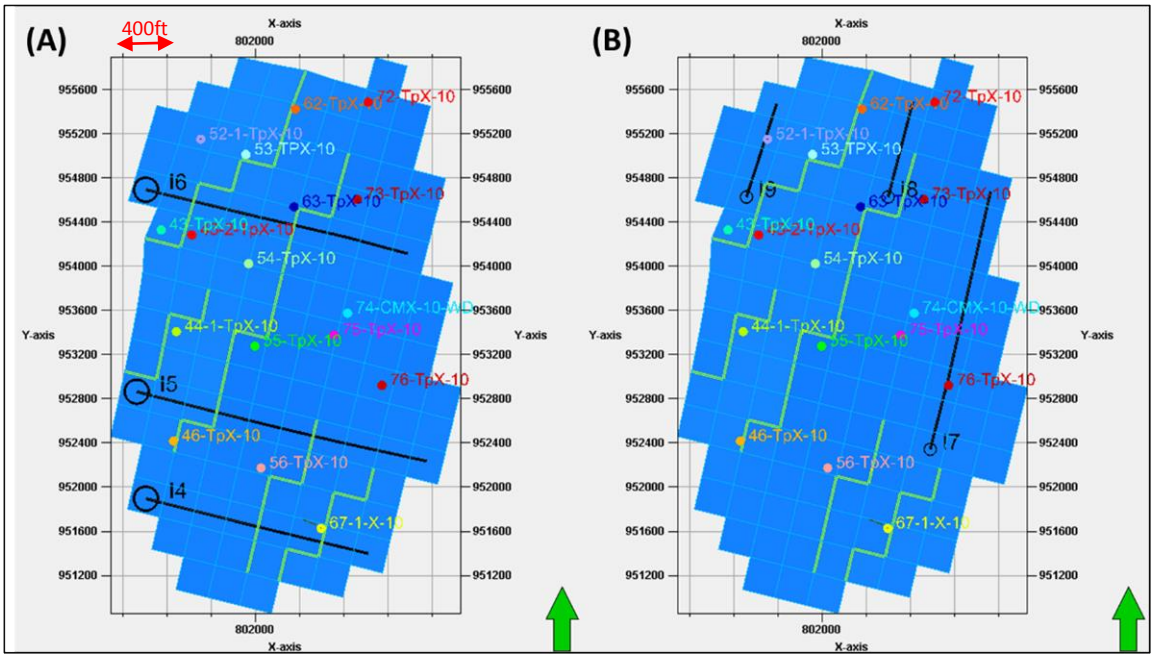

Figure 4-28: A) Model 1 has injectors (I4, I5, and I6) parallel to the main fracture set (N76°W). B) In model 2, Injectors (I7, I8, and I9) are perpendicular to the dominant fracture set. Each grid block is 300ft by 300ft.

Model 1 and 2 have wells which inject 1000 MSCF/day (333.33 Mscf/day per injector) from the end of the production history data (December 01, 2005) to January 01, 2009, a 26 month injection period. This injection rate is proposed by Chiaramonte (2009). The injectors bottom hole pressure

constraint is 3300 psi, equivalent to the threshold pressure for seal integrity of S_1 fault (Chiaramonte, 2009). The bottom hole pressure (BHP) for all the producers is set to 500 psi (Chiaramonte, 2009).

The two models produce significantly different results under CO_2 injection. In m2 breakthrough occurs earlier than m1 since injection is directly into the dominant fracture set along the *j* direction (Figure 4-29). However, the dominant fracture set accelerates CO_2 breakthrough in both models. Models 1 and 2 are compared to a case where no CO_2 is injected. Continued production in models 1 and 2 with EOR is 640 MSTB and 580 MSTB more, respectively, than the case with no CO_2 injection (Figure 4-30).

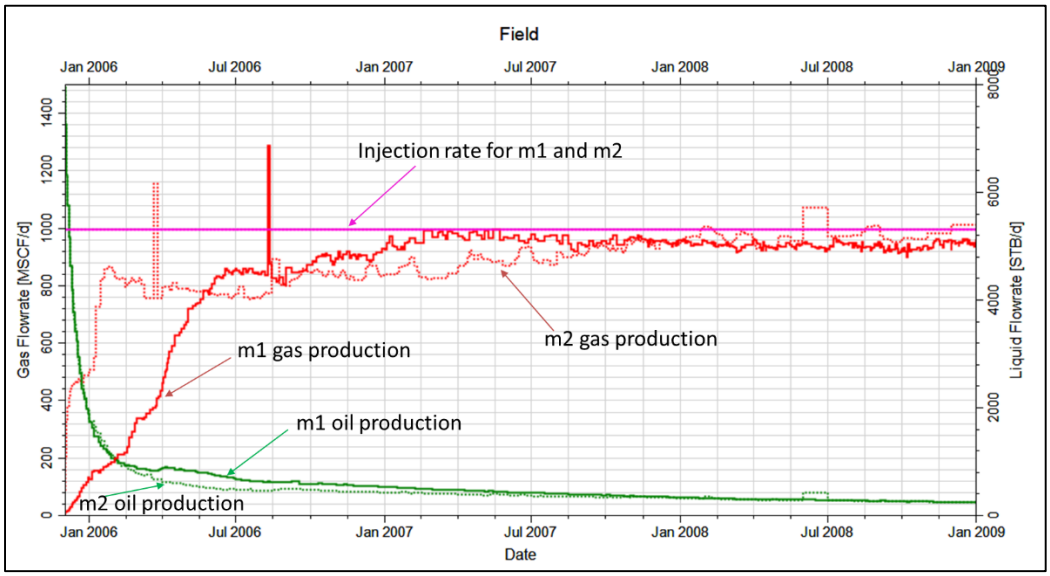

Figure 4-29: A high mole fraction of CO_2 is observed at the producers beginning almost immediately after injection in model 2. Model 1 has a higher oil production and lower gas production rates during the injection at 1000Mscf/day. Both models suffer from early breakthrough because of the fractures which act as easy flow conduits for CO_2 to reach the producers while bypassing the matrix blocks.

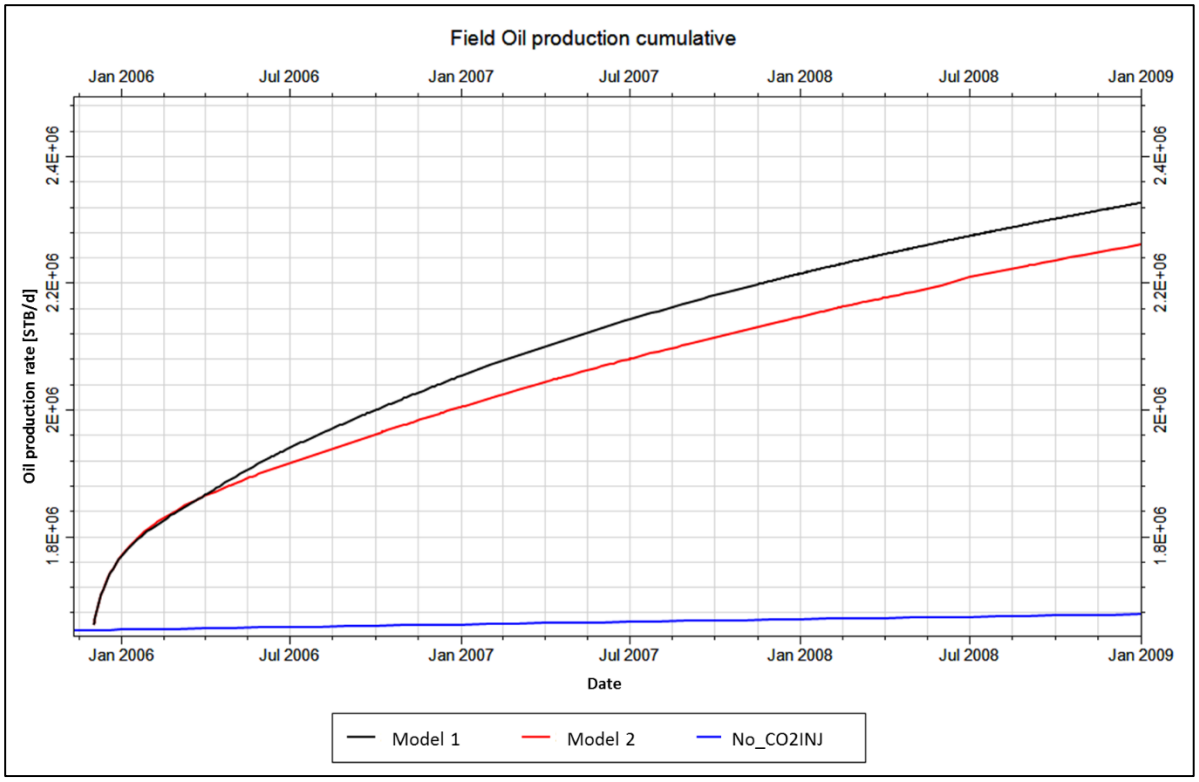

Figure 4-30: The oil production for Models 1 and 2 are compared to an oil production case with no CO_2 injection. The recovery improvement of 640MSTB (black curve) is achieved in Model1 compared to no CO_2 injection case (Blue curve).

We showed earlier in this chapter that an increase in the fault transmissibility multiplier increases the cumulative oil production by nearly 300 MSTB. Results reveal that completely leaky faults yield more oil production (Figure 4-26). Thus, we launched a sensitivity analysis on the fault transmissibility multiplier (MULTFLT) for the CO_2-EOR models. We consider two cases: all permeability barriers are completely sealing (MULTFLT=0), and all permeability barriers are completely leaky (MULTFLT=1). Results show that recovered oil varies up to 150MSTB depends on MULTFLT values. The higher the MULTFLT, the higher the recovered oil (Figure 4-31).

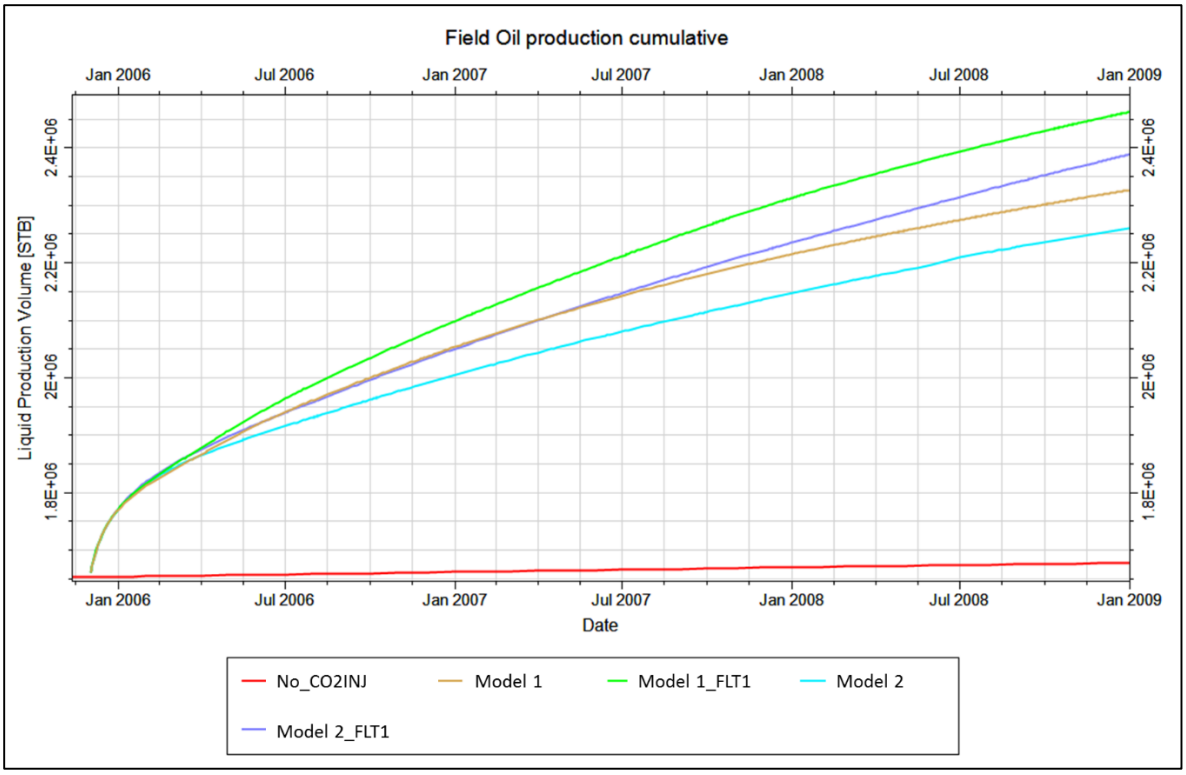

Figure 4-31: Increasing fault multiplier results in higher oil production for both CO_2-EOR models.

Conclusions

- Although history matching is a non-unique process, the results of this study reveals the significant influence of fracture aperture, fault transmissibility multiplier, and vertical permeability on model oil production. Results showed that higher fracture apertures significantly improve model oil production. Aperture distribution in the history matched model is close to the aperture distribution from Core A retrieved from Well 48-X-28, so that model results are consistent with field observed aperture values.
- Fault multipliers are also important factors in oil production modeling that can lead to variation in cumulative oil production from the Tensleep reservoir at Teapot Dome by up to 300 MSTB. We showed that vertical permeability is an uncertain parameter which affects water-conning in the reservoir. An initial aperture multiplier of 5, equivalent to 125

for k_x , k_y and k_z caused a strong water coning. We showed that a permeability multiplier of 62.5 for k_z is necessary to obtain a history match.

- Streamline simulation shows that the dominant (N76°W) fracture set has significant influence on flow orientation. Two other low intensity sets do not significantly control flow directions except for the highest producers when they allow the well to access larger reservoir volume.
- CO_2 tends to emerge in the producers with the start of injection for both models: at a higher rate in model 2 where the injectors are perpendicular to the dominant fracture set (N76°W) and at a lower rate in model 1 where the injectors are oriented parallel to the dominant fracture set.
- Horizontal wells parallel to the main anisotropy axis resulted in a higher sweep efficiency in model 1 compared to model 2.
- A threshold pressure of 3300psi for reservoir sealing was assumed based on work of Chiaramonte, however, at an injection rate of 1000 MSCF/day, this pressure was never reached in either model. Thus, the sealing properties of the S_1 fault and other permeability barriers is not compromised during CO_2-EOR.

Recommendations

1- Both draw-down and build-up well tests are needed to improve fracture permeability estimates.

2- Perforated intervals are crucial for accurate fluid flow modeling and representation of water-conning effects. The new field owner (Standard Oil Resources Corporation) might provide key perforation location data.

3- The EOS could be improved if more lab data were available. Differential liberation tests, separator tests and constant composition expansion are necessary to provide a more accurate EOS.

4- Local grid refinements around the injectors and producers can improve our understanding of flow patterns and sweep efficiency around wells.

5- Stochastic modeling matrix porosity and permeability could be investigated as a possible mean to improve the accuracy of the results. The challenge faced in this effect would be the requirements for increased processing times and more rigorous convergence problems.

6- The relative permeabilities of fractures are important parameters that are assumed to vary linearly with phase saturation. Future study of relative fracture permeabilities are needed.

7- The ultimate recovery in CO_2-EOR can be optimized by using well controlling strategies such as pressure rise control or gas saturation decrease. A gas saturation decrease shows that CO_2 is less moving as a free gas phase and is mixed with the oil in a miscible process.

8- Smaller grid dimensions on the order of 10ft by 10ft should be tested. Such tests will likely require access to proper computing resources.

9- The 8 component EOS in this study can be reduced to 4 component EOS by lumping heavy components. It will greatly improve simulation speed.

Acknowledgement

We would like to thank Rocky Mountain Oil Testing Center, which provided us with 3D seismic and log data for Teapot Dome. The use of Eclipse and Petrel from Schlumberger, and CMG from Computer Modelling Group is greatly appreciated; these software resources made the analysis presented in this paper possible. We also thank Vicki Stamp for providing us with PVT report of oil samples. Production data were sorted and formatted for Petrel by Valerie Smith from Schlumberger.

Nomenclature

δ_{ij} The Kronecker delta function.

$\propto$ Equation of state temperature dependence function.

λ Dimensionless material-dependent constant.

ω Acentric factor.

v Molar volume, [L^3Mole^{-1}], m^3/mole.

A_k k^{th} Fracture area, [L^2], ft^2.

a, b Peng-Robinson equation of state parameters.

F_{ij} The fracture tensor, [L^2], mD.

F_T The trace of the fracture tensor matrix, [L^2], mD.

k_{ij} The permeability tensor, [L^2], mD.

$n_{j,}n_i$ The components of fracture unit normal vector.

n_{ik} , n_{jk} The components of the unit normal vector on k^{th} fracture.

m Intermediate function in equation of state.

P Pressure, [$ML^{-1}T^{-2}$], Pa.

R Gas constant=8.314472, [$ML^2T^{-2}\,\theta^{-1}\,Mole^{-1}$], Pa-m³/ (Kelvin-mole).

T Temperature, [θ], $°K$.

Subscripts

i, j, k Arbitrary orthogonal coordinate system components.

c Critical.

r Reduced property.

REFERENCES

Araktingi, Udo Gaetan, FM Orr Jr. 1993. Viscous fingering in heterogeneous porous media. SPE Advanced Technology Series **1** (01): 71-80.

Barenblatt, GI, Iu P Zheltov, IN Kochina. 1960. Basic concepts in the theory of seepage of homogeneous liquids in fissured rocks [strata]. Journal of applied mathematics and mechanics **24** (5): 1286-1303.

Batycky, RP, Martin J Blunt, Marco R Thiele. 1997. A 3D field-scale streamline-based reservoir simulator. SPE Reservoir Engineering **12** (04): 246-254.

Caine, J. S., J. P. Evans, and C. B. Forster. 1996. Fault zone architecture and permeability structure. Geology **24**:1025–1028

Chiaramonte, Laura. 2009. Geomechanical Characterization and Reservoir Simulation of a Carbon Dioxide Sequestration Project in a Mature Oil Field, Teapot Dome, WY, ProQuest (Reprint).

Chung, Frank TH, Ray A Jones, Hai T Nguyen. 1988. Measurements and correlations of the physical properties of CO_2-heavy crude oil mixtures. SPE reservoir engineering **3** (03): 822-828.

Cooper, Scott Patrick. 2000. Deformation within a basement-cored anticline: Teapot Dome, Wyoming, Citeseer.

Dershowitz, Bill, Paul LaPointe, Thorsten Eiben et al. 2000. Integration of Discrete Feature Network Methods With Conventional Simulator Approaches. SPE Reservoir Evaluation & Engineering **3** (02): 165-170.

Friedmann, S Julio, Vicki W Stamp. 2006. Teapot Dome: Characterization of a CO_2-enhanced oil recovery and storage site in Eastern Wyoming. Environmental Geosciences **13** (3): 181-199.

Gaviria Garcia, Ricardo. 2006. Reservoir simulation of CO_2 sequestration and enhanced oil recovery in Tensleep Formation, Teapot Dome field, Texas A&M University.

Gong, Bin, Mohammad Karimi-Fard, Louis J Durlofsky. 2008. Upscaling discrete fracture characterizations to dual-porosity, dual-permeability models for efficient simulation of flow with strong gravitational effects. SPE Journal **13** (01): 58-67.

Green, Thom H., and C. W. Ziemer. 1953. Northwest Lake Creek Area, Hot Springs County, Wyoming. Tulsa Geological Society Digest **21**: 114-115.

Gupta, A, G Penuela, R Avila. 2001. An integrated approach to the determination of permeability tensors for naturally fractured reservoirs. Journal of Canadian Petroleum Technology **40** (12).

Hycal Energy Research Laboratories Ltd., 2004, DOE-RMOTC, Teapot Dome Miscibility study, final report, December 13, 2004, 29 p.

Jarrell, Perry M. 2002. Practical aspects of CO_2 flooding, Richardson, Tex.: Henry L. Doherty Memorial Fund of AIME, Society of Petroleum Engineers (Reprint).

Karimi-Fard, M, LJ Durlofsky, K Aziz. 2004. An Efficient Discrete-Fracture Model Applicable for General-Purpose Reservoir Simulators. SPE Journal **9** (02): 227-236.

Karimi-Fard, Mohammad, Abbas Firoozabadi. 2003. Numerical simulation of water injection in fractured media using the discrete-fracture model and the Galerkin method. SPE Reservoir Evaluation & Engineering **6** (02): 117-126.

Karimi-Fard, M, B Gong, LJ Durlofsky. 2006. Generation of coarse-scale continuum flow models from detailed fracture characterizations. Water resources research **42** (10).

Kavousi Ghahfarokhi, Payam.2016. The Structured Gridding Implications for Upscaling Model Discrete Fracture Networks (DFN) Using Oda's Method. Society of Petroleum Engineers Journal: Submitted

Kavousi Ghahfarokhi, Payam, Thomas H Wilson. 2015. Fracture intensity attribute for the Tensleep reservoir at Teapot Dome, Wyoming, USA. Interpretation **3** (3): SZ41-SZ48.

Kazemi, H, LS Merrill Jr, KL Porterfield et al. 1976. Numerical simulation of water-oil flow in naturally fractured reservoirs. Society of Petroleum Engineers Journal **16** (06): 317-326.

Khorsandi, Saeid, Kaveh Ahmadi, Russell T Johns. 2014. Analytical solutions for gas displacements with bifurcating phase behavior. SPE Journal **19** (05): 943-955.

King, Michael J, Akhil Datta-Gupta. 1998. Streamline simulation: A current perspective. In Situ **22** (1): 91-140.

Li, Junchao, Zhengdong Lei, Guan Qin et al. 2015. Effective Local-Global Upscaling of Fractured Reservoirs under Discrete Fractured Discretization. Energies **8** (9): 10178-10197.

Li, Liwei, Saeid Khorsandi, Russell T Johns et al. 2015. CO_2 enhanced oil recovery and storage using a gravity-enhanced process. International Journal of Greenhouse Gas Control **42**: 502-515.

Lorenz, J. C., and S. P. Cooper, 2004, Analysis of fracture characteristics and distribution of 48-X-28 well. Rocky Mountain Oilfield Testing Center Report, 31 p.

Lorenz, J. C., and S. P. Cooper. 2013. Natural fractures in folded sandstones of the Tensleep Formation, Wyoming.in C. Knight, and J. Cuzella, eds., Application of structural methods to Rocky Mountain hydrocarbon exploration and development. AAPG, Studies in Geology **65**: 175–213.

Muskat, M, RDt Wyckoff. 1934. A theoretical analysis of water-flooding networks. Transactions of the AIME **107** (01): 62-76.

Oda, Mc. 1985. Permeability tensor for discontinuous rock masses. Geotechnique **35** (4): 483-495.

Peng, Ding-Yu, Donald B Robinson. 1976. A new two-constant equation of state. Industrial & Engineering Chemistry Fundamentals **15** (1): 59-64.

Penuela, G, F Civan, RG Hughes et al. 2004.Time-dependent shape factors for interporosity flow in naturally fractured gas-condensate reservoirs. Society of Petroleum Engineers.

Romm, Evgeniĭ Solomonovich, William R Blake. 1972. Fluid flow in fractured rocks, Phillips Petroleum Company (Reprint).
Sarma, Pallav. 2003. New transfer functions for simulation of naturally fractured reservoirs with dual porosity models, Stanford University.
Texas, A. and Ferguson, D. 2002. Investigation of Efficiency Improvements during CO_2 Injection in Hydraulically and Naturally Fractured Reservoirs. Semi-Annual Technical Progress Report. DOE Contract No.: DE-FC26-01BC15361: 88 p
Thomas, L Kent, Thomas N Dixon, Ray G Pierson. 1983. Fractured reservoir simulation. Society of Petroleum Engineers Journal 23 (01): 42-54.
van Golf-Racht, Theodor D. 1982. Fundamentals of fractured reservoir engineering, Elsevier (Reprint).
Warren, JE, P Jj Root. 1963. The behavior of naturally fractured reservoirs. Society of Petroleum Engineers Journal **3** (03): 245-255.
Wilson, Thomas H, Valerie Smith, Alan Brown. 2015. Developing a model discrete fracture network, drilling, and enhanced oil recovery strategy in an unconventional naturally fractured reservoir using integrated field, image log, and three-dimensional seismic data. AAPG Bulletin **99** (4): 735-762.

Chapter 5: Conclusions

In Chapter 2, we used 3D poststack seismic data along with wireline image log to generate a fracture intensity attribute for the Tensleep reservoir at Teapot Dome. We showed that the most negative curvature attribute can be combined with the similarity attribute to generate an edge-enhanced volume for discontinuity extraction using an edge-illumination process. Extracted discontinuities are interpreted to result from local velocity sag produced across more intensely fractured zones or flexures. Discontinuities extracted from the seismic data are dominated by a northwest trend similar to the trend of the dominant northwest hinge-oblique fracture set identified in several wireline image logs available from the field. The modeled discontinuities are nearly parallel to S_{Hmax} and are likely to remain open during CO_2-EOR operations. The comparison of modeled intensity and cumulative production data indicates that better producing wells are located along these northwest-trending discontinuities.

In Chapter 3, We conducted a detailed study of Oda's method for discrete fracture network upscaling. In this process, the porosity and permeability of individual fractures within individual grid cells are averaged in the case of ϕ and transformed into a grid cell tensor in case of permeability. We showed that grid block orientation relative to the DFN influences the Oda upscaled permeability tensors and hence the fluid simulation results. When grid walls are oriented parallel and perpendicular to the dominant fracture set, the geometric mean of the Oda permeability tensor components (K_G) drops to a minimum as does the simulated cumulative production. Any grid rotation angle which brings the dominant fractures to a 45° angle diagonally through the grid block local principal directions (i and j) maximizes K_G and thesimulated cumulative production. The eigenvector analysis and streamline simulations reveal multiple flow directions through a DFN dominated by a single set. For 3 fracture sets identical to those found in the Tensleep reservoir

at Teapot Dome, the off-diagonal permeability components fall to zero when the grid is oriented at N72°W. Thus, we oriented the grid at N72°W to improve calculation speed during the flow simulation. This orientation is roughly parallel to the dominant fracture set N76°W.

The CO_2-EOR analysis of the resulting reservoir model improved our understanding of fluid flow in this fractured reservoirs. Although history matching is a non-unique process, the results of this study reveals the significant influence of fracture aperture, fault transmissibility multiplier, and vertical permeability on model oil production. Results showed that higher fracture apertures significantly improve model oil production. Aperture distribution in the history matched model is close to the aperture distribution from Core A retrieved from Well 48-X-28, so that model results are consistent with field observed aperture values.

Fault multipliers are also important factors in oil production modeling that can lead to variation in cumulative oil production from the Tensleep reservoir at Teapot Dome by up to 300 MSTB. We showed that vertical permeability is an uncertain parameter which affects water-conning in the reservoir. An initial aperture multiplier of 5, equivalent to multiplier of 125 for k_x , k_y and k_z led to a strong water coning. We showed that a permeability multiplier of 62.5 for k_z is necessary to obtain a history match.

Streamline simulation shows that the dominant (N76°W) fracture set has significant influence on flow orientation. Two other low intensity sets do not significantly control flow directions except for the highest producers for which they allow the well to access larger reservoir volume.

CO_2 tends to emerge in the producers with the start of injection for both models: at a higher rate in model 2 where the injectors are perpendicular to the dominant fracture set (N76°W) and at a lower rate in model 1 where the injectors are oriented parallel to the dominant fracture set.

Horizontal wells parallel to the dominant fracture set (main anisotropy axis) resulted in a higher sweep efficiency in model 1 compared to model 2.

A threshold pressure of 3300psi for reservoir sealing was assumed based on work of Chiaramonte, however, at an injection rate of 1000 MSCF/day, this pressure was never reached in either model. Thus, the sealing properties of the S_1 fault and other permeability barriers is not compromised during CO_2-EOR.